# A novel Monte-Carlo based method of calculating mean transit time through voxelized biological organs

by

Md Istiak Ahmad

B.S., Bangladesh University of Engineering and Technology, Bangladesh, 2022

---

A Thesis

submitted in partial fulfillment of the
requirements for the degree

MASTER OF SCIENCE

Alan Levin Department of Mechanical and Nuclear Engineering
Carl R. Ice College of Engineering

KANSAS STATE UNIVERSITY
Manhattan, Kansas

2025

| Approved by: | Approved by: |
| --- | --- |
| Co-Major Professor | Co-Major Professor |
| Amir A. Bahadori | Steven J. Eckels |

# Copyright

# Abstract

Capillary transit time, defined as the time required for blood to traverse the microvascular network, is a cornerstone parameter in the study of hemodynamics. The study of capillary transit time, the foundation of which was laid by August Krogh in his seminal 1919 work, has come a long way since its advent. At present, capillary transit time analysis is being used to assess microvascular function and tissue oxygenation in conditions like stroke, tumors, and neurodegenerative diseases, guiding treatment strategies in radiotherapy and thrombolysis. It also helps optimize drug delivery by revealing how blood flow heterogeneity affects therapeutic agent distribution and retention in target tissues. With the advancement of blood flow simulation using computational human phantoms (CHP), a potential novel use of capillary transit time analysis in the field of internal and external dosimetry has arisen, where it may be used to predict the distribution of dose imparted by the radiophermaceuticals and the distribution of irradiated white blood cells in tumors. Various experimental and mathematical methods have been developed over the years to measure and predict capillary transit time. However, these models lack applicability in particle tracing applications. On the other hand, existing Monte-Carlo particle tracing codes lack the functionality of tracing particles inside vasculatures. Hence, the aim of the present work is to develop a path tracing algorithm that follows blood flow in the vasculature, including the capillary bed, using the principles of Monte-Carlo simulation and existing blood flow framework found in contemporary literature (The VoM-PhyS framework) to facilitate the calculation of mean transit time.

One of the main challenges in developing a path tracing framework is finding a suitable probability distribution of possible next steps, based on which each step of the random walk of the particles is chosen. In the present study, this probability distribution is derived based on the outgoing flow rate at a particular node. Flow rate is calculated from governing

equations, including Hagen-Poiseuille and Darcy's equation of porous media, depending on particle location in the network. Using this probability distribution, random particle tracks are generated for increasing particle numbers and the associated elapsed-times are calculated. Variability of the elapsed time resulting from variation in the particle's velocity considering its position with respect to the centerline of arterial and venous vessels is accommodated in this framework, as well. In the VoM-PhyS model, blood takes an instantaneous jump from the terminal of the segmentable vessels to a nearby tissue voxel within a specified sphere of influence. A method of estimating the time elapsed in this jump was also developed and implemented. The transit time distributions and the mean transit times were derived from these data. It was found that the distribution of mean transit time follows a gamma-variate distribution, which flattens with increasing sphere of influence, i.e., the variation in times increases. It was also found that the peak of the distributions shifts to increasing time values and the mean transit time increases with increasing sphere of influence. Finally, results of various statistical tests are presented to verify the statistical significance of the data generated using the proposed framework.

# Table of Contents

# List of Figures

# List of Tables

# Nomenclature

| | |
|---|---|
| $\alpha$ | Perfusion proportionality factor ($\mathrm{m\,s\,kg^{-1}}$) |
| $\Delta P$ | Pressure drop in the vessel segment (Pa) |
| $\Delta P_{entry}$ | Transmural pressure at vessel entrance (Pa) |
| $\Delta P_{exit}$ | Transmural pressure at vessel exit (Pa) |
| $\Delta s$ | Distance between the centers of voxels (m) |
| $\Delta V$ | Volume of a voxel ($\mathrm{m^3}$) |
| $\delta$ | Offset from vessel wall (m) |
| $\dot{q}_{ji}$ | Flow rate from node $j$ to node $i$ ($\mathrm{m^3\,s^{-1}}$) |
| $\epsilon$ | Sphere of influence radius (m) |
| $\gamma_\beta$ | Pressure drop parameter |
| $\kappa$ | Hematocrit and tissue density constant |
| $\mathcal{P}_k$ | Probability of selecting node $k$ |
| $\mathcal{Q}$ | Blood flow in Klitzman's model ($\mu\mathrm{m^3\,s^{-1}}$) |
| $\mathcal{R}$ | Geometric resistance of blood vessel in Klitzman's model ($\mu\mathrm{m^{-3}}$) |
| $\mathcal{V}$ | RBC velocity ($\mu\mathrm{m\,s^{-1}}$) |
| $\mu$ | Viscosity of blood (s) |
| $\mu'_{ij}$ | Non-dimensional viscosity |

| | |
|---|---|
| $\mu_{en}$ | Energy-absorption coefficient |
| $\Omega$ | Specified region in the simulation domain |
| $\psi$ | Angular flux ($\mathrm{cm}^{-1}\,\mathrm{sr}^{-1}$) |
| $\rho$ | Mass density ($\mathrm{kg\,m}^{-3}$) |
| $\tilde{A}(r_s)$ | Time-integrated activity (Bq-h) |
| $\xi$ | Uniform random number between 0 and 1 |
| $A$ | Cross-sectional area of the voxel perpendicular to the direction of flow ($\mathrm{m}^2$) |
| $C_a(t)$ | Arterial input function |
| $C_t(t)$ | Tissue concentration-time curve |
| $c_{out}(t)$ | Tracer concentration at the outlet |
| $CBF$ | Cerebral blood flow |
| $CBV$ | Cerebral blood volume |
| $D(r_T)$ | Absorbed dose to a target region $r_T$ (Gy) |
| $d_k(x,t)$ | Dose rate at position $x$ and time $t$ (Gy/h) |
| $E$ | Energy (J) |
| $E_{dep,j}$ | Energy deposited during the $j$th history in a cell (J) |
| $F$ | Blood flow rate ($\mathrm{m}^3\,\mathrm{s}^{-1}$) |
| $F_{rbc}$ | RBC flux ($\mathrm{s}^{-1}$) |
| $G(y)$ | Amount of blood flow in the terminal vessel ($\mathrm{m}^3\,\mathrm{s}^{-1}$) |

| | |
|---|---|
| $G^{\epsilon}(x)$ | Flow rate from the terminal to a voxel at a distance $x$ within its sphere of influence radius $\epsilon$ ($\mathrm{m}^3\,\mathrm{s}^{-1}$) |
| $G_a$ | Arterial source term ($\mathrm{m}^3\,\mathrm{s}^{-1}$) |
| $G_v$ | Venous sink term ($\mathrm{m}^3\,\mathrm{s}^{-1}$) |
| $H$ | Hematocrit (%) |
| $h$ | Capillary sheet thickness (m) |
| $h(t)$ | Distribution of transit times |
| $K$ | Permeability of porous medium ($\mathrm{m}^2$) |
| $K_a$ | Permeability of arterial compartment ($\mathrm{m}^2$) |
| $K_v$ | Permeability of venous compartment ($\mathrm{m}^2$) |
| $L$ | Vessel length (m) |
| $L_{ji}$ | Length of the vessel with end-nodes $j$ and $i$ (m) |
| $MCV$ | Mean corpuscular volume ($\mu\mathrm{m}^3$) |
| $MTT$ | Mean transit time (s) |
| $P(v_1)$ | Probability of entering the network through vessel $v_1$ |
| $P(v_{i+1}\|v_i)$ | Probability of moving to vessel $v_{i+1}$ given the current vessel $v_i$ |
| $p_k$ | Pressure at node $k$ in a vessel |
| $P_{j,a}$ | Pressure in the arterial compartment of voxel $j$ (Pa) |
| $P_{j,v}$ | Pressure in the venous compartment of voxel $j$ (Pa) |
| $R$ | Vessel radius (m) |

| | |
|---|---|
| $r$ | Position of a particle with respect to the vessel centerline (m) |
| $R(t)$ | Fraction of total tracer remaining in tissue |
| $R_{ji}$ | Radius of the vessel with end-nodes $j$ and $i$ (m) |
| $S(r_T \leftarrow r_s)$ | Mean absorbed dose to the target region per nuclide decay in the source region (Gy) |
| $S(t)$ | Signal intensity |
| $s_{ij}$ | Slenderness ratio |
| $t_c$ | Characteristic transit time in Goirand's model (s) |
| $t_{kj}$ | Time to travel from voxel $j$ to voxel $k$ (s) |
| $TE$ | Echo time (s) |
| $u$ | Velocity, mass flux ($\mathrm{m\,s^{-1}}$) |
| $V$ | Volume ($\mathrm{m^3}$) |
| $w_j$ | statistical weight |
| $x_{ij}$ | Pressure drop fraction |
| $<t^2>$ | Second moment of $h(t)$ |
| $<t_{MR}>$ | First moment of the MR signal |
| $<t>$ | First moment of $h(t)$ |

# Acknowledgments

I express my sincerest gratitude towards my advisors, Dr. Steven Eckels and Dr. Amir Bahadori. They not only guided my research, but also mentored my intellectual growth, sharpened my problem-solving skills, and provided constant support during failures. I am immensely indebted to them for the knowledge, skills, and perspective I have gained, both as a scholar and as an individual.

My sanity will become questionable if I don't mention one person particularly. Dr. Rohan P. Amare. This person single-handedly supported my works, as a mentor, a helping hand, a coder, a debugger, a mental support, and a brotherly figure. He spent innumerable hours with me, solving problems in my codes, answering my silly questions, and teaching me how to navigate through the graduate life. I shall be lifelong indebted to him.

I'd like to thank my roommate and friend Muhaiminul Islam for helping me prepare high quality figures for the thesis. I'd also like to thank my friend Jahid Chowdhury for his help in debugging and parallelizing my code.

Finally, I want to express my utmost gratitude to my dearest friend Yasir Nazir Parrey, without whom I'd become homeless for the last few months of my stay in Manhattan. Yasir hosted me at his apartment, cooked for me, pushed me to work hard, and gave me company even if he had his own preoccupation, like a true friend in need. I consider myself blessed to have him as a friend.

# Dedication

I dedicate my thesis to all of humanity, with the humble hope that someday this little effort may contribute, even in a small scale, to the betterment of human lives.

# Chapter 1

# Introduction

Blood is the most vital liquid, found in vertebrates and some invertebrates, facilitating the transport of nutrients, gases, and waste. Blood is categorized as a specialized connective tissue consisting of cellular components, i.e., red blood cells, white blood cells, and platelets, suspended in a liquid extracellular matrix named plasma[1;2]. In humans and other vertebrates, the system that sustains the blood flow is known as the cardiovascular system. This system is responsible for not only transporting nutrients, gases, and waste, but also for regulating body temperature, balancing pH, and homeostasis. The cardiovascular system consists of the heart, arteries, capillaries, and veins. The heart serves as the pumping machine for blood, and the arteries, capillaries, and veins serve as conduits[2].

The study of blood flow, known as hemodynamics, is of vital importance to medical professionals, researchers, and engineers. It underpins our understanding of cardiovascular physiology, the diagnosis and treatment of circulatory disorders, and the development of advanced medical devices. The dynamics of blood flow is quantitatively governed by the heart's pumping action, vascular resistance, blood viscosity, vessel elasticity, and many more parameters[3–5]. From a radiobiological perspective, the study of blood flow is crucial because of its impact on tissue oxygenation, which eventually influences the effectiveness of radiation treatment[6]. Radiation dose calculation, delivery, and treatment planning is highly reliant on the knowledge of blood flow. Hypoxic regions caused by insufficient blood perfusion exhibit

reduced sensitivity to radiation, which requires higher doses to achieve therapeutic effects[7]. This, in turn, might increase the risk of collateral damage to healthy tissues. Understanding blood flow dynamics helps model the oxygen distribution and its resulting radiobiological response, enabling the development of advanced treatment protocols like dose painting, where higher doses are targeted to hypoxic areas.

Particle tracing is a well-known computational technique used to simulate the trajectories of individual particles as they move through a medium. This technique is usually underpinned by some law of physics, e.g., pressure field, electromagnetic interaction, or Newton's laws. The Monte-Carlo method is a very famous particle tracing technique. The Monte-Carlo methods are a class of stochastic techniques that use random sampling to model and simulate complex systems and processes[8]. They account for various probabilistic behaviors, such as diffusion, collision, transition of states, fluctuations due to perturbations, etc. In the context of blood particle tracing, these methods can simulate the movement of blood cells or drug particles within the cardiovascular system, considering factors like fluid dynamics[9], interactions with vessel walls, and concentration gradient. By incorporating Monte-Carlo techniques, uncertainties and variability in particle behavior, such as the distribution of white blood cells or the transport of nanoparticles for drug delivery, can be modeled with high fidelity.

Capillary transit time (CTT), defined as the time required for blood to traverse the microvascular network, serves as a fundamental hemodynamic parameter that critically influences oxygen delivery and metabolic exchange in tissues. Since its foundation laid by the pioneering work of August Krogh[10] in 1919, CTT analysis has evolved into an indispensable tool for understanding blood flow in microvasculature as well as studying diseases like stroke and cancer. The average time that it takes for the blood particles to travel through a specific vascular region is known as the mean transit time (MTT)[11;12]. MTT is dependent on blood volume, flow rate, heart rate, perfusion, etc[13]. The knowledge of MTT can play a very important role in internal and external radiotherapy. In internal radiotherapy (e.g., radiopharmaceutical therapy), MTT is crucial for predicting the distribution and retention of radioactive agents within target tissues. Prolonged MTT in tumors may enhance radiation

dose deposition due to extended radiopharmaceutical retention, while rapid MTT in healthy tissues reduces off-target exposure[14]. Conversely, in external beam radiotherapy, MTT serves as a surrogate for tissue oxygenation; shorter MTT correlates with better oxygen delivery, thereby increasing radiation efficacy via the oxygen enhancement effect (OER)[15]. MTT is essential for mapping oxygen availability in tissues, as oxygen enhances the efficacy of ionizing radiation through the formation of reactive oxygen species[16]. Computational models incorporating CTT heterogeneity[17] further refine dose planning by identifying hypoxic, radioresistant tumor subregions that may require dose escalation.

The brief introductory remarks stated so far signify the importance of blood flow modeling and particle tracing and how they can be of service in radiation biology and medicine. The prime goal of this work is to find a way of combining these two to create a framework for better calculating the MTT.

## 1.1 Problem Statement and Scope of Research

Figure 1.1 illustrates the objectives of this thesis. The first step is to identify a blood flow framework that closely aligns with the desired goals of the study. The suitable type of simulation domain and control equations to be analyzed are dictated by the framework. Once the domain is set up accordingly, the simulation is run to generate the blood flow quantities, e.g., pressure and flow rate. Finally, for modeling particle transport, an algorithm is needed to utilize the blood flow quantities to generate tracks, and equations to calculate the time elapsed. Standard statistical procedures are to be carried out to calculate the MTT, its associated uncertainties, and the statistical significance of the result. The distinct objectives are described in more detail as follows.

1. **Identifying a suitable blood flow framework**

   A multitude of methods can be found in the literature that have been proposed to simulate the blood flow inside biological domains. Chapter 2 of this thesis sheds light on a select few of them that bear pertinence. For the purpose of the current research,

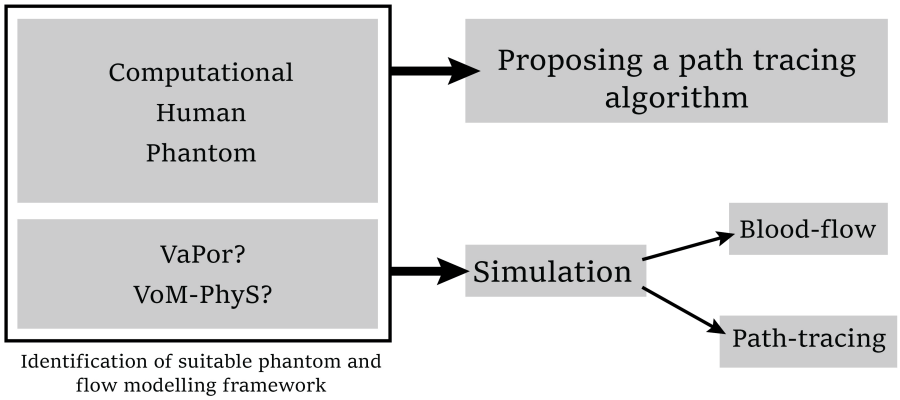


Figure 1.1: Outline of the proposed research activities.

the criteria being sought after are ease of handling, robustness, versatility and personalizeability. These criteria are chosen so that the resulting framework be applicable in the field of radiation therapy. Among the discussed frameworks, the most befitting one according to the stated criteria will be chosen.

2. **Proposing a path tracing algorithm in conjunction with the blood flow framework and its implementation**

   In chapter 3, the equations and methods behind the chosen blood flow framework will be briefly discussed. A path tracing algorithm will be developed using the results of the blood flow framework. The necessary assumptions, rules, equations and rationales will be provided. Chapter 3 will also delineate the necessary steps regarding the preprocessing of the computational domain, preparation of the coding scripts, computational resources, and actions of running the simulation.

3. **Simulating blood flow, tracing paths and justifying the results**

   Chapter 4 of this work will present the results obtained from the simulation of blood flow and path tracing. It will pose the results in the form of various plots and contours,

discuss and interpret various aspects of it. Chapter 4 will also show the results of statistical tests to verify the generated data.

# Chapter 2

# Literature Review

This chapter focuses on the review of existing scientific literature that inspired the current work and shed more light on the aims of this research. The first section expounds on the methods of calculation and the use of Capillary Transit Time (CTT) and Mean Transit Time (MTT) in various sectors of the study of hemodynamics. Succinct descriptions of different approaches of calculating or estimating the MTT, which ranges from experimental to purely mathematical, their advantages, and potential shortcomings in the light of the current state of scientific advancement will also be a goal of this section.

The prime objective of this work is to propose a path tracing framework inspired by Monte-Carlo simulation. Hence, it is imperative to shed light on the Monte-Carlo methods. The section following the review of CTT is going to present a brief introduction to the Monte-Carlo path tracing techniques. This section will provide a brief description of the steps that run inside the black-box of a typical Monte-Carlo software package. It will also provide a brief description of various existing Monte-Carlo software packages and their functionalities.

In modern times, the study of hemodynamics has become highly reliant on computational techniques. New methods of representing the vasculature to .increasingly finer detail are being invented. The methods of simulating blood flow within this vasculature are also becoming increasingly sophisticated, ranging from in-house models to full-fledged commercial software packages. Computational human phantoms are models that represent accurate

anatomical structures of the organs and human body in a computer environment. These are the tools of a dosimetrist to study the effect of radiation on tissues and hemodynamics in a human body. The subsequent two sections are going to present an introductory account of the computational phantoms and a short review of the relevant blood flow simulation models along with their vascular representation techniques in the existing literature. This will lay the foundation to make a judicious choice of a suitable blood flow simulation model for the purpose of this study.

Finally, the main goal of this study, which is to develop a path tracing framework inside the vasculature and calculate the MTT, is revisited and elaborated. Shortcomings of existing models are identified and how the proposed solution addresses those shortcomings is discussed. The challenges of the proposed solution are elucidated to conclude this chapter.

## 2.1 Capillary Transit Time

Capillary transit time (CTT) is a fundamental hemodynamic parameter that quantifies the duration blood spends traversing the microvascular network. This metric is critical for understanding oxygen delivery[18], metabolic exchange[17], and waste clearance[19] in tissues, with profound implications for both physiological function and pathological conditions such as stroke[20], Alzheimer's disease[21], and cancer[22]. In radiation therapy, CTT plays a vital role. It affects the distribution of chemotherapeutics[23] and radiosensitizers in the case of internal radiotherapy, while it regulates the distribution of reactive oxygen species[24] to tumor and healthy tissues which affects radiation induced DNA damage in the case of external radiotherapy. The calculation of CTT involves a complex interconnection between microvascular architecture, hemodynamics, and regulatory mechanisms, which necessitates diverse methodological approaches.

Over the years, researchers have approached the study of CTT from many different angles, ranging from direct experimental measurements to sophisticated mathematical modeling. The current section of literature review will focus on some of the prominent methods used in quantifying CTT.

### 2.1.1 Experimental Approaches

Experimental measurements of CTT are often carried out using the magnetic resonance (MR) techniques with intravascular tracers. These techniques derive blood volume estimates by measuring the area under the dynamic contrast-time curve. Flow, on the other hand, is determined from the curve's first moment, applying the Central Volume Principle. Weiskoff et al.[11] describes the method of measuring tissue blood flow using intravascular tracers in MR imaging. Using the Central Volume Principle (CVP), derived from indicator-dilution theory, they prove that

$$MTT = \frac{V}{F} = \int_0^\infty th(t)\ dt \tag{2.1}$$

where $V$ is the volume of blood in the organ, $F$ is the flow rate, and $h(t)$ is the distribution of times required for the tracer to move through the system, i.e. the transit time. They also critique the method challenging the correct interpretation of MTT under the Central Volume Principle. Weiskoff demonstrated that the first moment of the concentration-time curve obtained from tomographic imaging does not directly equate to MTT, which is given by the ratio of blood volume ($V$) to flow ($F$). Instead, the authors show that the first moment of the MR signal corresponds to a higher-order moment of the underlying transit-time distribution, which necessitates careful modeling or relative comparisons for accurate flow estimation. For an outflow experiment, MTT is calculated as the normalized first moment of the tracer concentration at the exit vein:

$$MTT = \frac{\int_0^\infty tc_{out}(t)dt}{\int_0^\infty c_{out}(t)dt} \tag{2.2}$$

where $c_{out}(t)$ is the tracer concentration at the outlet. However, in MR imaging, the signal reflects the fraction of total tracer remaining in the tissue, $R(t)$, rather than the outflow concentration. The relationship between $R(t)$ and the transit time distribution $h(t)$ is given

by:

$$R(t) = 1 - \int_0^t h(t)dt \tag{2.3}$$

The first moment of the MR signal, $<t_{MR}>$, is related to the second moment of h(t), leading to:

$$<t_{MR}> = \frac{\int_0^\infty tR(t)\ dt}{\int_0^\infty R(t)\ dt} = \frac{< t^2 >}{2 < t >} \tag{2.4}$$

where $<t>$ and $<t^2>$ are the first and second moments of $h(t)$. According to Weiskoff, this discrepancy means that $<t_{MR}>$ systematically underestimates the true MTT unless corrected for vascular topology.

Østergaard[12] uses the CVP in his methodological framework for calculating MTT using Dynamic Susceptibility Contrast MRI (DSC-MRI) which is a bolus-tracking method that quantifies cerebral perfusion. The calculation of MTT is rooted in tracer kinetics and relies on the interplay between Cerebral Blood Flow (CBF), Cerebral Blood Volume (CBV), and the residue function, where the residue function describes the fraction of contrast agent present in the vasculature at any given time after injection. The process involves several theoretical and computational steps, each supported by specific equations. Using the CVP in this context, the definition of MTT becomes $MTT = CBV/CBF$. This equation elegantly links MTT to two fundamental hemodynamic parameters. To derive MTT, Østergaard's work first explains how CBV is obtained by integrating the area under the tissue concentration-time curve $C_t(t)$ during the first pass of the contrast agent. The concentration-time curve is derived from MRI signal changes using the following relationship.

$$C_t(t) = -\frac{k \log\left(\frac{S(t)}{S(t_0)}\right)}{TE} \tag{2.5}$$

where $S(t)$ is the signal intensity at time t, $S(t_0)$ is the baseline signal, $TE$ is the echo time, and $k$ is a proportionality constant. CBV is then given by the ratio of the integrals of the

tissue and arterial concentration-time curves.

$$CBV = -\frac{\int_{-\infty}^{\infty} C_t(t)\, dt}{\int_{-\infty}^{\infty} C_a(t)\, dt} \tag{2.6}$$

Here, $C_a(t)$ represents the Arterial Input Function (AIF), which is measured in a major artery supplying the tissue. In practice, absolute CBV quantification is challenging due to partial volume effects. Partial volume effect underestimates the blood volume because it takes the weighted-average of the MR signal if both tissue and blood vessel are detected in a single voxel. In such cases, relative CBV is often reported by integrating the tissue curve alone.

The extraordinary contribution of Østergaard's work to science is the determination of CBF. It is determined by deconvolving the tissue concentration-time curve with the AIF. This process isolates the residue function $R(t)$, which describes the fraction of tracer remaining in the vasculature at time $t$ after an ideally instantaneous injection. The relationship is expressed by the following convolution integral.

$$C_t(t) = CBF \cdot C_a(t) \circledast R(t) \tag{2.7}$$

Solving this equation for $R(t)$ requires deconvolution, which can be performed using model-independent methods like Singular Value Decomposition (SVD) or Fourier transforms, or model-dependent approaches that assume specific vascular structures. The SVD method is particularly robust, as it minimizes noise-related instabilities and provides the residue function directly. CBF is then derived from the initial height of $R(t)$. Since, the whole tracer volume was retained in blood initially, i.e., $R(0) = 1$, CBF equals the initial height of $R(t)$. Once CBV and CBF are determined, MTT is computed using the central volume principle.

Mouridsen et al.[25] and Larsson et al.[26] improve further on Østergaard's work. The paper by Mouridsen et al. presents a parametric approach for estimating the MTT of blood through the cerebral microvasculature using DSC-MRI. The method is based on tracer kinetic theory,

which is similar to Østergaard's. The authors calculate the corrected tracer concentration using the following equation:

$$\kappa C_t(t) = CBF \cdot C_a(t) \circledast R(t) \tag{2.8}$$

where $\kappa$ is a constant accounting for hematocrit and tissue density. To model the residue function, the authors assume a gamma distribution for capillary transit times, given by:

$$h(t|\alpha, \beta) = -\frac{dR}{dt} = \frac{1}{\beta^{\alpha}\Gamma(\alpha)} t^{\alpha-1} e^{-t/\beta} \tag{2.9}$$

where $h(t)$ is the transit time distribution, and $\alpha$ and $\beta$ are shape and scale parameters, respectively. The MTT is derived as $MTT = \alpha\beta$, and the capillary transit time heterogeneity (CTH) is $CTH = \beta\sqrt{\alpha}$.

Larsson et al. use the same method as Østergaard for calculating the MTT of blood through brain capillaries using dynamic contrast-enhanced T1-weighted MRI (DCE-MRI). The authors model $h(t)$ using the following gamma-variate function instead of a general gamma distribution.

$$h(t) = \left[ \left( \frac{t - t_0}{t_{max} - t_0} \right)^{\alpha} \exp\left( \alpha \left( 1 - \frac{t - t_0}{t_{max} - t_0} \right) \right) \right] \Big/ A \tag{2.10}$$

where $t_0$ is the minimal transit time, $t_{max}$ is the time to peak, $\alpha$ is a shape parameter, and $A$ is a normalization constant. For this gamma model, MTT and CTH (standard deviation of $h(t)$) are calculated as:

$$MTT = \frac{\alpha + 1}{\alpha} t_{max}, \qquad CTH = \frac{\sqrt{\alpha + 1}}{\alpha} t_{max} \tag{2.11}$$

The analysis involves fitting the gamma-variate model to DCE-MRI data.

Sassaroli et al.[14] in their 2015 study investigate the impact of CTT distributions on hemodynamic models used in coherent hemodynamics spectroscopy (CHS). The study extends Fantini's[27] original hemodynamic model, which assumes a single CTT value, by in-

corporating a gamma-distributed (Eq. 2.9) CTT to better reflect physiological variability. The goal is to evaluate how this distribution affects the model's predictions of oxy- and deoxyhemoglobin concentrations, as well as average capillary and venous saturations. The study concludes that the original model suffices for narrow CTT distributions but requires extension for broader ones.

Klitzman and Johnson's[28] 1982 study represents a crucial investigation into the microcirculatory dynamics of skeletal muscle, specifically examining how capillary network geometry influences red blood cell (RBC) distribution and oxygen delivery. In their work, CTT was used as a key measure to assess oxygen delivery efficiency and flow heterogeneity in the hamster cremaster muscle. The measurements taken by their experiment enabled the calculation of several derived parameters, including geometric resistance, $\mathcal{R} = 8L/\pi(D/2)^4$, blood flow $\mathcal{Q} = (\mathcal{V}/1.35) \times \pi(D/2)^2$, where $\mathcal{V}$ is the RBC velocity, incorporating the Fåhræus effect, RBC Transit time, $T = L/\mathcal{V}$, and hematocrit, $H = (100 \times 4 \times F_{rbc} \times MCV)/(\pi D^2 V)$, where MCV (mean corpuscular volume) was determined to be $63.5 \pm 0.3$ µm$^3$ for hamster RBCs. The study examined 218 capillary bifurcations, where fractional flow, $\mathcal{Q}^\star = \mathcal{Q}_1/(\mathcal{Q}_1 + \mathcal{Q}_2)$ and fractional RBC flux, $\mathcal{F}^\star = \mathcal{F}_1/(\mathcal{F}_1 + \mathcal{F}_2)$ were calculated to assess preferential RBC distribution.

Presson et al.[29] investigates capillary recruitment and transit time in the rat lung, focusing on how changes in blood flow and pressure affect MTT and gas exchange efficiency. In this study, the researchers used isolated, pump-perfused rat lungs to measure CTT under varying conditions, including increased flow and elevated venous pressure. Their goal was to determine how capillary recruitment and transit time distribution influence oxygen uptake, particularly in species with high metabolic rates like rats, which may have limited gas-exchange reserves compared to larger animals. To measure transit times, the researchers employed indicator dilution techniques using fluorescein isothiocyanate-dextran as a plasma marker. Dye injections were made into the pulmonary artery, and passage through subpleural capillaries was recorded via video microscopy. The input (arteriolar) and output (venular) dye concentration curves were analyzed to derive the CTT distribution. The mean transit time, $\bar{t}$ was calculated via numerical integration. The variance $\sigma^2$ and relative dispersion

$RD = \sigma/\bar{t}$ of transit times were also computed to assess distribution homogeneity.

### 2.1.2 Mathematical Models

Various mathematical models have been proposed to calculate CTT and MTT, ranging from probabilistic frameworks to network flow. Karst et al.[30] presents a methodology for calculating the MTT in microvascular networks by analyzing transit time distributions across multiple steady-state configurations. The approach focuses on the probabilistic pathways of RBCs through the network, incorporating flow dynamics, hematocrit distribution, and network geometry. The authors apply this methodology to three types of mesh networks, namely, regular honeycomb, perturbed honeycomb, and fully random, each having distinct geometric properties. For each network, they identify multiple equilibrium states by solving nonlinear systems of equations governing flow, pressure, and hematocrit. The calculation of MTT begins with defining the transit time for a single capillary, derived from the ratio of vessel volume to flow rate ($\tau = V/Q$). For a network, the transit time of a RBC traversing a specific pathway is the sum of transit times across all vessels in that path. The probability of an RBC taking a particular pathway is determined using a Markovian assumption, where the likelihood of transitioning to the next vessel depends only on the current vessel instead of the entire history. This simplifies the pathway probability calculation to a product of conditional probabilities as follows.

$$P(v_1, v_2, v_3, ..., v_n) = P(v_1) \prod_{i=1}^{n-1} P(v_{i+1}|v_i) \tag{2.12}$$

where $P(v_1)$ is the probability of entering the network through vessel $v_1$, and $P(v_{i+1}|v_i)$ is the probability of moving to vessel $v_{i+1}$ given the current vessel $v_i$. These probabilities are derived from RBC flow rates and hematocrit values at each bifurcation. The transit time distribution is constructed by enumerating all possible pathways from inlets to outlets, computing their associated transit times, and summing the probabilities of pathways with identical transit times. The MTT is then simply the first moment of this distribution,

representing the average transit time across all pathways.

Huang et al.[31] presents a stochastic simulation model to calculate the MTT of red blood cells in the human pulmonary circulation, incorporating anatomical and elasticity data of pulmonary blood vessels. The model simplifies the complex vascular network by converting connectivity data into probability matrices, enabling efficient computation of transit times without reconstructing the entire vascular structure. The approach focuses on steady blood flow conditions and incorporates the hierarchical branching of pulmonary arteries, capillary sheets, and veins. The method begins with morphometric and elastic property data derived from silicone elastomer casts of human pulmonary vessels. The vessels are organized using the Diameter-Defined Strahler System, which classifies them into 15 orders for both arteries and veins. Connectivity matrices describe the branching patterns between these orders, and these matrices are transformed into probability matrices. These probabilities determine the paths red blood cells take through the network, simulating their flow stochastically. For each path, the transit time is calculated by summing the times spent in arterial segments, the capillary sheet, and venous segments.

In Huang's work, the pressure-flow relationships in arteries and veins are modeled using Poiseuille's law, adapted for elastic vessels. The vessel diameter $D$ changes linearly with transmural pressure $\Delta P$, as described by $D/D_0 = 1 + \beta\Delta P$, where $D_0$ is the zero-pressure diameter and $\beta$ is the compliance coefficient. The flow rate $Q$ in each vessel segment is derived from a fifth-power law as follows.

$$\frac{640\mu\beta D_0 L}{\pi} Q = D_0^5 \left[ (1 + \beta\Delta P_{entry})^5 - (1 + \beta\Delta P_{exit})^5 \right] \tag{2.13}$$

where $\mu$ is blood viscosity, $L$ is vessel length, and $\Delta P_{entry}$ and $\Delta P_{exit}$ are transmural pressures at the segment ends. The capillary sheet is modeled using sheet flow theory, where the thickness $h$ depends on the pressure difference between blood and alveolar gas satisfying

$h = h_0 + \alpha(P - P_A)$. The flow rate through the capillary sheet is given by

$$\dot{Q} = k\Big\{\big[h_0 + \alpha(P_{art}P_A)\big]^4 - \big[h_0 + \alpha(P_{ven}P_A)\big]^4\Big\} \tag{2.14}$$

where the constant $k$ incorporates geometric and viscous factors. Transit times for individual segments are calculated by integrating the flow rates and volumes. For example, the volume V of an elastic vessel is given by

$$V = \frac{\pi}{4}D_0^2 L\big(1 + \beta P_{entry} + \beta P_{exit} + \frac{1}{3}\beta^2 P_{entry}^2 + \frac{1}{3}\beta^2 P_{exit}^2 + \frac{1}{3}\beta^2 P_{entry}P_{exit}\big) \tag{2.15}$$

where $P_{entry}$ is the pressure at the entrance and $P_{exit}$ is the pressure at the exit of the vessel. The transit time for such a segment is then $V/Q$. The total transit time for a red blood cell is the sum of times across all segments in its path. By simulating thousands of such paths, the model generates a frequency distribution of transit times from which the MTT is derived.

Payne et al.[32] present a comprehensive approach of calculating the MTT in vascular networks, focusing on how transit time distributions encode information about vascular structure and flow dynamics. The analysis begins with the fundamental equation for transit time (TT) in a single vessel, derived from the Hagen-Poiseuille equation, which states that TT depends on the driving pressure drop $\Delta P$, blood viscosity $\mu$, and the geometric ratio of vessel length to radius $(L/R)$. For a single vessel, the transit time T is given by

$$T = \frac{8\mu}{\Delta P}\left(\frac{L}{R}\right)^2 \tag{2.16}$$

This equation is extended to a pathway $i$ consisting of multiple vessels, where the total transit time $T_i$ is the sum of the transit times of each vessel along the pathway.

$$T = \sum_{j=1}^{J_i} \frac{8\mu_{ij}}{(\Delta P)_{ij}}\left(\frac{L}{R}\right)_{ij}^2 \tag{2.17}$$

Here, $J_i$ represents the number of vessels in pathway $i$, and $\Delta P_{ij}$ is the pressure drop across vessel $j$ in pathway $i$. The constraint that the total pressure drop across the network $\Delta P_N$ is the sum of the pressure drops across all vessels in any pathway is also imposed. To simplify the calculation, the pressure drop fraction $x_{ij}$ is introduced, defined as $x_{ij} = \Delta P_{ij}/\Delta P_N$. This allows the transit time to be rewritten in terms of non-dimensional viscosity $\mu'_{ij}$ and slenderness ratio $s_{ij}$, where $\mu'_{ij} = \mu_{ij}/\mu_0$ and $s_{ij} = (R_{ij}/R_0)/(L_{ij}/L_0)$. The characteristic values $R_0$ and $L_0$ are used to define a small parameter $\epsilon = R_0/L_0$ . The transit time expression then becomes,

$$T_i = \frac{8\mu_0}{\Delta P_N \epsilon^2} \sum_{j=1}^{J_i} \frac{\mu'_{ij}}{x_{ij} s_{ij}^2} \tag{2.18}$$

The paper further connects MTT to the network's permeability $k_p$, which relates the network flow rate $q_N$ to the pressure drop $\Delta P_N$ by $k_p/\mu_0 = q_N/\Delta P_N$. Substituting this into the transit time equation yields

$$T_i = \frac{8k_p}{q_n \epsilon^2} \sum_{j=1}^{J_i} \frac{\mu'_{ij}}{x_{ij} s_{ij}^2} \tag{2.19}$$

The central volume principle (CVP) is then employed to relate MTT to cerebral blood volume (CBV) and cerebral blood flow (CBF) as $MTT = CBV/CBF$.

Goirand et al.[33] investigates the role of microvascular network architecture in determining blood flow and transport quantities, including the MTT of blood through the cerebral microcirculation. The study employs highly resolved simulations of blood flow in microvascular networks with high degree of anatomical realism, coupled with a Continuous-Time Random Walk (CTRW) theory, to analyze the distribution of blood travel times and their implications for oxygen delivery and waste clearance. The authors simulate blood flow in a dense capillary network ($\sim$ 15,000 vessels) that was digitized from a mouse cortex, incorporating non-linear behavior of blood rheology and red blood cell dynamics. The flow rate $Q$ in each vessel is computed, and the transit time $t$ for a single vessel is derived as $t = l\pi d^2/4Q$, where $l$ is vessel length and $d$ is diameter. The probability density function of vessel transit times

follows a Cauchy distribution given by the following equation.

$$p_t(t) = \frac{2}{\pi t_c}\left(\frac{1}{1+(\frac{t}{t_c})^2}\right) \tag{2.20}$$

Where, $t_c$ is a characteristic transit time. This distribution exhibits a power-law decay $p_t(t) \sim t^{-2}$ for long transit times, reflecting the broad heterogeneity of flow rates in the network. The authors develop a mean-field transport model to describe the PDF of network travel times $p_T(T)$, which transitions from a power-law to a stretched exponential behavior.

$$p_T(T) \sim \left((T-T_0)/\tau_1 + L_0\right)^{-2} \qquad \text{for } T < T_c\ , \tag{2.21}$$

$$p_T(T) \sim \left(\frac{T}{T_c}\right)^{-3/4} \exp\left(-\frac{L_c}{L^*}\left(\frac{T}{T_c}\right)^{1/4}\right) \qquad \text{for } T > T_c\ . \tag{2.22}$$

where $L_0$ and $L_c$ are characteristic lengths, $L^*$ is a parameter of the exponential decay, and $\tau$ is the diffusion time. This model accounts for the dipole-driven (i.e., driven by a source and a sink) distribution of trajectory lengths and provides a good approximation for oxygen transport, which is dominated by shorter travel times. For solutes with lower diffusivity, such as amyloid-$\beta$, the authors extend the model using CTRW theory to incorporate random flow fluctuations in the capillary network, yielding a power-law decay $p_T(T) \sim T^{-3}$.

## 2.2 Path Tracing Techniques: A Dosimetric Perspective

Radiation dosimetry is the scientific measurement, calculation, and assessment of the absorbed dose delivered by ionizing radiation to matter. It is a fundamental aspect of radiation protection, medical imaging, and cancer therapy, used to ensure that radiation is administered safely and effectively in diagnostic and therapeutic procedures. Dosimetry involves quantifying how much energy from radiation is deposited in a given mass of material, usually expressed in units such as the gray (Gy) or sievert (Sv), depending on the context.

Radiation dosimetry plays a vital role in both external beam radiotherapy and radiopharmaceutical therapy, focusing on the accurate calculation of absorbed doses in both target and surrounding healthy tissues. Its goal is to maximize therapeutic effectiveness while minimizing potential side effects.

Dose calculation primarily relies on solving the Boltzmann Transport Equation (BTE). Deterministic and stochastic methods are the two main approaches for tackling this equation. Deterministic methods solve the transport equation directly using numerical techniques like the finite difference or the finite element methods. These approaches provide smooth, fast, and repeatable results by approximating the solution to the Boltzmann transport equation under defined boundary and source conditions. They are efficient for simple geometries and high-throughput clinical planning systems but may struggle with highly heterogeneous media, complex geometries, or low-dose regions due to resolution and approximation limits. In contrast, stochastic methods, primarily Monte-Carlo (MC) simulations, rely on random sampling of particle histories to statistically estimate energy deposition and radiation transport. At its core, the Monte-Carlo method involves simulating a process many times with randomized inputs drawn from known probability distributions. The law of large numbers ensures that, as the number of simulations increases, the results converge to an accurate approximation of the true value. This makes the method particularly useful for modeling phenomena with inherent randomness or complex geometries. These methods track millions of particles through detailed geometries, using probabilistic models for interactions based on cross-section data. Monte-Carlo methods are widely considered the gold standard for dose calculations because of their high accuracy and versatility, particularly in complex anatomical regions or mixed radiation fields.

### 2.2.1 The Monte-Carlo Method

Monte-Carlo methods in radiation dosimetry simulate the complex journeys of particles, such as, photons, electrons, and neutrons, through matter, scoring energy depositions to evaluate absorbed dose[34]. In software packages such as MCNP[35] and PHITS[36], the primary objective

is to numerically solve the BTE, which governs how particles interact with heterogeneous media. The continuous-energy Boltzmann transport equation for a particle species is as follows[8].

$$\frac{1}{v}\frac{\partial\psi(r,E,\Omega,t)}{\partial t} + \Omega\cdot\nabla\psi + \Sigma_t(r,E)\psi = \int_E\int_{4\pi}\Sigma_s(r,E'\to E,\Omega'\to\Omega)\psi\ dE'd\Omega' + S \tag{2.23}$$

Where $\psi$ denotes angular flux as a function of position $r$, energy $E$, direction $\Omega$ and time $t$, $\Sigma_t$ and $\Sigma_s$ are total and scattering cross sections, and $S$ is the source term. Monte-Carlo simulation interprets this equation by tracking individual particles, also known as 'histories', from source emission until absorption or leakage, sampling interaction lengths, event types, scattering angles, and energy deposition based on underlying probability distributions sampled from nuclear and atomic cross-section databases.

The Monte-Carlo algorithm begins by sampling an initial position, direction, and energy from a defined source. The distance to the next interaction is found using the following formula[8].

$$l = -\frac{ln\ \xi}{\Sigma_t(E)} \tag{2.24}$$

Where, $\xi$ is a uniform random number between 0 and 1. At each step, a collision is sampled according to the relative probabilities of competing interaction channels. For photons this might include photoelectric absorption, Compton scattering, or pair production; for electrons, a continuous-slowing-down approach with condensed history methods is employed. A detailed treatment of this method can be found here[8].

Commercial codes like MCNP typically tally doses via energy deposition or track-length flux tallies graded by cell. For example, the local absorbed dose in a volume $V$ is estimated

by the following formula.

$$D = \frac{1}{\rho V} \sum_{j=1}^{n} w_j E_{dep,j} \tag{2.25}$$

Where, $w_j$ is the statistical weight, $E_{dep,j}$ is energy deposited during the $j$th history in that cell, and $\rho$ is the mass density. Dose uncertainty is quantified by tracking the sample variance, which typically converges as $1/\sqrt{N}$, N being the number of histories. Dose scoring may also use fluence-based estimators such as mass-energy-absorption coefficients.

$$D = \int \psi(r, E)\ \mu_{en}(E) \frac{E}{\rho}\ dE \tag{2.26}$$

Where, $\mu_{en}$ is the energy-absorption coefficient. Alternatively, direct energy deposition tallies are used, especially with coupled photon-electron transport.

### 2.2.2 Existing MC frameworks, software packages and their use in dosimetry

Several MC frameworks and software packages have been developed, each with unique features tailored to specific applications in reference dosimetry, detector response simulations, and treatment planning. Among the most widely used MC systems are EGSnrc[37], PENELOPE[38], GEANT4[39], MCNP[35], PHITS[36], and FLUKA[40], each employing different algorithms for particle transport, particularly in handling electron interactions and interface effects[34].

EGSnrc, an evolution of the EGS4 system, is one of the most established MC codes in medical physics. It incorporates advanced electron transport algorithms such as PRESTA[41] (Parameter Reduced Electron-Step Transport Algorithm) and PRESTA-II[42] to address boundary-crossing artifacts and improve accuracy in heterogeneous media. EGSnrc is widely used for calculating stopping-power ratios (SPRs), perturbation correction factors for ionization chambers, and small-field dosimetry. The BEAMnrc[43] and DOSXYZnrc[44] user codes, built

on EGSnrc, specialize in simulating linear accelerator (linac) treatment heads and patient dose distributions, respectively. These tools are critical for validating treatment planning systems (TPS) and benchmarking experimental measurements.

PENELOPE (Penetration and Energy Loss of Positrons and Electrons) is another robust MC system, known for its sophisticated handling of low-energy electron transport and condensed-history techniques. Unlike EGSnrc, PENELOPE avoids interface artefacts by dynamically adjusting step sizes near material boundaries. This makes it particularly suitable for simulating ionization chambers and other detectors where electron scattering effects are significant. User codes like PENLINAC[45] and PRIMO[46] extend PENELOPE's capabilities to model clinical linacs and compute 3D dose distributions in patient CT datasets. PRIMO, for instance, integrates linac head simulations with patient dose calculations, providing a streamlined workflow for clinical applications.

GEANT4, originally developed for high-energy physics, has been adapted for medical dosimetry due to its flexibility in geometry modeling and support for diverse particle types. It employs an interaction-by-interaction approach, making it highly accurate but computationally intensive. The GAMOS[47] framework simplifies GEANT4 for medical applications, offering pre-configured physics models and scoring options for radiotherapy simulations. GEANT4 is often used in proton and heavy-ion therapy, where nuclear interactions play a significant role, as well as in brachytherapy dose calculations.

MCNP (Monte-Carlo N-Particle), developed by Los Alamos National Laboratory, is widely used in radiation protection and shielding but also finds applications in radiotherapy. MCNP6, the latest version, includes enhanced electron-photon transport and support for complex geometries, making it useful for brachytherapy source modeling and kilovoltage (kV) dosimetry. However, its adoption in megavoltage (MV) photon beam simulations is less common compared to EGSnrc or PENELOPE due to historical focus on neutron and nuclear physics.

FLUKA, another multi-particle transport code, excels in simulating mixed radiation fields, including neutrons and high-energy hadrons. While less common in conventional photon/electron therapy, it is valuable in proton therapy and space radiation studies. FLUKA's

detailed nuclear interaction models make it suitable for secondary neutron dose calculations in radiotherapy bunkers and proton therapy systems.

MC simulations serve three primary roles in radiotherapy– reference dosimetry, detector response modeling, and treatment planning. MC calculates fundamental dosimetric quantities such as SPRs (e.g., water-to-air) and mass energy-absorption coefficients, which are essential for converting detector readings to absorbed dose. Codes like EGSnrc and PENELOPE are preferred due to their validated electron transport algorithms. MC models how detectors (ionization chambers[48], diodes[49], diamond detectors[50]) perturb radiation fields, correcting for effects like cavity displacement, wall attenuation, and stem scattering. The software packages employs various variance reduction techniques (e.g., correlated sampling) to efficiently compute chamber-specific correction factors. Such simulations are critical for small-field dosimetry, where detector size and composition significantly influence measurements. MC-based TPS (e.g., PEREGRINE[51], XVMC[52], DPM[53]) simulate dose distributions in patient CT datasets, addressing limitations of analytical algorithms in heterogeneous tissues.

## 2.3 Computational human phantoms in dosimetry

Computational human phantoms (CHPs) are digital models of human anatomy that play a crucial role in estimating radiation doses absorbed by tissues and organs. These models are widely used in medical imaging, radiation therapy, and radiation protection, where direct measurement of internal doses is difficult or in some cases impossible to determine. Over the years, CHPs have evolved from simple geometric representations to highly detailed, patient-specific models, enabling more accurate and personalized dose calculations[54;55]. Their development has been driven by advances in medical imaging, computational power, and simulation techniques, making them indispensable tools in modern dosimetry.

The earliest CHPs were stylized or mathematical phantoms, which used basic geometric shapes like spheres and cylinders to approximate organs and tissues. While computationally efficient, these models lacked anatomical accuracy. Voxel-based phantoms, derived from

CT or MRI scans, improved realism by representing anatomy as a 3D grid of voxels. However, their discrete nature introduced stair-step effects, limiting precision for small or thin structures. Boundary representation (BREP) phantoms, such as NURBS or polygon mesh models, overcame this by using smooth surfaces to define organ boundaries, allowing for deformations like posture changes and organ motion. Hybrid phantoms combine voxel and BREP techniques to balance accuracy and computational efficiency, while newer tetrahedral mesh phantoms further optimize simulations by reducing the number of surface facets.

Different MC packages utilize CHPs in distinct ways. Geant4, for example, supports BREP and tetrahedral mesh phantoms directly, enabling detailed simulations without voxelization. It is widely used in ionizing and non-ionizing radiation studies, including MRI safety assessments[56]. MCNP (e.g., MCNP6) and PHITS traditionally rely on voxel phantoms but are adapting to mesh formats for improved accuracy, particularly in radiation protection and nuclear medicine dosimetry. EGS4 and PENELOPE often employ voxel phantoms for radiotherapy and diagnostic imaging dose calculations. GPU-accelerated codes like GATE[57] leverage voxel or hybrid phantoms for rapid simulations in complex scenarios, such as 4D radiotherapy planning.

## 2.4 Combination of Hemodynamic Simulation and Particle Transport Using Computational Phantoms In Radiation Therapy Models

Particle transport using computational phantoms has been briefly discussed in section 2.3. Primarily it has been used for dose calculation in external radiotherapy and radiation protection purposes. But with the advancement of latest technologies like FLASH and various radiophermaceuticals for internal radiotherapy, accounting for the distribution of blood to various organs has become very important. Blood flow simulation tools, used in conjunction with particle transport, can potentially create highly accurate dose volume histograms.

Correa-Alfonso et al.[58] presented a novel computational approach to model the hepatic vasculature within the liver to enhance dosimetric accuracy for radiopharmaceutical therapies. The research focuses on differentiating radiation dose deposition between liver parenchyma and blood vessels, which is critical for accurate dose assessment in nuclear medicine. The study utilizes the International Commission on Radiological Protection (ICRP) adult mesh-type reference computational phantoms (MRCP)[59] for the adult male (AML) and female (AFL) livers. These phantoms are tetrahedral mesh models, which offer flexibility in representing complex anatomical structures compared to traditional voxel-based models. The liver was segmented into eight anatomical regions based on the Brisbane 2000 system[60], ensuring alignment with clinical liver anatomy.

To model the hepatic vasculature, the study employed a constrained constructive optimization (CCO)[61] algorithm to generate virtual binary trees representing the hepatic arterial (HA), hepatic portal venous (HPV), and hepatic venous (HV) circulations. The algorithm constructs these trees by iteratively adding vessel segments, ensuring adherence to physiological principles such as Poiseuille's law[62] for blood flow and Murray's law[63] for vessel bifurcations. The vessels were modeled as rigid cylindrical pipes with radii ranging from several millimeters down to 0.1 mm, excluding smaller structures like capillaries and sinusoids. The algorithm updated pressures and flow rates dynamically as new vessels were added, maintaining conservation of blood flow and minimizing intersections between vascular trees. The study used the PHITS Monte-Carlo radiation transport code to simulate energy deposition from alpha particles, electrons, positrons, and photons accounting for radionuclide decay sites within the liver vessels as well as outside of the vessels within the liver blood pool. The tetrahedral mesh models were coupled with PHITS to compute specific absorbed fractions (SAFs), which quantify the energy deposited in target regions per unit source activity. The absorbed dose $D(r_T)$ to a target region $r_T$ was calculated using the MIRD schema[64], which is as follows.

$$D(r_T) = \sum_{r_s} \tilde{A}(r_s) S(r_T \leftarrow r_s) \tag{2.27}$$

Where, $\tilde{A}(r_s)$ is the time-integrated activity in the source region, and $S(r_T \leftarrow r_s)$ is the mean absorbed dose to the target region per nuclide decay in the source region.

The 2021 study by Shin et al.[65] introduces Hematological Dose (HEDOS), a computational framework designed to estimate radiation dose to circulating blood cells during external beam radiotherapy. HEDOS employs a discrete-time Markov process to simulate blood circulation across 28 organs, based on ICRP Publication 89[66] reference values for blood volumes and flow rates. The framework models blood as discrete Blood Particles (BPs), each representing 0.053 mL of blood, and tracks their spatiotemporal distribution. They use the transition probability matrix, $\mathbf{P}$, to simulate the Markov process. The matrix consists of elements like the following.

$$p_{ij} = \frac{F_j}{V_i} \tag{2.28}$$

Here, $p_{ij}$ is the probability of a BP moving from organ i to organ j, $F_j$ is the outflow rate to organ j, and $V_i$ is the volume of organ i. To ensure realistic blood flow dynamics by preventing newly entered BPs from exiting too quickly, a time-dependent Weibull model is used.

$$l_i(\tau; \lambda, \kappa) = 0.5\big(1 - \exp(-(\tau/\lambda)^\kappa)\big) \sum_{i \neq j} p_{ij} \tag{2.29}$$

Here, $\tau$ is residence time, and $\lambda, \kappa$ are Weibull parameters. The model accounts for recirculation, where BPs may re-enter irradiated organs multiple times during treatment, significantly affecting cumulative dose. For dose calculation, HEDOS convolves the blood path distribution with time-dependent organ dose-volume histograms (DVHs) from treatment plans. The dose to each BP is computed by randomly sampling dose values from DVHs during irradiation and accumulating dose over time, accounting for re-entry into irradiated fields.

The study by Shu Xing et al.[9] presents a novel four-dimensional (4D) dynamic liver blood flow model designed to estimate the absorbed dose to circulating blood cells, particularly

lymphocytes, during liver-directed external beam radiotherapy. The study utilized polygon-mesh computational phantoms derived from the International Commission on Radiological Protection (ICRP) reference adult male (AM) and adult female (AF) models[66;67]. These phantoms included detailed anatomical representations of the liver, segmented into eight functional regions based on the Couinaud classification[68;69] to reflect physiological blood supply patterns. This study combines the method developed by Correa-Alfonso et al.[58] and Shin et al.[65] to model the vasculature and the blood flow. The vascular trees were constructed using an in-house algorithm based on the CCO method.

The study employed a two-tiered approach to simulate blood flow: whole-body circulation and explicit tracking within the liver vasculature. For whole-body circulation, a discrete-time Markov Chain model was used to simulate the spatiotemporal distribution of blood particles (BPs) across 28 organs. Each BP represented a finite volume of blood cells, and its trajectory was determined probabilistically based on organ-specific blood volumes and flow rates derived from ICRP Publication 89[66]. The model simulated 100,000 BPs with a 1-second time resolution over a 10-minute period, ensuring statistical robustness. Key parameters included cardiac outputs of 6.5 L/min (AM) and 5.9 L/min (AF) and liver residence times of 19.2 s (AM) and 14.4 s (AF).

For BPs entering the liver, an explicit Monte-Carlo simulation was implemented to track their propagation through the vascular trees. The simulation recorded the spatial coordinates of each BP every 0.1 seconds as it traversed the HA, PV, or HV trees. BPs entering via the HA or PV trees were routed probabilistically at bifurcations, with branching probabilities proportional to the squared vessel radii in accordance with Murray's law. Upon reaching terminal vessels, BPs transitioned to the HV tree and exited the liver via the inferior vena cava. This approach allowed for precise dose accumulation as BPs interacted with time-varying radiation fields. The dose to circulating blood was computed by integrating the dose rate over the BP paths during radiation delivery. The accumulated dose for a BP after one

fraction was calculated as follows.

$$d_i = \sum_k d_k(x,t)\Delta t \tag{2.30}$$

where $d_k(x,t)$ is the dose rate at position $x$ and time $t$, and $\Delta t$ is the time step (0.1 s).

The study by Hammi et al.[70] introduces a four-dimensional (4D) computational blood flow model designed to estimate radiation dose to circulating blood cells, particularly lymphocytes, during intracranial radiotherapy. By integrating detailed vascular anatomy, explicit blood particle tracking, and dynamic dose accumulation, the framework provides insights into how treatment parameters, such as modality, dose rate, and patient physiology, affect lymphocyte depletion. The study combines anatomy-based and generic computational voxel phantoms to simulate cerebral blood flow. Major vasculature (e.g., anterior/posterior cerebral arteries, superior sagittal sinus) was segmented from high-resolution 3D MRI data (T1/T2-weighted) using thresholding and 3D thinning algorithms in MATLAB. The blood flow model uses explicit Monte-Carlo tracking of blood particles (BPs) to model spatiotemporal dose accumulation. A Markov Chain approach simulates BP distribution across 32 organ compartments (e.g., heart, lungs) based on ICRP Publication 89[66] hemodynamic data. The model accounts for cardiac output (6.5 L/min for adults), blood volume (5.3 L), and organ-specific flow rates. For BPs entering the brain, the model tracks their propagation along vascular paths with a time resolution of 10 ms. The BP count is derived as follows.

$$N_B = \sum_i \frac{f_{BP}}{\bar{v}} \int p_i \, dxdydz \tag{2.31}$$

Here, $f_{BP}$ is the pulsing rate, $\bar{v}$ is average blood speed (90 mm/s), and $p_i$ represents vascular trajectories. Dose to each BP is computed by integrating dose rates along its path during beam delivery.

$$D_{ID} = \sum_{path}^{N} \frac{\dot{d}(x,t)}{\bar{v}(x)} \Delta x \tag{2.32}$$

Where, $\dot{d}(x,t)$ is the voxel-specific dose rate, $\Delta x$ is the step length, and $N$ is the number of BP re-entries into the radiation field.

Beekman et al.[71] proposed an improved method over HEDOS[65]. Beekman divided the human body into 32 organ compartments (e.g., heart, lungs) based on ICRP Publication 89 hemodynamic data (blood volume, flow rates). Blood flow is modeled as a stochastic Markov process, where blood particles (BPs) transition between compartments with dwell-time-dependent probabilities. For high-resolution dose calculation, organs like the liver or lungs can be replaced with detailed vasculature graphs (e.g., hepatic arterial trees). These are represented as directed graphs. A surrogate capillary vessel corrects for unmodeled microvasculature, preserving MTT. The model tracks 100,000 BPs, which is scalable as per the user's requirement, with a 50 ms time resolution to simulate continuous flow.

The extraordinary improvement that this work offer over HEDOS is the use of diffeomorphic image registration, i.e., to warp phantom vasculature to patient anatomy while preserving topology. It introduces patient-specific adjustments (e.g., cardiac output, tumor perfusion) via imaging or literature. It also introduced random walk for BPs in stochastic compartments instead of uncorrelated jumps in HEDOS, better mimicking vascular flow. Instead of assuming exponential transit times, which causes equilibrium shifts, this work uses Weibull distributions (corresponds to $\kappa = 2$ in Eq. 2.29) to ensure realistic transit delays. It introduces a hazard function based on survival analysis to correctly model dwell-time-dependent transitions, where HEDOS relies only on the Weibull distribution. The hazard function is given by

$$p(\tau) \simeq h(\tau)\Delta t = \frac{f(\tau)\Delta t}{s(\tau)} \tag{2.33}$$

Here, $h(\tau)$ is the hazard function which describes the probabilistic rate at which particles leave, $s = 1 - F$ is the survival function, where $F$ is the cumulative density function of transit times, and $f(\tau)\Delta t$ is the probability the particle leaves in the time window $\tau + \Delta t$.

## 2.5 Challenges of Using Existing Methods for Path-Tracing in Computational Phantoms

At this juncture, it is important to take a closer look at the existing literature mentioned so far and make evaluations on how they fall short in addressing the goals of this research. The primary goal of the current research is to develop a path-tracing framework that can follow the vascular networks inside the phantom. The developed framework should be flexible and robust so as to meet patient-specific requirements, easily transferrable to different types of phantoms, and accommodating to facilitate determination of secondary quantities, such as MTT.

The first challenge to achieve these goals is to determine a computational phantom that not only provides a realistic representation of the vascular networks but also preserves the anatomical accuracy, i.e., actual structure, surface, and volume of a patient's body or a particular organ of interest. The mesh phantoms are highly accurate in representing the surface of the organ. They are developed using voxel phantoms by fitting analytical surfaces over the outer periphery. This is a toilsome process that requires tremendous effort and pre-processing. The voxel phantoms are generated with greater ease using CT/MRI imaging data. This takes much less time and effort than the mesh phantoms, which translates to high patient specificity. Voxel phantoms conserve organ-volume, which is essential in dose calculation. The key setback of using traditional voxel phantom is its stair-step surface condition. This stair-step effect introduces overestimation in surface area which results in error in temperature distribution. Amare et al.[72] proposes a structured mesh cleaving method which can reduce the surface error to only 16%, which makes the use of voxel phantoms more promising. Hence, this work will focus on using voxel phantoms.

The next challenge is to obtain a realistic vascular network for the flow simulation. In voxel phantoms, vascular structures are segmented from the imaging data. The vasculature in the human body ranges from centimeters to microns in radius, with typical values being 1.25 cm for aorta, 3 µm at the capillary bed, and 1.5 cm at vena cava[73]. CT/MRI imaging

devices cannot resolve features across this range. It can only resolve up to a few millimeters. Hence, a large portion of vascular structures are lost if voxel phantoms are used and the network becomes discontinuous. To simulate the vessels beyond this point, one has to perform mathematical modeling of blood vessels or use some vasculature generation algorithm. The works of Correa-Alfonso et al.[58], and Xing et al.[9] rely on algorithmic vascular generation using CCO model. They grow the vascular network up to 100 µm diameter, covering an acceptable range of diameters. But the challenge of using this method with voxel phantoms is that the modeling of smaller vessels require smaller voxels, which can cause the total voxel count to skyrocket. Consequently, it will become a computational burden. Another important aspect of Correa-Alfonso's and Xing's works is that the arteries are directly connected with the veins at their terminal end. They completely disregard the capillary bed. Blood flow is the slowest in capillary bed and important phenomena like gas and nutrients exchange occur at this level. Omitting them introduces major errors in flow distribution across the tissues and makes the model unfit for many potential uses like study of oxygen exchange and MTT calculation. Hodneland's[74] work proposes a mathematical model to simulate the pressure continuity of the blood flow beyond the segmentable vessel. In his work, flow in the capillary bed is modeled by a porous medium assumption while the unresolved vasculature representing arterioles and venules smaller than the segmented vessels but bigger than the capillary bed is modeled by a pressure drop parameter accounting for the flow resistance of this level.

Another challenge in employing voxel phantom is to find a suitable blood flow model that successfully couples the 1D vessel flow with 3D porous medium. The VaPor model by Blowers et al.[75] provides a solution to this problem. It takes all the voxels that intersects a terminal vessel and exchanges blood with these voxels, while the other voxels rely solely on perfusion. This mass transfer across the domains is controlled by the inter-domain mass transfer parameter. This model lacks the ability to couple pressure gradient with the inter-domain mass transfer. Moreover, calculation of flow rate at every terminal becomes difficult in large domains. A more robust way to couple the terminals to the tissue voxels is found in the works of Heltai et al.[76] In this work, the tissue is modeled as a 3D elastic matrix, while

the vasculature is represented as a 1D network of cylindrical vessel segments. Each vessel is defined by its centerline and radius. The coupling is achieved by introducing hypersingular forcing terms in the 3D elasticity equations. These terms represent the effect of blood pressure on the tissue without explicitly resolving the 3D vessel geometry. They use the Dirac delta function, approximated by a modified cosine function, providing a smooth and compact support to enable numerical implementation. This model very efficiently handles the decoupling of 1D vasculature from 3D mesh, enabling efficient simulation of complex networks. It also avoids explicit 3D discretization of thin vessels, relying instead on 1D centerline data. However, this method does not have any provision to handle the oxygenated and deoxygenated state of blood. Hodneland's[74] framework provides a complete model of blood flow simulation encapsulating both 1D vessels representing segmentable arteries and veins and the 3D tissue approximated by two-compartment porous medium. In this model, the blood flow in arterial and venous vessel is modeled with classical Hagen-Poiseuille pipe flow equations, whereas the capillary bed is modeled using Darcy's equation for porous medium. The unsegmented vasculature, which is the point of coupling in 1D-3D domain, is governed by a Dirac delta distribution with the pressure coupling provided by the pressure drop parameter. Later Amare, in his 2020[72] and 2022[77] work, adapted this method into a full fledged multiphysics simulation framework, named VoM-PhyS, to simulate mass flow and heat transfer in voxelized domains. The present work adopts this framework for the blood flow simulation. A more detailed overview of this framework is given in section 3.1.

Finally, the last component of a complete blood-flow driven path-tracing framework is the path-tracing algorithm. The existing Monte-Carlo algorithms are developed to facilitate the path tracing of subatomic and charged particles like proton, neutron, photon, electron and alpha particles. These particles take random tracks according to their respective interaction probabilities (i.e., cross sections) through the given medium. Hence, the existing MC packages cannot be readily used to track the blood corpuscles or other particles of interest that follow the vasculature. The work of Shin et al.[65] suggests a discrete time Markov process to simulate the probabilistic nature of blood particle tracks, but this method cannot be used directly in the case of this study, because it generates the path distribution using

transition probabilities depending on whole body organ network, not explicitly described vascular tree. Xing et al.[9] proposes a modified Monte-Carlo simulation for the path tracing through the vascular tree inside the liver. In this work, BPs entering via the HA or PV trees were routed probabilistically at bifurcations, with branching probabilities proportional to the squared vessel radii. This model also fails to be applicable to the current study because of the nature of vascular tree it uses. The vascular tree used in this work is shunted at the arterial terminal with the venous terminal, which disregards capillary bed. For the purpose of the current work, a new Monte-Carlo framework relying solely on flow rate will be developed in chapter 3, which accommodates not only tracing inside the vasculature, but also the capillary bed and the conjunction of these two domains.

## 2.6 Research Goals Revisited

Section 2.5 elaborates on the challenges in applying the current state-of-the-art presented in the preceding sections to meet the aims of the current research. It also points out the junctures where the current research can take up the existing knowledge and use it to advance the goal of this study. This section summarizes the goals of this research, outlining how insights gathered from the literature review will be applied to accomplish the intended goals.

- To represent the anatomical structures and vascular geometry, this study will resort to the voxelized domains used in the works of Hodneland[74] and Amare[77]. The imaging data and computational domains available from the stated works will be used throughout this work.

- To simulate the blood flow in the stated domain, the VoM-PhyS Framework developed by Amare et al.[77] will be invoked. The details of this simulation procedure will be described in chapter 3. The pressure map obtained from the simulation will be heavily relied on to develop the intended path tracing framework.

- Since no existing MC framework suits the purpose of the current study, a new path-tracing framework inspired by the ideas of MC methods will be developed in chapter 3.

This framework will depend on the flow rate at desired locations to generate the random paths. The framework will also include the calculation of transit time in each path accommodating for the time elapsed in the unsegmented vasculature.

- Chapter 4 will show the results obtained from the simulation of the proposed framework, discuss its important features, and establish its validity.

# Chapter 3

# The Path Tracing Framework

A brief review of various path tracing frameworks and algorithms is provided in chapter 2. Limitations of these methods in accommodating the needs of the current study have also been discussed. The current chapter describes a novel path tracing framework to address the goals of the current study. This path tracing framework is developed based on the VoM-PhyS Framework[77], which is a multidimensional coupled blood flow and heat transfer solver that operates on voxel phantoms. The proposed framework uses the blood flow modality of VoM-PhyS and directly uses the results from the blood flow solver to calculate various quantities that are useful in different stages. The framework is implemented in the voxelized frog tongue data found in the literature to demonstrate its functionality.

## 3.1 The VoM-PhyS Blood Flow Solver

A brief review of the blood flow solver within the VoM-PhyS framework is warranted to ensure continuity and coherence with the path-tracing framework. The VoM-PhyS blood flow solver relies on Hodneland's[74] mixed-dimensional blood flow simulation framework, which models macro and micro scale blood flows in a coupled fashion for continuous blood flow. A schematic of the mixed-dimensional framework is provided in Figure 3.1. In the

macro-scale, the flow is governed by the Hagen-Poiseuille pipe flow equation.

$$\dot{q}_{ji} = \frac{\pi R_{ji}^4}{8\mu L_{ji}}(p_j - p_i) \tag{3.1}$$

Here, $\dot{q}_{ji}$ is the flow rate from node $j$ to node $i$, the radius and length of the vessel with end-nodes $j$ and $i$ are represented by $R_{ji}$ and $L_{ji}$ respectively. $\mu$ is the viscosity of blood and $p_k$ is the pressure at node $k$.

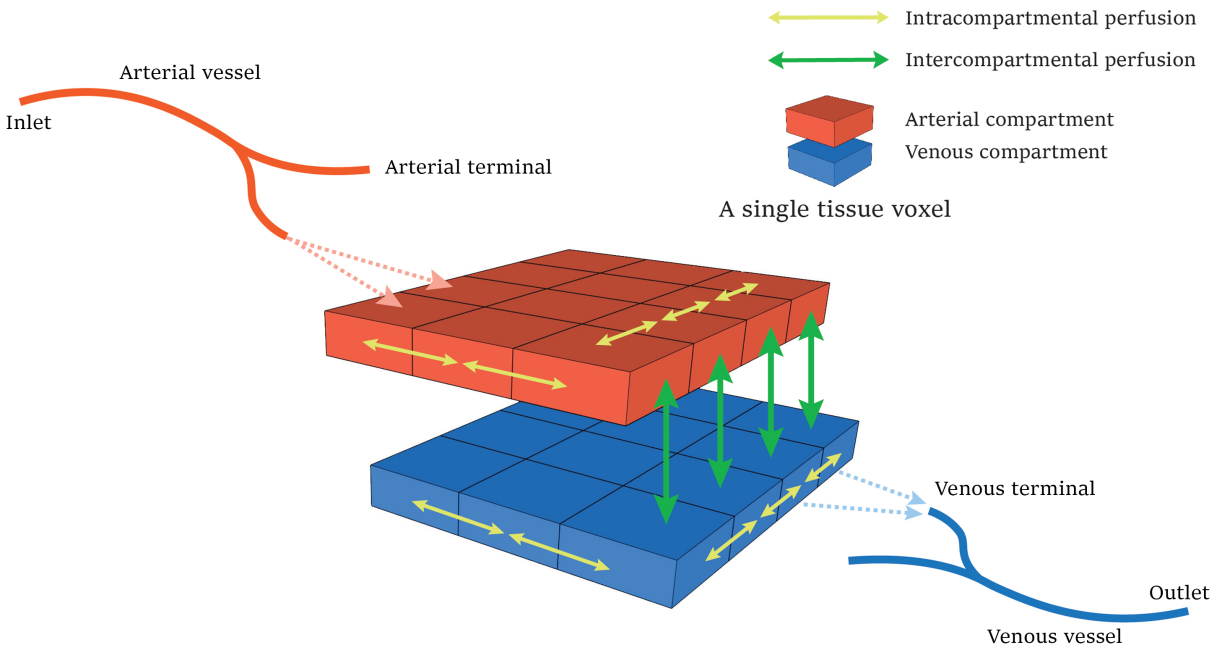


Figure 3.1: Mixed dimensional coupling proposed by Hodneland[74]. It shows the segmented vasculatures as tubes and the capillary bed as two-compartment porous medium. The 1D-3D discontinuity is also visible.

The macro-scale represents the segmentable blood vessels, i.e., vessels that can be recreated from CT or MRI imaging data. These vessels are modeled as 1D pipe networks. Blood is assumed to be a Newtonian fluid in a steady state laminar flow and pulsatile behavior is ignored. The micro-scale represents the capillary flow which is modeled as a 3D porous medium. The porous medium comprises of tissue and capillary bed, which is henceforth referred to as tissue domain. The transport of oxygen and carbondioxide occurs at this level. To accommodate the oxygenated and deoxygenated state of blood, each voxel in the tissue

domain is divided into two compartments, one representing the arterial capillary bed and associated tissue, the other representing the venous capillary bed and associated tissue. They are referred to as arterial compartment and venous compartment of the voxel, respectively. The flow in the tissue domain is dictated by Darcy's equation for porous medium, which is as follows.

$$u = -\frac{K}{\mu}\nabla P \tag{3.2}$$

where $K$ represents the permeability of the porous medium and $P$ is the pressure field. The equation is applicable to both the arterial and the venous compartments, demarcated by subscripts $a$ and $v$, respectively.

The transition of blood from oxygenated to deoxygenated state is represented by perfusion from arterial to venous compartment. This perfusion is driven by the pressure difference of arterial and venous compartment. The following equation governs this flow.

$$u_{perf} = \alpha(P_{a,i} - P_{v,i}) \tag{3.3}$$

Here, the parameter $\alpha$ is known as the perfusion proportionality factor, which represents the flow resistance between the compartments of a voxel. Incorporating Eq. 3.2 and Eq. 3.3 in the conservation of mass equation $\nabla \cdot u = G$,

$$-\nabla \cdot \left(\frac{K_a}{\mu}\nabla P\right) = -\alpha(P_a - P_v) + \sum_i G_{a,i} \tag{3.4a}$$

$$-\nabla \cdot \left(\frac{K_v}{\mu}\nabla P\right) = \alpha(P_a - P_v) - \sum_j G_{v,j} \tag{3.4b}$$

In Eq. 3.4a, the positive source term $G_a$ represents the emergence of oxygen-rich blood from arterial terminals and the negative perfusion term represents the relocation of blood to the venous compartment transitioning to deoxygenated state. Conversely, the negative source term $G_v$ in Eq. 3.4b represents the departure of deoxygenated blood to venous terminals and the positive perfusion term represents the relocation of blood from the arterial compartment.

A voxel can receive blood from multiple arterial terminals. Hence, in Eq. 3.4a, the sum of $G_a$ is over all such terminals. Similarly, a voxel can deliver blood to multiple venous terminals, which is represented by the sum over all such terminals in Eq. 3.4b.

The exchange of blood between a voxel and a terminal vessel, i.e., $G_a$ and $G_v$ is governed by the Dirac function, which is as follows.

$$G^{\epsilon}(x) = \int_{\Omega} G(y)\eta^{\epsilon}(x-y)dy \tag{3.5a}$$

$$\eta^{\epsilon}(x) = \frac{1}{\epsilon^n}\eta(\frac{x}{\epsilon}) \tag{3.5b}$$

$$\eta(x) = \begin{cases} C\ exp(\frac{1}{|x|^2-1}), & \text{if } |x| < 1 \\ 0, & \text{if } |x| \geq 1 \end{cases} \tag{3.5c}$$

$$\int_{\Omega} \eta^{\epsilon}(x)dx = 1 \tag{3.5d}$$

Eq. 3.5a gives the amount of blood that a voxel at location $x$ exchanges with a terminal artery or vein, where $G(y)$ represents the amount of blood flow in the terminal vessel. Each voxel receives a different amount of blood depending on its position $x$, i.e., the distance from the terminal. Each terminal has a characteristic radius $\epsilon$, which defines its sphere of influence (SoI). Only the voxels that falls inside the SoI of a particular terminal can exchange blood with that terminal, described by Eq. 3.5b. The superscript $n$ in Eq. 3.5b is the number of dimensions of simulation domain. Eq. 3.5c gives the precise definition of the function used in Eq. 3.5b, which is a modified normal distribution function. Finally, Eq. 3.5d gives the normalization condition, which means that summing the fractions of flow received by all the voxels inside the domain $\Omega$ of a particular terminal must give the total flow of that terminal.

The last equation that completes the system is the pressure continuity equation between the terminal and the voxels inside its SoI. In reality, a finer network of vessels exist beyond the terminal artery or vein, which is not resolvable due to spatial resolution limits of imaging and limitations of computational capabilities. However, these fine structures pose resistance to the flow. The following equation relates the pressure at the terminal vessel to the pressures

at the voxels, incorporating the resistance of the unresolved network.

$$\dot{q}_{\beta,k} = \frac{\gamma_\beta}{\mu}\left(p_{\beta,k} - \sum_j \eta^{\epsilon}_{\beta,k}(x_j - x_k)P_{\beta,j}V_j\right) \tag{3.6}$$

Here, $\dot{q}_{\beta,k}$ is the flow to terminal node $k$, $\gamma_\beta$ is the pressure drop parameter which represents the flow resistance in the unresolved network, $p_{\beta,k}$ is the pressure at the terminal node and $P_{\beta,j}$ is the pressure at the voxel. The subscript $\beta$ is a placeholder for either the arterial side $a$ or the venous side $v$.

Discretization of Eqs. 3.4a and 3.4b can be achieved by invoking the finite volume two-point flux approximation (TPFA)[78]. These discretized equations, along with Eqs. 3.1 and 3.6, form a complete set of linear equations that can be solved to get the pressure at each node inside the simulation domain. Detailed treatment of the discretization and matrix formation can be found in the original work of R. Amare et al[77].

## 3.2 The Path Tracing Framework

In accordance with the VoM-PhyS framework, the path that a particle of interest will follow is comprised of four segments. These include, the path traced in the arterial vasculature, the path traced in the arterial compartment of the tissue domain, the path traced in the venous compartment of the tissue domain, and the path traced in the venous vasculature. Each of these segments has its own rules of choosing steps to trace out a path in its own territory. The times taken at each step are also calculated using their respective formulae.

To define the framework for the proposed path-tracing algorithm, several simplifying assumptions are necessary. Firstly, the particles used for path tracing are modeled as point-like entities that do not undergo any chemical or nuclear interaction with the medium or each other. Additionally, these particles experience no collisions, either with vascular walls or other particles, and move purely advectively, possessing the same velocity as the local blood flow without perturbing it. Vascular junctions are assumed to behave as ideal mixing chambers, ensuring that path selection is independent of specific locations with respect to

the centerline of the vessel. Under these conditions, simulating $N$ particles is equivalent to randomly sampling $N$ paths according to the rules described below.

### 3.2.1 Path tracing in the arterial vasculature

The path-tracing algorithm begins at the inlet node and iteratively progresses through subsequent nodes, recording each traversed node. In the case of multiple inlets, an inlet is randomly chosen under the condition that all the inlet nodes are subject to equal probability of being chosen. At any branching node where multiple vessels diverge, the next node is selected stochastically according to a probability distribution proportional to the flow rate to that node from the current node. Specifically, if $n$ nodes branch from node $i$, the probability $\mathcal{P}_k$ of selecting node $k$ as the successor is given by:

$$\mathcal{P}_k = \frac{\dot{q}_{ki}}{\sum_{j=1}^{n} \dot{q}_{ji}} \tag{3.7}$$

where $\dot{q}_{ki}$ is the flow rate from node $i$ to node $k$. The flow rate $\dot{q}$ is obtained from the Hagen-Poiseuille equation (Eq. 3.1). $P_k$ is obtained from the blood flow simulation using the VoM-PhyS model. Figure 3.2 depicts the algorithm in a flow chart.

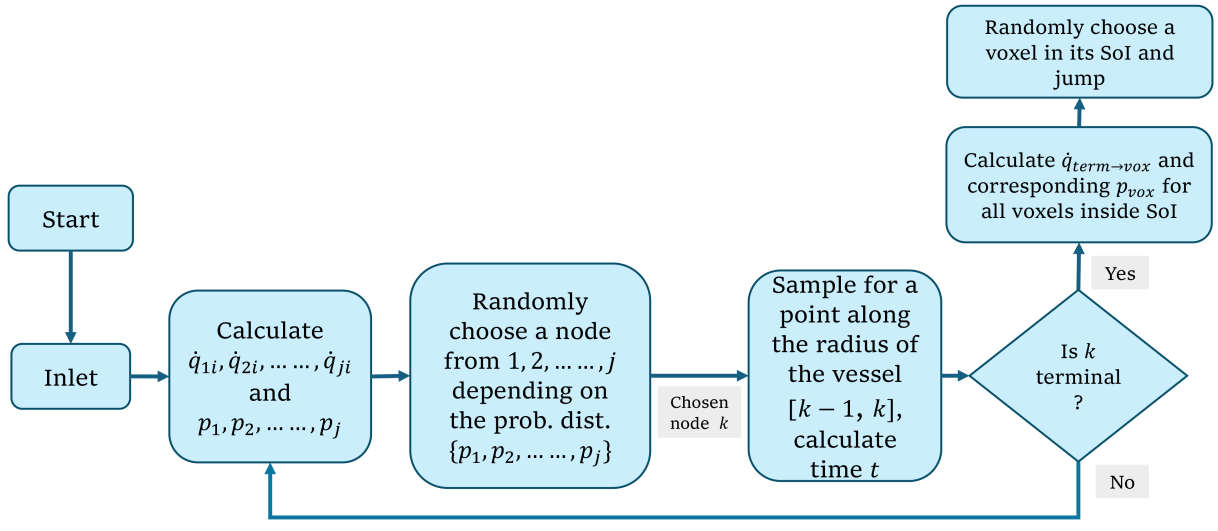


Figure 3.2: Flow-chart of the path tracing algorithm in arterial vasculature.

When the terminal node is reached, the particle jumps to a neighboring voxel located inside the SoI of that terminal node. The probability of a voxel being chosen as the landing voxel is proportional to the flow being delivered to that voxel. For voxel $k$ within the SoI of a terminal arterial node $j$, the probability of being chosen as the landing voxel is also given by Eq. 3.7. The flow a voxel receives from a terminal arterial node or discards to a terminal venous node is dictated by the Dirac function given in Eq. 3.5a.

The time taken at each step of the path is calculated simply by dividing the length of the vessel segment by the speed of the particle in that vessel segment, i.e., $t = L/u$, where $L$ is the length of the vessel segment and $u$ is the velocity of the particle. The velocity of the particle inside the vessel segment depends on the position of the particle along the radial direction. According to the Hagen-Poiseuille theory of laminar flow in a cylindrical pipe of radius $R$, the velocity of a particle at a distance $r$ from the center of the pipe is given by the following equation.

$$u = \frac{\Delta P}{4\mu L}(R^2 - r^2) \tag{3.8}$$

Here, $\Delta P$ is the pressure drop in the vessel segment. The position of the particle is sampled from a uniform distribution of points on the cross-sectional face of the vessel. Essentially, for a vessel of radius $R$, a random number $r$ is chosen from 0 to $R - \delta$ which represents the distance of the particle from the center of the vessel. This particle may be located anywhere on the circle of radius $r$ concentric to the vessel. The parameter $\delta$ represents the average radius of an RBC. This parameter is used to emulate the fact that the center of an RBC located at the outer edge of the cylindrical vessel lies one radius away from the edge. This provision also helps eliminate sampling a number equal to or infinitesimally close to the radius R of the vessel where the velocity of the particles is zero or very close to zero. An example distribution of points sampled on the face of a cylinder is shown in Figure 3.3.

Once a position $r$ for the particle is sampled, the time $t$ elapsed by this particle to cover

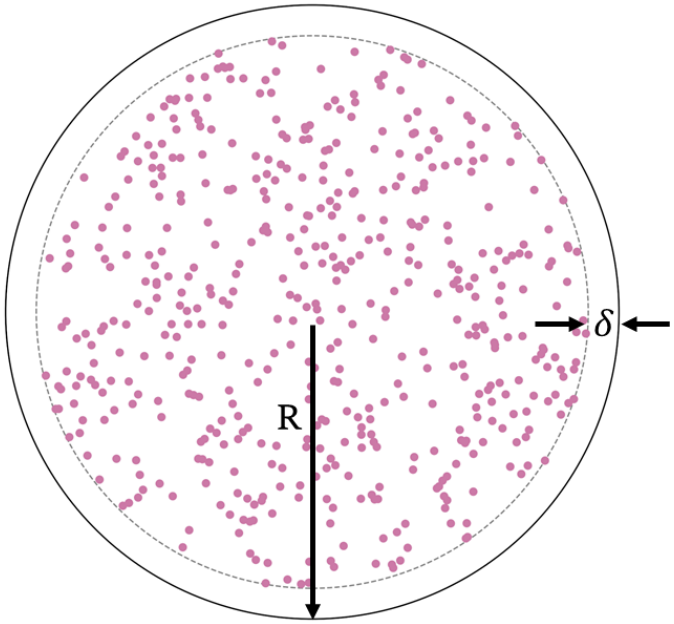


Figure 3.3: Uniform sampling of points on the face of the vessel. Note the distance $\delta$ from the vessel wall, which bounds the extent of position sampling.

the length $L$ of the vessel segment is obtained. The final equation is

$$t = \frac{4\mu L^2}{\Delta P(R^2 - r^2)} \tag{3.9}$$

At this point, it is important to note that the time elapsed by the particle to jump from the terminal arterial node to a neighboring voxel is not negligible. No such jump occurs in a real organ or system inside a living being. Vascular structures exist between these two locations, which implies that there is a finite time for a particle to traverse this distance. This inadequacy of the framework in calculating transit time is addressed later in Section 3.3 and a solution is proposed to calculate the time elapsed in this jump.

### 3.2.2 Path tracing in the arterial compartment

Once the particle reaches a neighboring voxel of a certain arterial terminal, it traces its path in the arterial compartment of the tissue domain. Since the tissue domain is a 3D array of voxels, each voxel in this domain has up to six voxels as its neighbor. Only the voxels that share a face with a given voxel are accepted as its neighbors. The voxels sharing an edge or a corner are not considered as neighbors since the VoM-PhyS model allows the blood to flow only in $x$, $y$ and $z$ directions. Figure 3.4 depicts the neighbors of a typical voxel in the tissue domain. At each step, the next node is chosen from the neighboring six nodes according to a probability distribution. Of the six neighboring nodes, the ones that do not maintain a negative pressure gradient, i.e., at higher pressure with respect to the current node, are filtered out. A probability distribution is then determined for the remaining nodes with the flow rate to these nodes from the current node. The flow rate $\dot{q}$ to a neighboring node $k$ from the current node $j$ inside a porous domain is dictated by Darcy's equation,

$$\dot{q}_{kj} = \frac{K_a A}{\mu} \frac{(P_j - P_k)}{\Delta s} \tag{3.10}$$

where $K_a$ is the permeability of the arterial compartment of tissue domain, $A$ is the cross-sectional area of the voxel perpendicular to the direction of flow, and $\Delta s$ is the distance between the centers of voxels $k$ and $j$. In the VoM-PhyS model, each voxel in the tissue

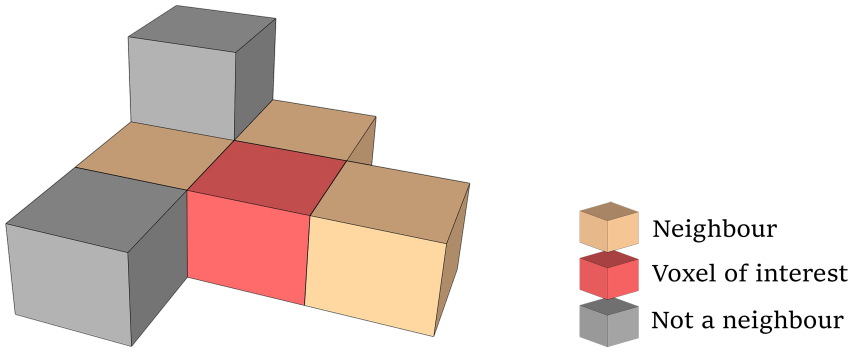


Figure 3.4: neighbors of a voxel of interest (red). Voxels sharing the six faces with the red voxel are counted as neighbors. The grey voxels are not considered as neighbors. All the neighbors are not shown.

domain is assumed to be comprised of two compartments, the arterial compartment and the venous compartment, to accommodate the oxygenated and the deoxygenated state of blood respectively. Hence, transitioning the particle to the venous compartment is allowed in the tissue voxels. The perfusion-driven flow rate is governed by the pressure difference in the arterial and the venous compartment of a given voxel. This flow rate is given by the following equation.

$$\dot{q}_{perf} = \alpha(P_{j,a} - P_{j,v})\Delta V \tag{3.11}$$

Here, $\alpha$ is the perfusion proportionality constant, $P_{j,a}$ and $P_{j,v}$ are the pressures in the arterial compartment and the venous compartment, respectively, and $\Delta V$ is the volume of the voxel.

The probability distribution of possible candidates for the next-step is found by using Eq. 3.7. In this case, $n$ includes all the allowable voxels as well as the venous compartment. The next node is chosen randomly from $n$ subject to the probability distribution. If the venous compartment is chosen, the path tracing transitions to the venous compartment of the tissue domain. The process is depicted in a flow-chart in Figure. 3.5. The time the

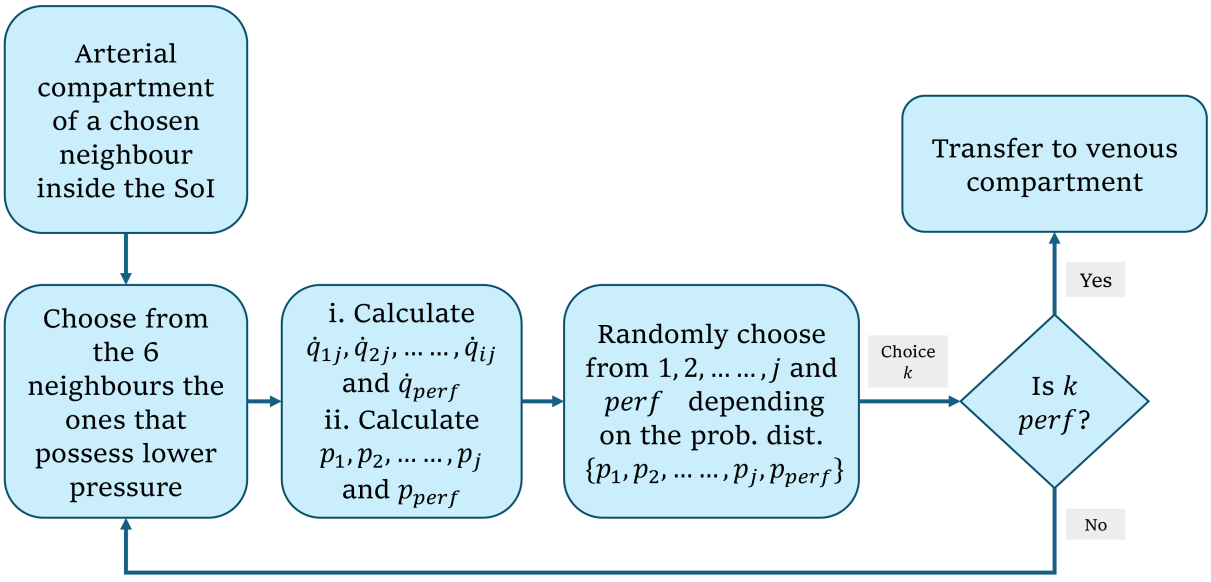


Figure 3.5: Flow-chart of the path tracing algorithm in arterial compartment.

particle takes to go from node $j$ to node $k$ is calculated by $t = \Delta s/u$, where $u$ is the Darcy

velocity of the particle. The Darcy velocity is given by Eq. 3.2, which takes the following discrete form in the arterial compartment.

$$u = \frac{K_a}{\mu} \frac{(P_j - P_k)}{\Delta s} \tag{3.12}$$

The final equation for time is

$$t_{kj} = \frac{\mu(\Delta s)^2}{K_a(P_j - P_k)} \tag{3.13}$$

It is important to note that the transition from the arterial to the venous compartment is assumed to be instantaneous in this work. This is a reasonable assumption due to the fact that the highest pressure drop occurs in this transition, and no distance is traversed by blood in this process inside the tissue domain according to VoM-PhyS model[77]. This transition is a complex process subject to numerous parameters, the treatment of which is beyond the scope of the current study.

### 3.2.3 Path tracing in the venous compartment

Once the particle transitions to the venous compartment, the path tracing continues in the venous compartment of the tissue domain. In the venous compartment, blood can be exchanged not only with the neighboring voxels, but also with the venous terminal nodes as well, if the occupied voxel is inside the SoI of one or more terminals. In such cases, the outflows from the voxel include the neighboring voxels obeying the negative pressure gradient condition as well as the flows to the venous terminals of which the voxel in consideration is within the SoI. The flow to the neighboring voxels is found by

$$\dot{q}_{kj} = \frac{K_v A}{\mu} \frac{(P_j - P_k)}{\Delta s} \tag{3.14}$$

where $K_v$ is the venous compartment permeability. The flow to the respective venous terminals is governed by the Dirac function (Eq. 3.5a). Once all these flows for a certain voxel are

obtained, the probability distribution is calculated using Eq. 3.7. The next node is chosen probabilistically according to this distribution. The time taken by the particle to go from the current voxel $j$ to the chosen next voxel $k$ is given by Eq. 3.13 where $K_a$ is replaced by $K_v$.

$$t_{kj} = \frac{\mu(\Delta s)^2}{K_v(P_j - P_k)} \tag{3.15}$$

Figure 3.6 shows the flowchart of this algorithm in the venous compartment. If the particle chooses a venous terminal, it takes a jump from the voxel to that terminal, similar to Section 3.2.1. One method of calculating the time elapsed in this jump is presented in Section 3.3.

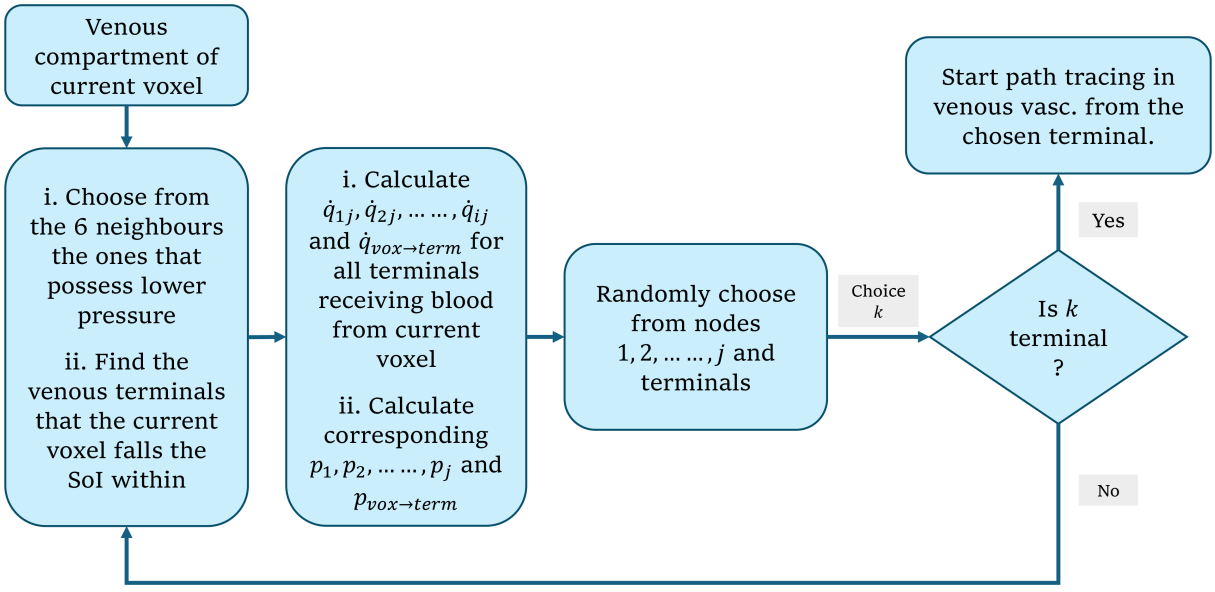


Figure 3.6: Flow-chart of the path tracing algorithm in venous compartment.

### 3.2.4 Path tracing in the venous vasculature

Path tracing in the venous vasculature begins when the particle reaches the venous terminal node. From there, the particle follows the rules described in Section 3.2.1. Flow is calculated using Eq. 3.1, probability distribution using Eq. 3.7, and time using Eq. 3.9. The path tracing

ends when the particle reaches one of the outlet nodes. The algorithm is depicted in the flow chart in Figure 3.7.

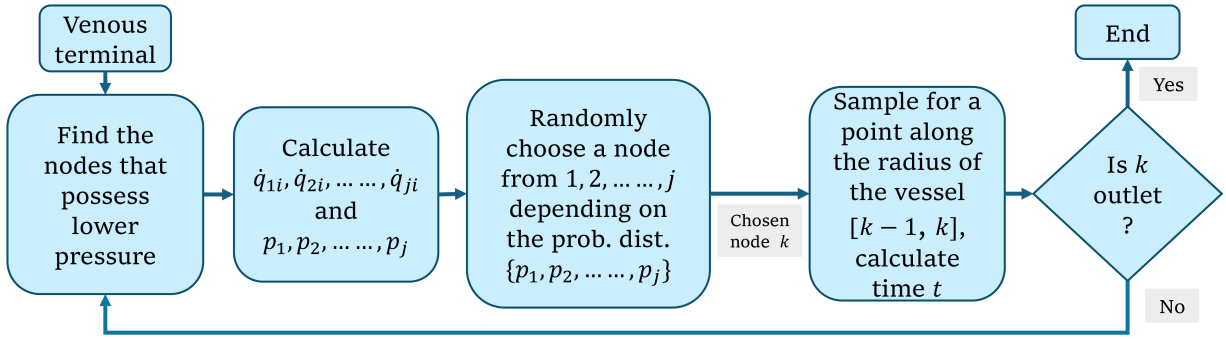


Figure 3.7: Flow-chart of the path tracing algorithm in venous vasculature.

A generic path traced by the algorithm stated above is shown in figure 3.8. The path starts from the inlet, tracing through the arterial vasculature, jumps to the arterial compartment. Then, it walks in the arterial compartment of the tissue domain until transitioning to the venous side, where it walks in the venous compartment, jumps to a venous terminal, traces through the venous vasculature, and eventually finishes at the outlet. Figure 3.8 also shows the discontinuities in the domain, i.e., the vessel endings, and the compartments.

## 3.3 Time In The Unsegmented Vasculature

Transit time in the segmented vasculature is well defined because the physical structure, e.g. length, diameter, and the flow condition, e.g. velocity, pressure, are well-defined. Similarly, in the capillary bed, the structure is well-defined due to the porous media assumption, and consequently, flow and pressure is also well known by the virtue of Darcy's equation (Eq. 3.2). Hence, the transit time in the capillary bed can be calculated with relative ease. In the case of the unsegmented vasculature between the segmented vascular network and the capillary bed, the structure is unknown due to the lack of segmentation data. In Hodneland's work[74], the flow in this region is handled with mathematical modeling (Dirac function (Eq. 3.5a)) that distributes the flow from a terminal instantaneously to the voxels in a predefined region, while the resistance of the missing network of vasculature in this region is modeled using a constant

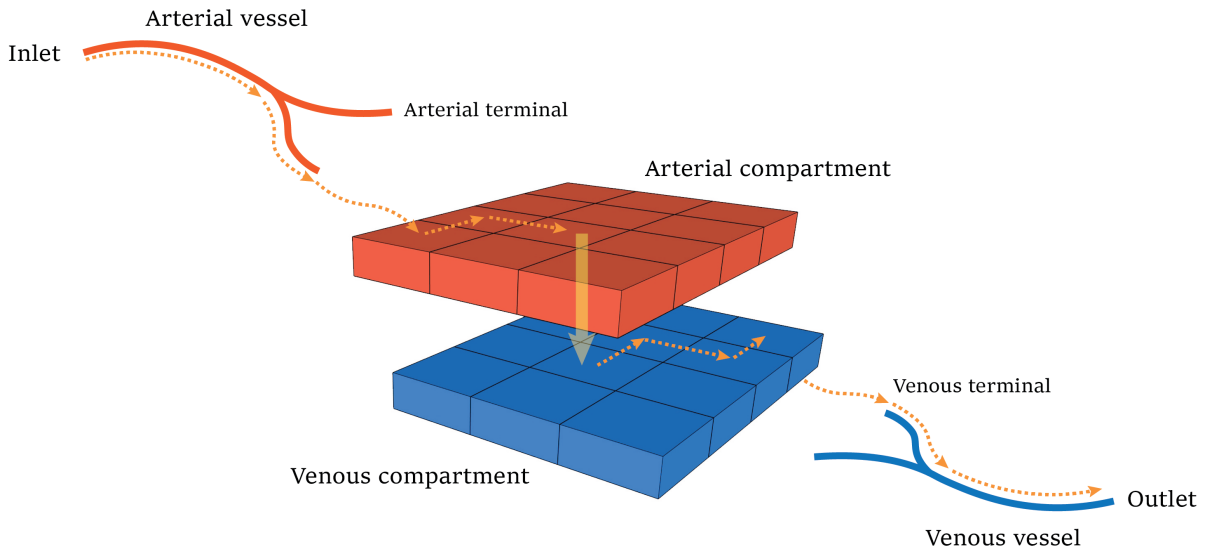


Figure 3.8: A generic path traced by the proposed Path Tracing Framework. The transparent fat arrow depicts the transition from arterial to venous compartment.

parameter ($\gamma_\beta$). Although ensuring flow continuity, the real hemodynamic information, i.e., the path that blood particles follow to reach those voxels, cannot be retrieved. As a result, the time to traverse those paths is also unknown. In this section, a method will be developed to estimate the time that a blood corpuscle (or any particle of interest following the blood flow) would take on average to reach the destination voxels from an arterial terminal (or the destination venous terminal from a voxel).

Before delving into details of the method, it is assumed, due to lack of data, that the terminal and each of the voxels within its SoI are connected via a vessel or a duct of constant circular cross section. These vessels may be bent, skewed or twisted in any desired way to represent the tortuous path that the blood would travel in the missing vasculature as long as these actions do not allow the vessel to intersect any plane taken along the cross-section more than once. According to Cavalieri's principle[79], each vessel has a volume equal to the cylinder of same cross section and length equal to the Cartesian distance of the voxel from the terminal.

This scenario can be described by Hagen-Poiseuille equation (Eq. 3.1), where, the flow rate to voxel $i$ from terminal $j$ , $\dot{q}_{ji}$ is known from the Dirac equation (Eq. 3.5a), the pressures

at the two ends of this cylinder $p_j$ and $p_i$, i.e., the pressure at the terminal and the pressure at the voxel, are known from the pressure solution provided by the VoM-PhyS model, and the length $L_{ji}$ is known from the Cartesian distance formula. Given these values, Eq. 3.1 can be solved for the vessel radius $R_{ij}$, which yields,

$$R_{ij} = \left[\frac{8\mu L_{ji}\dot{q}_{ji}}{\pi(p_j - p_i)}\right]^{\frac{1}{4}} \tag{3.16}$$

Knowing the radius $R_{ij}$, the volume of blood in the arbitrary vessel can be calculated as $\pi R_{ij}^2 L_{ji}$. Since, the volumetric flow rate $\dot{q}_{ji}$ in this path is known, the Central Volume Principle[11] (Eq. 2.1) can be invoked to calculate the mean transit time for a single jump in the unsegmented vasculature.

$$MTT_{\beta,j\leftrightarrow i} = \frac{\pi R_{ij}^2 L_{ji}}{\dot{q}_{ji}} \tag{3.17}$$

Here, $MTT_{\beta,j\leftrightarrow i}$ may represent the MTT for both arterial terminal to voxel and voxel to venous terminal.

This method can be used to fill the gaps of times for jumps in an incomplete path, provided that incomplete paths with jumps between the terminal and the voxel are predetermined from the path tracing framework described in Section 3.2.

## 3.4 The Simulation Domain

To demonstrate the functionality of the proposed framework, the model of a frog tongue has been adopted. This frog tongue is found in a classical biology textbook by Cohnheim[80], which represents a realistic vascular system. Figure 3.9a shows the domain as it appears in the book. The original imaging data of this frog tongue was obtained from Hodneland's[74] work. The data consist of 634 x 515 pixels with pixel dimensions of 0.063 mm x 0.064 mm and a thickness of 1 mm. The domain generated from this data is discontinuous because the source and sink terms generated by the arterial and venous terminals in the domain are

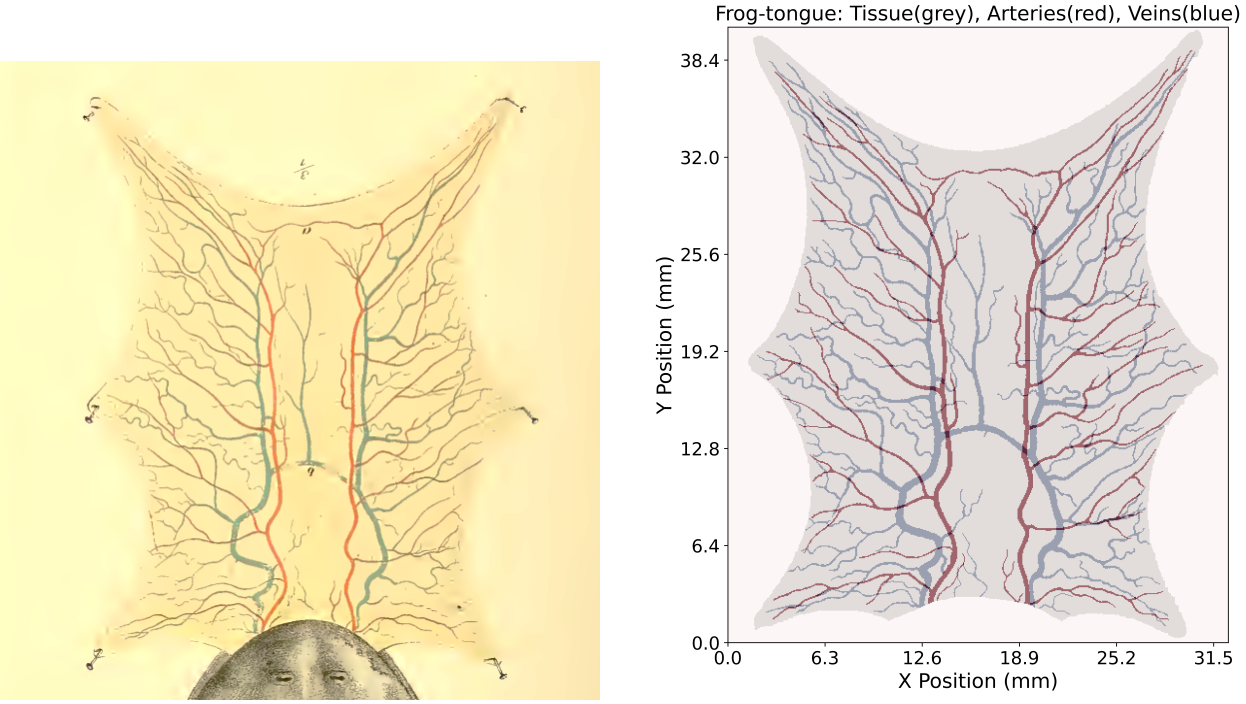


(a) An artist's rendition of the frog tongue in the classical Cohnheim[80] textbook.

(b) Computer rendition of the same frog tongue obtained from literature[74].

Figure 3.9: Computational domain of the frog tongue.

decoupled. This prevents blood perfusion between a tissue-blood interface. To address this problem, Hodneland's[74] work suggested that the blood vessels were completely separated from the domain and the entire system was assumed to be tissue. The 2D frog tongue was converted to a 3D domain by dividing the single slice into three sub-slices of 0.333 mm across the depth. The top layer contains the segmented arterial vessels and surrounding tissues, the middle layer consists only of tissue, and the bottom layer contains the venous vessels and tissues. Figure 3.10 shows the slices. These slices are addressed as Layer 1, Layer 2, and Layer 3, respectively. The little upward triangles in figure 3.10 (a), and downward triangles in figure 3.10 (c) are the arterial inlet and venous outlet nodes, respectively. Dirichlet boundary conditions were imposed at these nodes. The order of these layers is important because it affects the perfusion. In the current setup with arteries on the top, veins in the bottom, and tissue in the middle, blood enters in Layer 1, perfuses through Layer 2, and exits at Layer 3. If the slices were arranged otherwise, the tissue layer would receive less blood through perfusion because the distances of arterial and venous terminals would decrease.

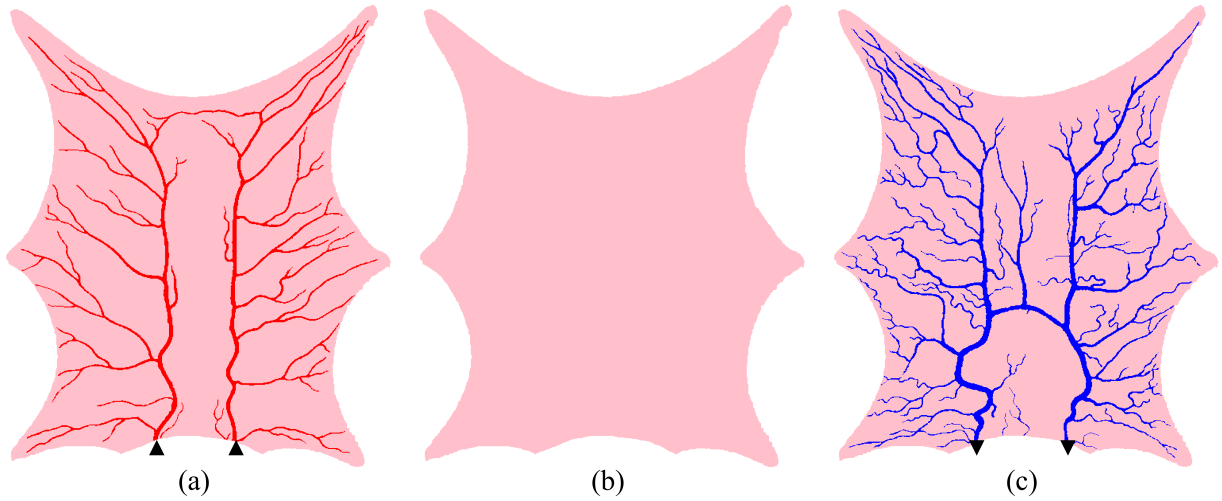


Figure 3.10: The sliced layers of the frog tongue with voxel dimension 0.063 mm x 0.064 mm x 0.333 mm each. The layers represent: (a) Layer 1: Arterial tree and tissue (b) Layer 2: Tissue (c) Layer 3: Venous tree and tissue. Adapted from Amare et al.[77]

A shortcoming of this choice of computational domain is that the vessel structures cannot be validated, since the original sample is not available. Moreover, the geometry is deformed. Figure 3.9a shows that the frog tongue is stretched and pinned on a canvas, which obviously distorted the original dimensions of the structures as they would appear in a living frog. This distortion clearly may have an impact on the blood flow and path tracing. However, this domain was chosen because it shows a representation of biological structures that is more realistic than contemporary algorithm-generated vasculature. It is also simple enough so as to demonstrate the validity of the proposed framework with manageable computational time.

## 3.5 Simulation

To demonstrate the functionality of the path tracing framework, firstly, the pressure map in the frog tongue is required. The pressure map is obtained by utilizing the VoM-PhyS blood flow model, as mentioned in Section 3.1. The pressure map was obtained for four cases of SoI (2 mm, 5 mm, 7 mm and 10 mm). The parameters used for these simulations are given in table 3.1. Once the pressure map was obtained, it was used as an input for the path

tracing framework.

Table 3.1: Simulation Parameters

| Parameter | Symbol | Value | Unit |
|---|---|---|---|
| Perfusion[81] | $\alpha$ | $1 \times 10^{-6}$ | $\mathrm{m\,s\,kg^{-1}}$ |
| Arterial permeability[74] | $K_a$ | $1 \times 10^{-12}$ | $\mathrm{m^2}$ |
| Venous permeability[74] | $K_v$ | $5 \times 10^{-10}$ | $\mathrm{m^2}$ |
| Blood viscosity[74] | $\mu$ | $3 \times 10^{-3}$ | $\mathrm{Pa\,s}$ |
| Pressure drop parameter[74] | $\gamma$ | $1 \times 10^{-14}$ | $\mathrm{m^3}$ |
| Arterial inlet pressure[74] | $P_{in}$ | 10.6 | kPa |
| Venous outlet pressure[74] | $P_{out}$ | 1.6 | kPa |
| Voxel dimensions[74] | | $64 \times 64 \times 333$ | $\mu\mathrm{m}^3$ |
| RBC radius (Offset)[82] | $\delta$ | 3.75 | µm |

For the purpose of calculating MTT, many histories of random paths were generated for all the SoI cases using the proposed path tracing algorithm and total time calculated for each path. Then the arithmetic average is taken to calculate the MTT. The path tracing algorithm described in Section 3.2 was implemented in a Python code which can be found here. The code was run on the Beocat High-Performance Computing (HPC) cluster at Kansas State University.

# Chapter 4

# Results

## 4.1 Flow simulation

Blood flow simulation was carried out in the frog tongue domain using the VoM-PhyS flow solver as described in Chapter 3 with the parameters tabulated in Table 3.1. Figure 4.1 shows the pressure map of the frog tongue domain. Figure 4.1(a) is the pressure map of the arterial compartment of Layer 1 with the arterial vessels and Figure 4.1(b) is the venous compartment of Layer 3 with venous vessels. The pressure maps for all the SoI radii are provided in Appendix A.

In Layer 1, blood pressure is the highest in the inlets, where Dirichlet boundary conditions of 10.6 kPa were imposed. Thenceforth, pressure decreases gradually due to flow resistance from the vascular geometry. In the tissue domain, the highest pressure is seen in the upper left, lower left, and middle right regions where a high density of arterial terminals are visible. Voxels of those regions receive blood from more terminals compared to other regions. Pressure in the tissues gradually decreases towards the bottom right region where only a few number of terminals deliver blood. The lowest pressure of about 9 kPa is found in this region. Blood gradually perfuses through the middle tissue layer, i.e., Layer 2, and undergoes significant drop in pressure. In Layer 3, the highest pressure in the tissue domain is about 1.96 kPa, which indicates that blood incurs a significant pressure drop of about

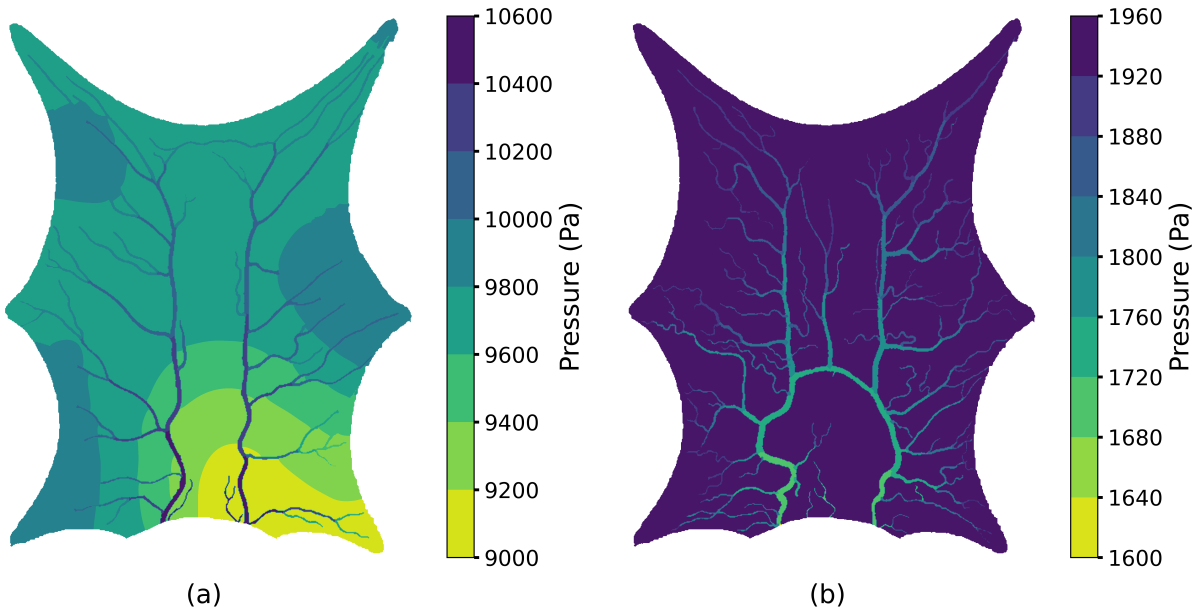


Figure 4.1: Pressure map in the frog tongue for SoI radius $\epsilon = 10$ mm. (a) Arterial compartment of Layer 1. (b) Venous compartment of Layer 3.

8.6 kPa with respect to the inlets. Pressure decreases further in the venous vasculature and finally exits at 1.6 kPa, which is the imposed boundary conditions at the outlets.

## 4.2 Path tracing

Once the pressure map was obtained, histories of random paths were generated for the SoI radii mentioned in section 3.5. Four sets of data with $10^3$, $10^4$, $10^5$, and $10^6$ particle histories were generated for each SoI radius. Particle histories in increasing order of ten were chosen to observe how number of histories affect the transit time distribution and the MTT. Subsequently, the total transit time for each history was calculated for the four sets of particle histories for each SoI radius and a histogram of transit times was generated. The MTT was also calculated from the generated data. These data were then visualized in various plots which will be presented in the subsequent sections.

### 4.2.1 Transit time distribution

Figure 4.2 shows the transit time distribution for all SoI radii, simulated with $10^6$ particle histories. The figure shows the transit times up to 10000 seconds which covers about 99% of the histories. The extreme outliers that span less than about 1% of the histories are not shown in the figures. These outliers were most likely caused by particles traveling too close to the vessel wall or having too large jump time. However, the full range of transit times were used to compute the MTT. The transit times were binned into 100 second bins. The histograms were plotted to display the distribution of transit times. To determine which distribution function describes the plotted data the best, three candidate distributions–gamma (Eq. 2.9), gamma-variate (Eq. 2.10), and lognormal–were selected based on the literature review and general observation of the plotted histogram. Two very well known metrics of curve-fitting–Coefficient of Determination ($R^2$), and Akaike Information Criterion (AIC)[83]–were calculated with the $10^6$ particle histories dataset for all SoI cases. Table 4.1 shows the obtained values of the metrics. The standard comparison rules for the two metrics are distinct: for the $R^2$, values closer to 1 indicate superior model fit, while for the AIC, lower numerical values represent better model performance.

Table 4.1: Values of Curve-fit Metrics

| SoI (mm) | Metrics values | | | | | |
|---|---|---|---|---|---|---|
| | $R^2$ | | | AIC | | |
| | Gamma | Gamma-variate | Lognormal | Gamma | Gamma-variate | Lognormal |
| 2 | 0.9934 | 0.9997 | 0.9786 | -2164.3 | -2484.7 | -2046.8 |
| 5 | 0.9851 | 0.9992 | 0.9928 | -2106.6 | -2392.7 | -2179.6 |
| 7 | 0.9683 | 0.998 | 0.9947 | -2059.3 | -2330.7 | -2237.7 |
| 10 | 0.9556 | 0.9949 | 0.9955 | -2081.7 | -2293.1 | -2311.4 |

From Table 4.1, it is evident that the distributions generally follow a gamma-variate distribution, although the 10 mm SoI case fits the lognormal distribution the best. Figure 4.2 includes a gamma-variate fit for comparison. The MTT calculated from the distributions start at about 757 seconds for $\epsilon = 2$ mm and gradually increases to about 2300 seconds for $\epsilon = 10$ mm. The distribution has higher peak for $\epsilon = 2$ mm, and the peak gradually decreases. The mode of the distributions starts at 300-400 seconds for $\epsilon = 2$ mm and increases to 1000-

1100 seconds for $\epsilon = 10$ mm. At the same time, the distribution also gets flatter and wider as the SoI increases. Transit time distributions for all the cases of SoI radii and number of particle histories are provided in Appendix B.

Table 4.2 shows the average percent contribution in time of the path-segments in $10^6$ particle histories for all SoI cases. Percent contributions of combined arterial and venous vessel time, combined arterial and venous compartment time, and combined arterial-side and venous-side jump-time for each particle history were calculated. An overall average of the percent contributions of each of these three combinations aggregated across all $10^6$ histories is then reported in Table 4.2. It is clear from Table 4.2 that for small SoI radii, the time spent in the tissue domain dominates the total transit time. Blood from arterial terminals is distributed among the voxels in a smaller volume in this case. Therefore, the blood relies heavily on perfusion to reach the venous terminals. This results in smaller transit time, which is evident from Figure 4.2a. As SoI increases, blood is distributed to greater number of voxels since the SoI covers more voxels. Blood from arterial terminal can reach distant arterial voxels and distant venous terminals can collect blood from venous voxels in this case compared to smaller SoI. Hence, dependence on perfusion to reach venous terminal decreases. Variations in flow delivery to voxels also increases, since the Dirac distribution function in this case dictates deliveries to greater number of voxels covering a bigger range of distance. Therefore, the span of jump times also increases. Jump times now accommodate smaller distances with slightly longer time than smaller SoI due to the fact that a voxel at a particular distance receives lesser flow for larger SoI compared to smaller SoI. Distant voxels in larger SoI cases receive even lesser flow, which results in very long jump time. As a combined effect of all these phenomena, the jump time in the unsegmented vasculature starts dominating the total transit time for greater SoI, which is evident from Figure 4.2d.

### 4.2.2 Comparison of MTT

Figure 4.3 shows the MTTs for all the SoI with increasing number of particle histories. For $\epsilon = 2$ mm, MTT is the lowest and it settles around 757 seconds at $10^6$ histories. The increasing

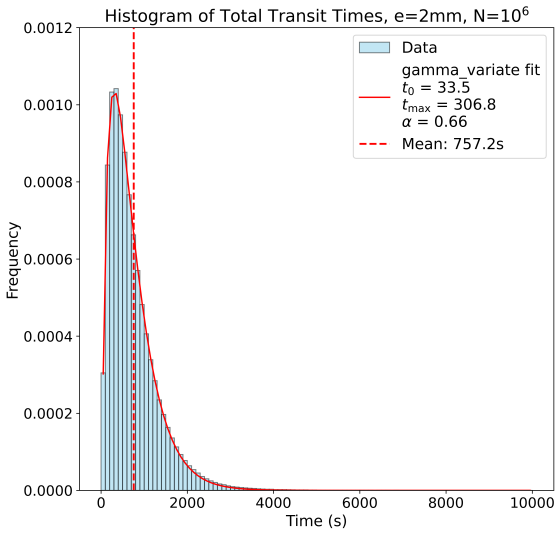


(a) $\epsilon = 2$ mm

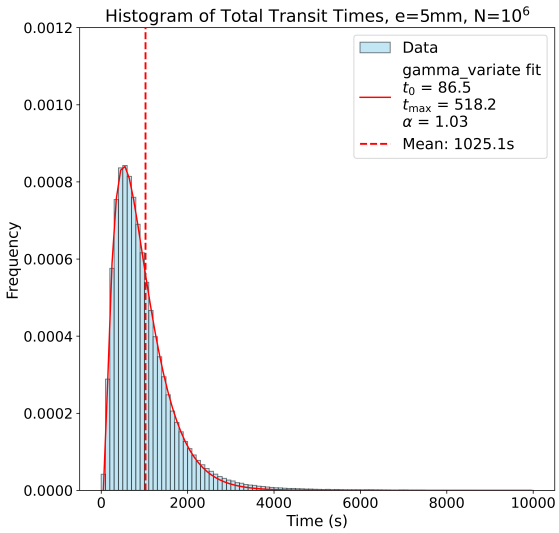


(b) $\epsilon = 5$ mm

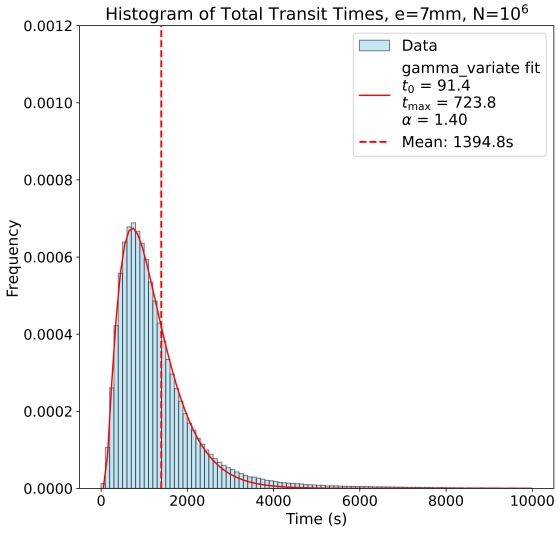


(c) $\epsilon = 7$ mm

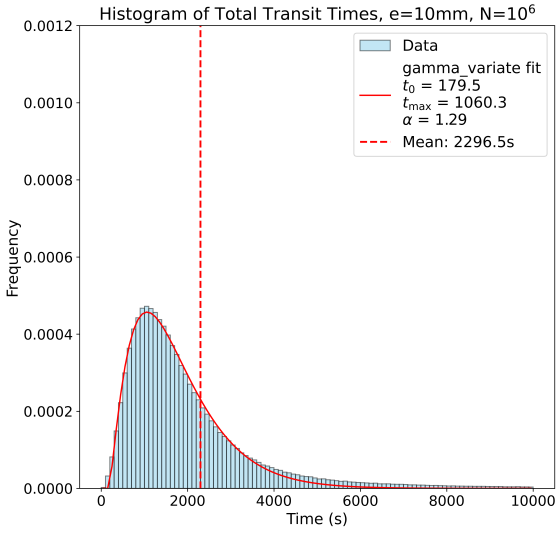


(d) $\epsilon = 10$ mm

Figure 4.2: Transit time distribution for SoI radii $\epsilon = 2$ mm, 5 mm, 7 mm, and 10 mm with $10^6$ particle histories. The mean transit time and the gamma-variate fit with estimated parameter values are also shown.

Table 4.2: Average % Contribution in Transit Time of Path-segments

| SoI (mm) | Average % contribution | | |
|---|---|---|---|
| | Vessels avg. | Tissue avg. | Jump avg. |
| 2 | $\sim 4.8$ | $\sim 86.8$ | $\sim 8.4$ |
| 5 | $\sim 3$ | $\sim 65$ | $\sim 32$ |
| 7 | $\sim 2.3$ | $\sim 52.3$ | $\sim 45.5$ |
| 10 | $\sim 1.5$ | $\sim 37.7$ | $\sim 60.8$ |

trend of MTT with increasing SoI is evident from the figure. For $\epsilon = 10$ mm, MTTs does not seem to converge to a particular value up to $10^6$ histories. To show the convergence, more particle histories, up to $5 \times 10^6$, have been generated. Figure 4.4 shows the data. It shows that for very high particle histories, the MTT for $\epsilon = 10$ mm case tends to converge to approximately 2297 seconds.

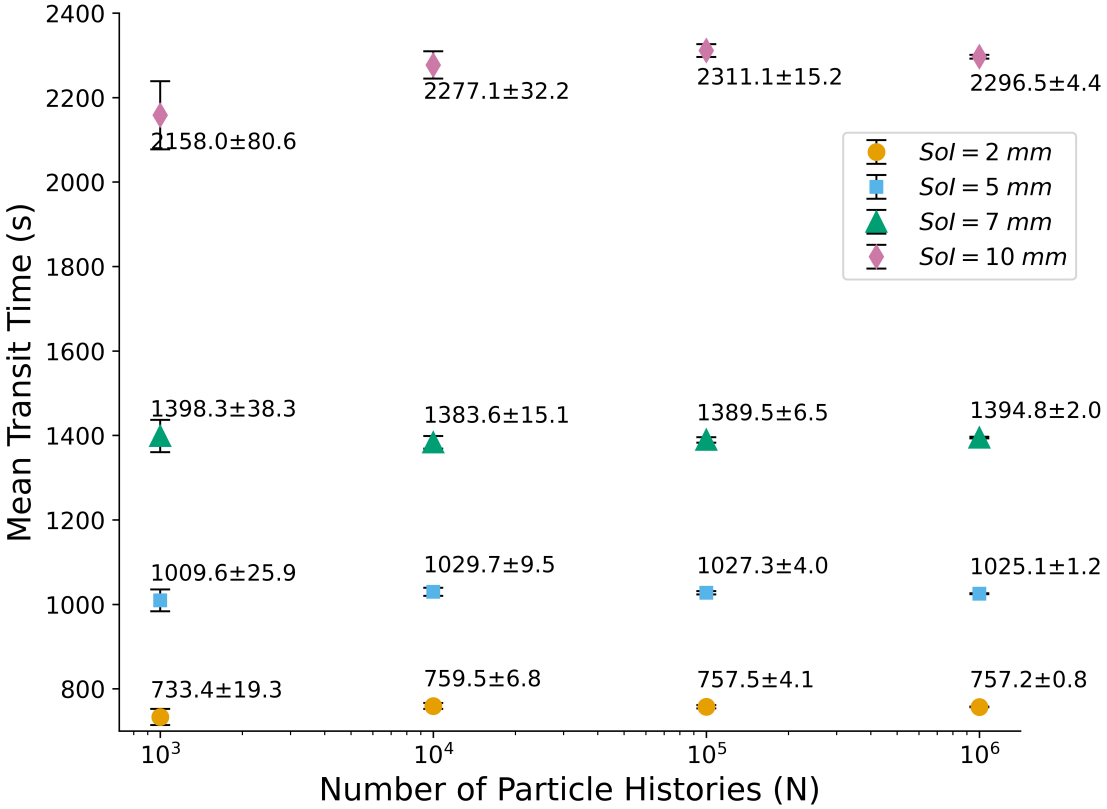


Figure 4.3: MTT with increasing particle histories for different SoI.

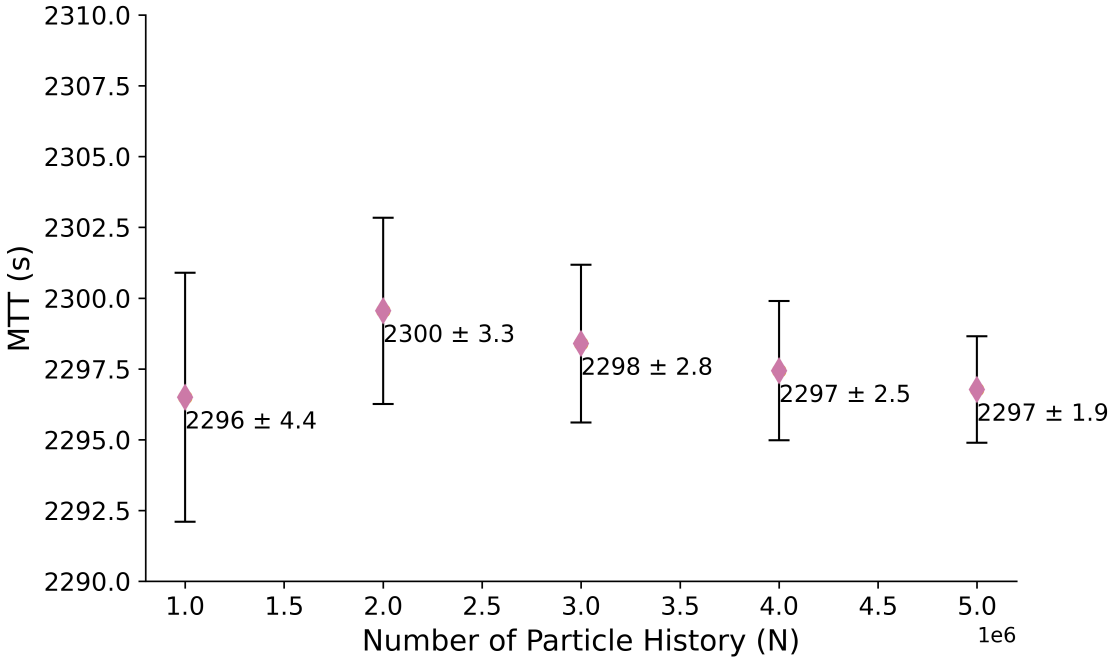


Figure 4.4: Convergence of MTT with high number of histories for $\epsilon$=10 mm.

### 4.2.3 Significance of jump time

Figure 4.5 compares MTT calculations with and without accounting for the travel time between arterial terminals and their corresponding voxels, and venous voxels and their corresponding venous terminals, for $10^6$ particle histories. The trends show that the MTTs tend to decrease if the jump time is not accounted for, whereas they increase in the case where it is accounted for. If the jump time is ignored, the transit time becomes highly dependent on perfusion. As the SoI increases, the particle of interest perfuses through shorter distances in the capillary bed to get collected by the terminal venous vessels. As a result, transit times decrease. On the other hand, more and more voxels receive blood from an arterial terminal, and a venous terminal can receive blood from more voxels as the SoI increases. Consequently, paths of particles traveling through the vasculature become more varied in length. Jump times dominate in a particle's transit time due to smaller flow rates to the voxels for higher SoI cases. Therefore, MTTs increase as SoI increases.

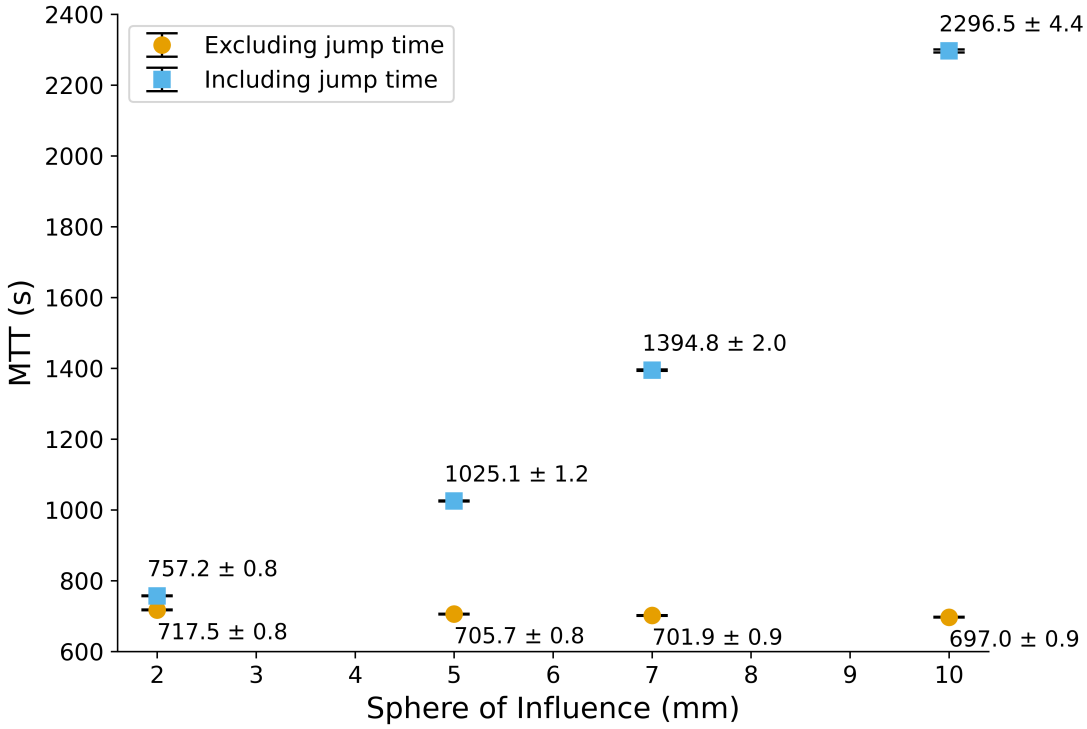


Figure 4.5: Comparison of MTT with and without jump time.

### 4.2.4 Significance of modeling capillary bed

In Correa-Alfonso's[58] and Xing's[9] work, blood vessels are generated using an in house CCO algorithm inside the computational domain. These algorithmically-generated blood vessels cover vessels up to 100 µm in diameter. In reality, blood vessels can have much smaller diameter than that in the capillary bed, as small as 3.5 µm[73]. Moreover, they connect the arterial and venous terminals at the lowest diameter level, which completely disregards the intricate flow phenomena of the capillary bed.

In Hondeland's[74] framework, and VoM-PhyS[77] model, the capillary bed is taken into account. Since the present study relies on these works, the effect of capillary bed on MTT is also studied. Figure 4.6 shows the percentage of histories that has spent more time in the capillary bed than the segmented and unsegmented vasculature (i.e., the jump) combined for all the cases of SoI. For $\epsilon = 2$ mm, about 96% of the particles have spent more time in

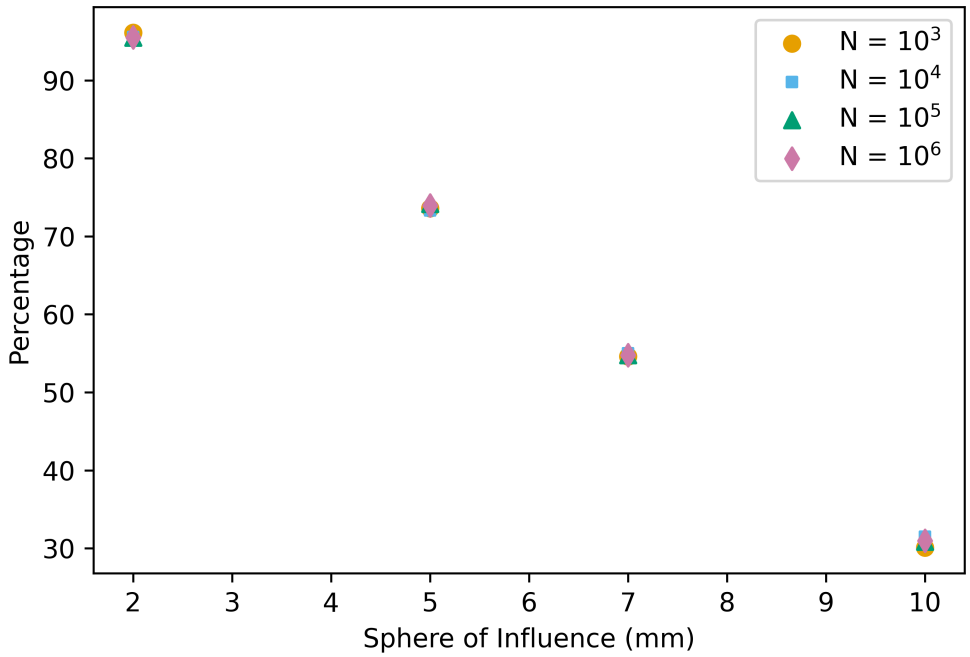


Figure 4.6: Percentage of histories elapsing higher time in capillary bed.

the capillary bed. As SoI increases, the percentage decreases, showing about 75% for $\epsilon = 5$ mm, 56% for $\epsilon = 7$ mm, and 30% for $\epsilon = 10$ mm. For $\epsilon = 10$ mm, more than 90% of the tissue voxels directly exchange blood with the terminals[84]. About 32% of the histories spend more time in the capillary bed compared to segmented and unsegmented vasculature, which is evident from Figure 4.6. This demonstrates the importance of modeling the capillary bed in hemodynamic analysis.

## 4.3 Statistical quality check

The reliability of Monte-Carlo simulations depends critically on rigorous statistical validation. Forster et al.[85] introduced a set of diagnostics designed to evaluate the reliability of Monte-Carlo tallies. These checks address different aspects of statistical convergence, ensuring that results adhere to the assumptions of the Central Limit Theorem (CLT) and that confidence intervals are valid. This diagnostic method comprises of 10 statistical checks for

various statistical parameters, e.g. mean, relative error (RE), variance of variance (VOV), figure of merit (FoM), etc. These tests are briefly explained in the following and the data generated by the proposed framework in the present work will be examined against these standards.

- **Non-monotonic behavior of the estimated mean**

  A monotonically increasing or decreasing mean as the number of histories (N) grows suggests that the simulation has not yet stabilized. This check ensures that the mean oscillates around a converged value rather than drifting systematically, which could indicate unresolved rare events or insufficient sampling. Referring to Figure 4.3, it is evident that the MTTs are non-monotonic for all the cases of SoI. The values do not show general convergence to any particular value, nor they show any upward or downward trend.

- **Magnitude of the Relative Error (RE)**

  The relative error must be below empirical thresholds, i.e., $< 0.05$ for point detector tallies and $< 0.10$ for other tallies. Excessively high RE values signal poor statistical precision, even if the mean appears to be stable. The relative error was calculated using the following formula for large N.

$$RE = \sqrt{\frac{\sum x_i^2}{(\sum x_i)^2} - \frac{1}{N}} \tag{4.1}$$

  Figure 4.7 shows the estimated relative error with increasing particle history. All of the values are less than 0.05, which signifies high statistical precision.

- **Monotonic decrease of the relative error**

  The RE should generally decrease as N increases, following the expected $1/\sqrt{N}$ trend. If the RE plateaus or increases, it suggests that new, high-variance events are still being discovered, violating the CLT assumption of adequate sampling. Figure 4.7 includes a $1/\sqrt{N}$ trendline to clearly show the comparison. The RE of generated data follows the $1/\sqrt{N}$ trend very closely.

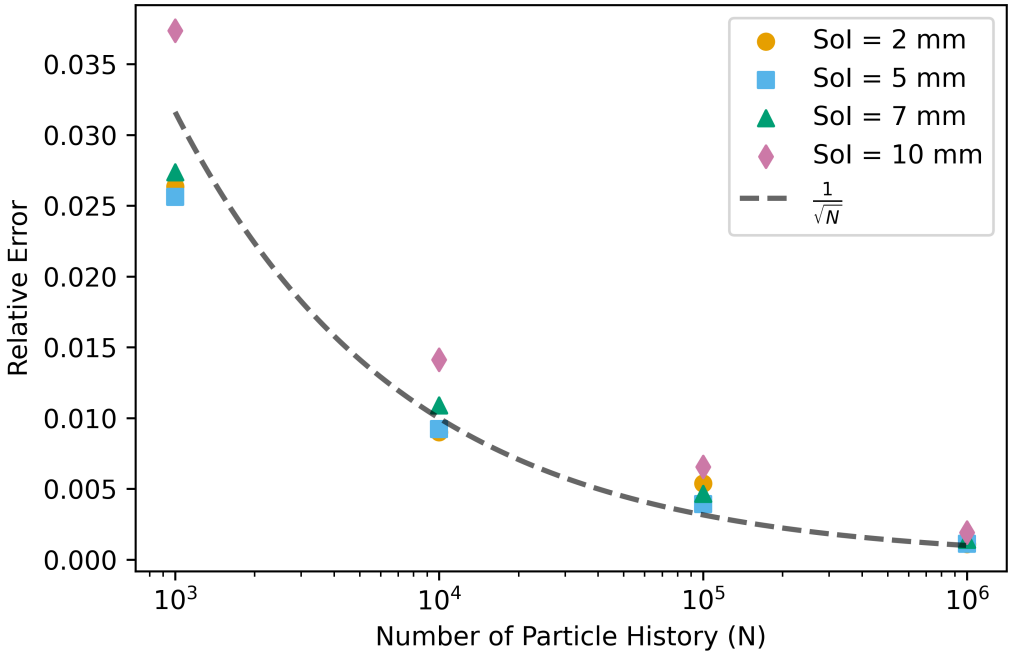


Figure 4.7: Estimated relative error with increasing particle history.

- **Magnitude of the variance of variance(VOV)**

  The VOV measures the uncertainty in the RE estimate itself. A VOV $< 0.10$ is recommended to ensure the RE is statistically reliable. High VOV values, i.e., $> 0.10$ imply that the RE is unstable and confidence intervals are untrustworthy. The VoV was calculated using the following formula for large N.

$$VOV = \frac{\sum(x_i - \bar{x})^4}{(\sum(x_i - \bar{x})^2)^2} - \frac{1}{N} \tag{4.2}$$

  Figure 4.8 shows the variance of variance of the data. All of the data points except one (N = $10^5$ for $\epsilon = 2$ mm) fall below the recommended value of 0.10. The sudden jump of VOV for the N = $10^5$, $\epsilon = 2$ mm case indicates that there might be rare but high-magnitude scores dominating the variance and the underlying distribution may have heavy tails.

- **Monotonic decrease of the VOV**

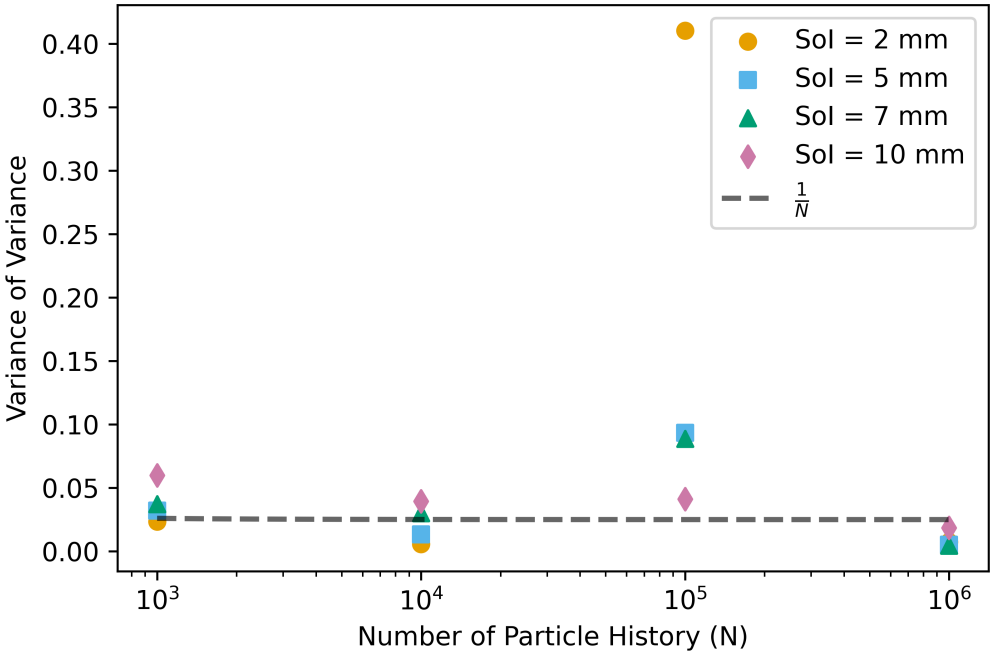


Figure 4.8: Variance of variance of the generated data with increasing particle history.

Like the RE, the VOV should decrease as N grows. Non-monotonic behavior (e.g., sudden jumps) may indicate infinite higher moments (e.g., fourth moment) or unresolved rare events skewing the variance estimation. If the jump at N = $10^5$ is overlooked for a while, Figure 4.8 shows a declining trend. The jump behavior indicating sampling of rare high value data goes away with increase in histories.

- **1/N scaling of the VOV**

  Figure 4.8 also provides a $\sim 1/N$ trendline to compare the values. The data points, except for the jumps, follow the trendline very closely, which signifies overall good quality of sampling and satisfying of CLT.

- **Stability of the figure of merit (FoM)**

  The Figure of Merit (FoM) is a key metric in Monte Carlo simulations that quantifies the computational efficiency and statistical stability of a tally. It is calculated using the following formula.

$$FoM = \frac{1}{\mathrm{RE}^2 \cdot \mathrm{CPU\ \ time}} \tag{4.3}$$

A high FoM means the simulation achieves low uncertainty (high precision) per unit of CPU time, whereas a low FoM suggests inefficiency; either the uncertainty is high, or the runtime is excessive for the precision obtained. In a well-behaved simulation, the FoM should remain statistically constant as the number of particle histories increases. Increasing or decreasing trends in FoM signals unresolved rare events or poor sampling. Figure 4.9 shows the calculated FoM for the generated data. All data were generated using the same computer architecture to ensure comparability.

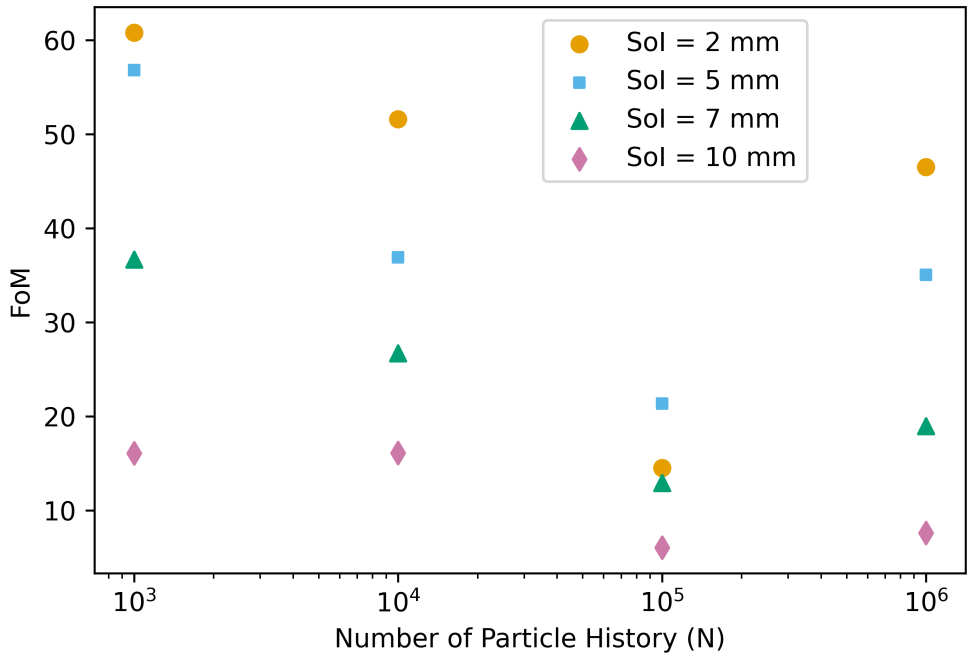


Figure 4.9: Figure of Merit of the generated data with increasing particle history.

In the case of $\epsilon = 10$ mm, the FoM values are not dramatically fluctuating, which can be interpreted as statistically constant. All the other cases show high downward jumps as well as decreasing trends. This might result from undersampling or improper

sampling which may be resolved by simulating more particles.

- **Non-monotonic behavior of the FoM**

  The FoM should exhibit random fluctuations rather than monotonic trends. A strictly rising or falling FoM suggests bias. Referring to Figure 4.9, overlooking the sudden dip for the N = $10^5$ data set, SoI cases $\epsilon$ = 2 mm, 5 mm, and 7 mm show a general decreasing trend in FoM. More histories need to be simulated for these cases to ascertain convergence. For $\epsilon$ = 10 mm, the plot shows random fluctuations, which indicates good quality. This case is promising, albeit further tests are required to verify strong reliability.

- **Tail Slope of the Empirical Score Distribution**

  The largest history scores are fitted to a Pareto distribution to estimate the tail decay rate. The slope is calculated using the following formula,

$$\text{slope} = 1 + \frac{1}{k} \tag{4.4}$$

  where, $k$ is a parameter of the Pareto distribution. A slope $> 3$ ensures the variance is finite, while slopes $\leq 3$ violate CLT assumptions. This check is critical for detecting unsampled high-score regions. Figure 4.10 shows the empirical history scores, i.e., the slope of the tail of the generated distributions.

  This plot clearly addresses all the suspicions of the previous tests. For N = $10^5$, the VOV values took a sudden jump, signifying poor sampling. From Figure 4.10 it is clear that the slope is equal to 3 for all the SoI cases, which clearly means that the tail of the distributions are not decaying quick enough. This is a clear indication of undersampling of high value region. Hence, N = $10^5$ is definitely not enough samples to cover the whole distribution perfectly. Additionally, $\epsilon$ = 2 mm has slope $\leq 3$ even for N = $10^6$ histories, which indicates that this case will take substantially high number of particle histories to converge. The other SoI cases show good result for N = $10^6$ in this test as well as all the previous tests, which means $10^6$ is a reasonable number of

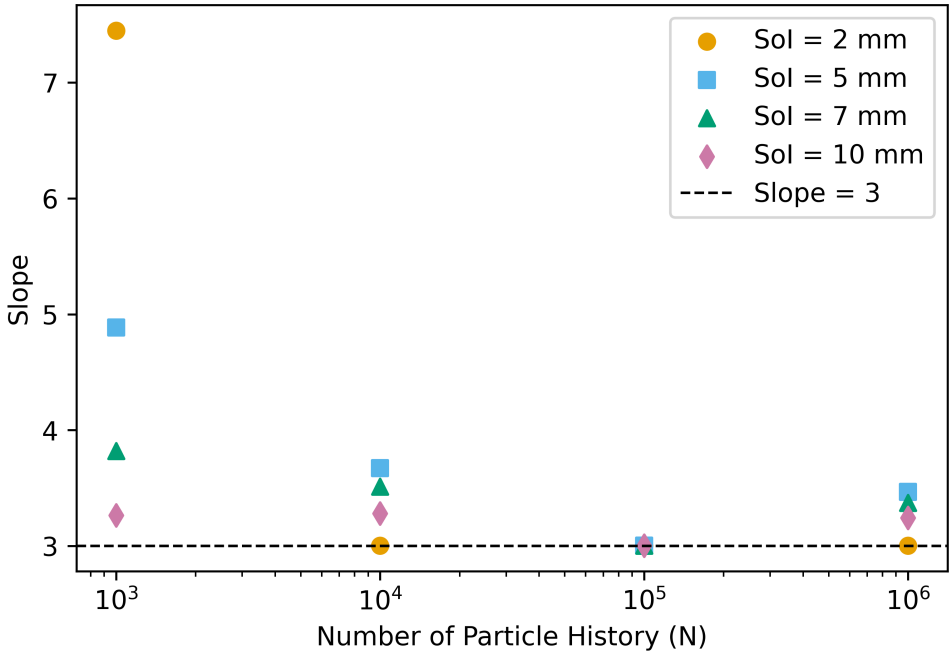


Figure 4.10: Empirical history score of the generated data with increasing particle history.

particle histories for declaring convergence. Although, simulating additional histories is commonly suggested to maintain accuracy.

## 4.4 Discussion

Section 4.2.1 illustrates the transit time distributions of the particles in the frog-tongue computational domain for the specified sphere of influence radii. Comparison of the mean transit time is provided in Section 4.2.2. The increasing trend of MTT with increasing SoI noticeable from Figure 4.3 conform to the rationale given in Section 4.2.1. However, the values of MTT are higher than expected. The minimum time a particle would've taken to traverse a path, traveling at the centerline velocity of each segment, perfusing instantaneously through the tissue domain, is approximately $\sim$ 1.5 seconds. A sample calculation for $\epsilon =$ 10 mm is shown in Appendix C. No account of any actual experimentally measured transit time in a frog-tongue was found in the literature. To draw a comparison, MTT in a Sprague-

Dawley rat lung is about 4 seconds[29]. It is reasonable to assume that the MTT in the frog-tongue of a living frog would approximately be of the same order. Hence, the discrepancy is substantial. The primary reason behind this discrepancy would be the physical structure of the frog-tongue domain. In Figure 3.9, it is clearly noticeable that the frog-tongue has been stretched due to the affixation to the board. As a result, the salient features, such as, the dimensions of the vasculatures have been distorted.

Another reason for this discrepancy might arise from the assumption of single vessels, having constant cross sections, connecting the terminals of segmented vasculatures to the neighboring voxels, in Section 3.3. In reality, there are many levels of bifurcating arterioles of diminishing diameters beyond the segmented vasculatures. Hence, the cross sectional area in each branching vessel decreases and the flow resistance increases. This implies that velocity is higher in the wider vessels and diminishes as the vessels become narrower. The assumption of constant cross section throughout, without branching, may lead to overestimation of jump-time for the distant voxels, since the blood is flowing at a constant velocity throughout, rather than higher velocity in the earlier vessels and gradually decreasing in the latter. The intricate structures of smaller arterioles might violate the assumption of Cavalieri's principle as well, which states that the vessels never bend in a way so as to intersect a plane along its cross section more than once. In their smallest levels, the arterioles may take a very long and winding path, leading to the violation of equal volume of straight and bent vessels between vascular terminals and their delivery voxels.

Moreover, the frog-tongue do not represent an actual living condition in terms of the parameters used. The flexibility of the proposed framework is that the parameters listed in Table 3.1 can be tuned to represent a real simulation domain as soon as the domain and its associated parameter values are available. For optimal statistical reliability in this framework, increasing the number of simulated particle histories is strongly recommended. From the statistical tests of Section 4.3, it can be inferred that a reliable result can be obtained if the simulated number of histories is at least $10^6$ at a SoI of 10 mm, since this case successfully passes all the diagnostic criteria for convergence.

# Chapter 5

# Summary and Conclusion

Capillary flow in living bodies is a highly complex phenomenon, and the study of capillary transit time in realistic biological domains is a challenging endeavor. To capture every aspect of it, one needs to understand and model not only the intricate structure of the vascular network in a realistic domain, but also flow phenomena and particle transport. This thesis has attempted to solve this problem by developing and demonstrating a new particle tracking method with the help of voxel phantom and the Voxelized Multi-Physics Simulation (VoM-PhyS) Framework where the particle tracking is performed by utilizing the idea of Monte-Carlo method.

Chapter 2 provides a literature review of various experimental and mathematical methods that have been developed so far to calculate the MTT. It also provides a review of the Monte-Carlo method and the existing Monte-Carlo codes and their various modalities. To estimate the MTT of particles inside a biological organ of interest on a computer rendered computational domain, one must have the information about the flow field inside that domain. Chapter 2 also provides various attempts that has been taken to simulate the flow inside voxelized domains and how they try to overcome the difficulty of coupling the flow physics of 1D-vessel to 3D-porous media. This chapter also provides a brief account of the attempts taken to combine blood flow and particle tracing to facilitate dosimetric calculations. A close look on the aforementioned scientific literature revealed that the current

state-of-the-art of hemodynamic and dosimetric studies fell short in the case of blood flow-driven particle tracking, which would revolutionize not only the calculation of MTT, but also pharmaceutical testing, internal and external radiation therapy in a patient-specific condition. Hence, this study made an effort to develop a blood-flow driven Monte-Carlo based path tracing framework to extend the boundary of human knowledge.

Chapter 3 briefly describes the VoM-PhyS Framework because it is at the heart of this study. The resulting pressure map from the VoM-PhyS Framework was used to calculate the flow at different nodes, and subsequently, the probability distribution of the candidate nodes for the next step. The path tracing framework was divided into four segments to delineate the voyage of the particle of interest in arterial vessel, arterial compartment, venous compartment and venous vessel. The time at each step inside these regions was calculated using the velocity provided by the mathematical models that govern the flow of each respective region. Chapter 3 also provides a method to estimate the time to cover the jump of the particle where the computational domain becomes discontinuous, i.e., where segmented 1D-vessels meet the 3D-porous medium of capillary bed. After running python scripts that implemented this framework, a number of histograms of particle transit times inside voxelized frog-tongue was obtained. Chapter 4 presents the results obtained from the simulation. It was found that the transit times of particles followed a gamma-variate distribution. The mean transit times increased with increasing SoI. The significance of accounting for jump time and modeling capillary bed was also demonstrated. The values of MTT obtained was higher than expected. However, parameters like arterial and venous permeability, pressure drop parameter, inlet and outlet pressures, etc., can be tuned to represent an actual simulation domain to obtain more realistic results, as soon as these values are available.

The proposed framework, despite being able to successfully trace path inside the desired computational domain, suffers from a few limitations. The limitations are addressed below, with some recommendations on how to resolve them.

- The framework assumes Newtonian behavior of blood, which is not the case in reality. Blood is a shear thinning fluid, which can be incorporated in the flow simulation by

using viscosity models such as the Casson model[86].

- The vasculatures are assumed rigid and pulsatile behavior is ignored. Elastic vasculatures may be incorporated in the light of Huang's[31] work stated in the literature review. Variable flux of blood may be set up at inlets.

- The ideal mixing junction assumption is not completely realistic. Biases of particles' at bifurcations to choose the nearest branch may be estimated considering the particle's position with respect to the centreline of the bifurcating branches, and incorporated with the flow-driven branch-choosing probability distribution described in the present work to obtain a more refined probability distribution.

- To address the instantaneous transition from arterial to venous compartment, oxygen exchange models may be introduced.

- The result of this study suffers a great deal from the distortion of the computational domain, which shoots the mean transit time very high. Resorting to a more anatomically accurate domain will resolve the issue. Applying this framework to ICRP[59] liver or tumor models may be the next step to test this framework further.

- The parameter values lack resemblance to an ideal living condition. This is another reason for the high discrepancy of the result. The framework has the flexibility to tune these parameters to achieve realistic in vivo conditions. The use of ICRP[59] liver may provide realistic data for better simulation.

- The assumption regarding Cavalieri's principle in jump-time estimation in the unsegmented vasculature before the capillary bed might not hold in reality. To get rid of this assumption, finer blood vessels may be captured from imaging data, or a few more levels of blood vessels may be generated algorithmically using the CCO algorithm.

The key contributions of the current study to the realm of scientific endeavors are the flow-driven path tracing framework and the method of estimating jump time of the particle at the vascular discontinuity. This research has a multidisciplinary scope of applicability. It

has the potential to be used in drug testing, particulate sedimentation inside human body or specific organs, internal and external radiotherapy and many other avenues. These areas are not studied in this dissertation, but the possibilities may be suggested for future exploration. Some recommendations for improving and advancing this framework are as follows.

- This framework can be used in neurology to correlate prolonged MTT with capillary transit time heterogeneity to identify risk of infarction. it may also be used to simulate amyloid-$\beta$ clearance inefficiencies in Alzheimer's disease, linking MTT variations to early biomarker detection of the disease.

- In immunology , it can be used to model Model T-cell migration to tumors to optimize adaptive cell therapy. It can also be used to study leukocyte dynamics in inflammation or infection.

- In drug testing and particulate sedimentation studies, Pharmacokinetic models may be implemented in conjunction with the particle tracing algorithm to estimate bioavailability, organ-specific retention, clearance, half-life, etc. parameters.

- The simplifying assumption of no nuclear interaction may be removed to facilitate the calculation of dose imparted by radiophermaceuticals. Detailed inhomogeneous activity distribution can be obtained by combining this framework with a deposition model. Then it can be used to calculate effective dose equivalent or committed effective dose equivalent in conjunction with MIRD schema[64]. It can be extended to calculate detailed organ specific dose volume histogram to facilitate dose optimization.

- This framework can be used to calculate the dose on white blood cells and oxygen carrying red blood cells passing through a well-defined window of irradiation in the case external radiotherapy. Tracking white blood cell distribution in tumor can be linked to the efficacy of radiation induced tissue damage. Tracking red blood cells may be linked to oxygen replenishment rate in FLASH[87] irradiated tissues to quantify the normal tissue sparing effect.

- In plant physiology, the framework can be adapted to model sap flow in xylem/phloem networks, linking root-to-leaf transit times to drought stress responses.

With all these potential pathways ahead, a new researcher taking on the task of advancing this framework may focus on a few key channels. Firstly, the ideal mixing chamber assumption should be addressed. Secondly, the Cavalieri's principle assumption should be replaced with a more realistic detailed vasculature. Additionally, elastic properties of vasculature may be introduced. With these three key limitations addressed, one might look further on extending the framework's functionalities, or applying the framework to new innovative tasks. A nuclear engineer's, or a dosimetrist's focus would be to extend this framework's capability to predict heterogeneous radionuclide distribution in a source organ and calculate dose to a target organ. In external radiotherapy, one may focus on dose calculation to white and red blood cells and their subsequent distribution in tumors or cancer cells to facilitate FLASH radiotherapy. Thus, this versatile framework will enable both practical implementation in sophisticated applications and fundamental contributions to expanding human knowledge.

# Bibliography


[1] E. Marieb and K. Hoehn. *Human Anatomy & Physiology*, volume 11th Ed. Pearson Deutschland GmbH, 2018.

[2] Roland N Pittman. Regulation of tissue oxygenation. 2016.

[3] J Rodney Levick. *An introduction to cardiovascular physiology*. Butterworth-Heinemann, 2013.

[4] John E Hall and Michael E Hall. *Guyton and Hall Textbook of Medical Physiology E-Book: Guyton and Hall Textbook of Medical Physiology E-Book*. Elsevier Health Sciences, 2020.

[5] Gary F Mitchell. Effects of central arterial aging on the structure and function of the peripheral vasculature: implications for end-organ damage. *Journal of applied physiology*, 105(5):1652–1660, 2008.

[6] Rakesh K Jain. Normalizing tumor microenvironment to treat cancer: bench to bedside to biomarkers. *Journal of Clinical Oncology*, 31(17):2205–2218, 2013.

[7] Eric J Hall, Amato J Giaccia, et al. Radiobiology for the radiologist. *Int J Radiat Oncol Biol Phys*, 66(627):10–1016, 2006.

[8] J. K. Shultis and R. E. Faw. *Radiation Shielding*, volume 2nd Ed. La Grange park, Illinois: American Nuclear Society, Inc., 2000.

[9] Shu Xing, Jungwook Shin, Jennifer Pursley, Camilo M Correa-Alfonso, Nicolas Depauw, Sean Domal, Julia Withrow, Wesley Bolch, Clemens Grassberger, and Harald Paganetti. A dynamic blood flow model to compute absorbed dose to circulating blood

and lymphocytes in liver external beam radiotherapy. *Physics in Medicine & Biology*, 67(4):045010, 2022.

[10] August Krogh. The supply of oxygen to the tissues and the regulation of the capillary circulation. *The Journal of physiology*, 52(6):457, 1919.

[11] Robert M Weisskoff, David Chesler, Jerrold L Boxerman, and Bruce R Rosen. Pitfalls in mr measurement of tissue blood flow with intravascular tracers: which mean transit time? *Magnetic resonance in medicine*, 29(4):553–558, 1993.

[12] Leif Østergaard. Principles of cerebral perfusion imaging by bolus tracking. *Journal of Magnetic Resonance Imaging: An official journal of the international society for magnetic resonance in medicine*, 22(6):710–717, 2005.

[13] Leif Østergaard, Alma Gregory Sorensen, Kenneth K Kwong, Robert M Weisskoff, Carsten Gyldensted, and Bruce R Rosen. High resolution measurement of cerebral blood flow using intravascular tracer bolus passages. part ii: Experimental comparison and preliminary results. *Magnetic resonance in medicine*, 36(5):726–736, 1996.

[14] Angelo Sassaroli, Jana Kainerstorfer, and Sergio Fantini. Study of capillary transit time distribution in coherent hemodynamics spectroscopy. *Journal of Innovative Optical Health Sciences*, 8(02):1550025, 2015.

[15] Raymond H Thomlinson and Louis H Gray. The histological structure of some human lung cancers and the possible implications for radiotherapy. *British journal of cancer*, 9(4):539, 1955.

[16] Michael R Horsman, Lise Saksø Mortensen, Jørgen B Petersen, Morten Busk, and Jens Overgaard. Imaging hypoxia to improve radiotherapy outcome. *Nature reviews Clinical oncology*, 9(12):674–687, 2012.

[17] Sune N Jespersen and Leif Østergaard. The roles of cerebral blood flow, capillary transit time heterogeneity, and oxygen tension in brain oxygenation and metabolism. *Journal of cerebral blood flow & metabolism*, 32(2):264–277, 2012.

[18] Leif Østergaard. Blood flow, capillary transit times, and tissue oxygenation: the centennial of capillary recruitment. *Journal of Applied Physiology*, 2020.

[19] Jeffrey J Iliff, Hedok Lee, Mei Yu, Tian Feng, Jean Logan, Maiken Nedergaard, Helene Benveniste, et al. Brain-wide pathway for waste clearance captured by contrast-enhanced mri. *The Journal of clinical investigation*, 123(3):1299–1309, 2013.

[20] Thorbjørn S Engedal, Niels Hjort, Kristina D Hougaard, Claus Z Simonsen, Grethe Andersen, Irene Klærke Mikkelsen, Jens K Boldsen, Simon F Eskildsen, Mikkel B Hansen, Hugo Angleys, et al. Transit time homogenization in ischemic stroke–a novel biomarker of penumbral microvascular failure? *Journal of Cerebral Blood Flow & Metabolism*, 38 (11):2006–2020, 2018.

[21] Simon F Eskildsen, Louise Gyldensted, Kartheeban Nagenthiraja, Rune B Nielsen, Mikkel Bo Hansen, Rikke B Dalby, Jesper Frandsen, Anders Rodell, Carsten Gyldensted, Sune N Jespersen, et al. Increased cortical capillary transit time heterogeneity in alzheimer's disease: a dsc-mri perfusion study. *Neurobiology of aging*, 50:107–118, 2017.

[22] Leonard Weiss and Dimeter S Dimitrov. A fluid mechanical analysis of the velocity, adhesion, and destruction of cancer cells in capillaries during metastasis. *Cell Biophysics*, 6(1):9–22, 1984.

[23] JA JACQUEZ. Mathematical models of chemotherapy. In *Proceedings of the Berkeley Symposium on Mathematical Statistics and Probability*, number 4, page 57. University of California Press, 1961.

[24] Edward Taylor, Richard P Hill, and Daniel Létourneau. Modeling the impact of spatial oxygen heterogeneity on radiolytic oxygen depletion during flash radiotherapy. *Physics in Medicine & Biology*, 67(11):115017, 2022.

[25] Kim Mouridsen, Mikkel Bo Hansen, Leif Østergaard, and Sune Nørhøj Jespersen. Reliable estimation of capillary transit time distributions using dsc-mri. *Journal of Cerebral Blood Flow & Metabolism*, 34(9):1511–1521, 2014.

[26] Henrik BW Larsson, Mark B Vestergaard, Ulrich Lindberg, Helle K Iversen, and Stig P Cramer. Brain capillary transit time heterogeneity in healthy volunteers measured by dynamic contrast-enhanced t1-weighted perfusion mri. *Journal of Magnetic Resonance Imaging*, 45(6):1809–1820, 2017.

[27] Sergio Fantini. Dynamic model for the tissue concentration and oxygen saturation of hemoglobin in relation to blood volume, flow velocity, and oxygen consumption: Implications for functional neuroimaging and coherent hemodynamics spectroscopy (chs). *Neuroimage*, 85:202–221, 2014.

[28] Bruce Klitzman and Paul C Johnson. Capillary network geometry and red cell distribution in hamster cremaster muscle. *American Journal of Physiology-Heart and Circulatory Physiology*, 242(2):H211–H219, 1982.

[29] Robert G Presson Jr, Thomas M Todoran, Bracken J De Witt, Ivan F McMurtry, and Wiltz W Wagner Jr. Capillary recruitment and transit time in the rat lung. *Journal of Applied Physiology*, 83(2):543–549, 1997.

[30] Nathaniel J Karst and John B Geddes. Modeling transit time distributions in microvascular networks. *Journal of Theoretical Biology*, 572:111584, 2023.

[31] Wei Huang, Jun Shi, and RT Yen. Stochastic simulation of human pulmonary blood flow and transit time frequency distribution based on anatomic and elasticity data. *Molecular & Cellular Biomechanics*, 9(4):269, 2012.

[32] Stephen J Payne, Yidan Xue, Jen-Feng Kuo, and Wahbi K El-Bouri. Transit time mean and variance are markers of vascular network structure, wall shear stress distribution and oxygen extraction fraction. *Biomechanics and modeling in mechanobiology*, pages 1–13, 2025.

[33] Florian Goirand, Tanguy Le Borgne, and Sylvie Lorthois. Network-driven anomalous transport is a fundamental component of brain microvascular dysfunction. *Nature communications*, 12(1):7295, 2021.

[34] Pedro Andreo. Monte carlo simulations in radiotherapy dosimetry. *Radiation Oncology*, 13:1–15, 2018.

[35] Judith F Briesmeister et al. Mcnptm-a general monte carlo n-particle transport code. *Version 4C, LA-13709-M, Los Alamos National Laboratory*, 2, 2000.

[36] Koji Niita, Tatsuhiko Sato, Hiroshi Iwase, Hiroyuki Nose, Hiroshi Nakashima, and Lembit Sihver. Phits—a particle and heavy ion transport code system. *Radiation measurements*, 41(9-10):1080–1090, 2006.

[37] Iwan Kawrakow. Accurate condensed history monte carlo simulation of electron transport. i. egsnrc, the new egs4 version. *Medical physics*, 27(3):485–498, 2000.

[38] Data Bank. Penelope-2014: A code system for monte carlo simulation of electron and photon transport. 2015.

[39] Sea Agostinelli, John Allison, K al Amako, John Apostolakis, Henrique Araujo, Pedro Arce, Makoto Asai, D Axen, Swagato Banerjee, GJNI Barrand, et al. Geant4—a simulation toolkit. *Nuclear instruments and methods in physics research section A: Accelerators, Spectrometers, Detectors and Associated Equipment*, 506(3):250–303, 2003.

[40] Giuseppe Battistoni, Till Boehlen, Francesco Cerutti, Pik Wai Chin, Luigi Salvatore Esposito, Alberto Fasso, Alfredo Ferrari, Anton Lechner, Anton Empl, Andrea Mairani, et al. Overview of the fluka code. *Annals of Nuclear Energy*, 82:10–18, 2015.

[41] Alex F Bielajew and David WO Rogers. Presta: the parameter reduced electron-step transport algorithm for electron monte carlo transport. *Nuclear Instruments and Methods in Physics Research Section B: Beam Interactions with Materials and Atoms*, 18 (1-6):165–181, 1986.

[42] Iwan Kawrakow and Alex F Bielajew. On the representation of electron multiple elastic-scattering distributions for monte carlo calculations. *Nuclear Instruments and Methods in Physics Research Section B: Beam Interactions with Materials and Atoms*, 134(3-4): 325–336, 1998.

[43] DWO Rogers, BRBI Walters, Iwan Kawrakow, et al. Beamnrc users manual. *Nrc Report Pirs*, 509:12, 2009.

[44] BRBI Walters, Iwan Kawrakow, DWO Rogers, et al. Dosxyznrc users manual. *Nrc Report Pirs*, 794:57–58, 2005.

[45] ML Rodríguez. Penlinac: extending the capabilities of the monte carlo code penelope for the simulation of therapeutic beams. *Physics in Medicine & Biology*, 53(17):4573, 2008.

[46] Lorenzo Brualla, Miguel Rodriguez, Josep Sempau, and Pedro Andreo. Penelope/primo-calculated photon and electron spectra from clinical accelerators. *Radiation Oncology*, 14(1):6, 2019.

[47] Pedro Arce, Pedro Rato, Mario Canadas, and Juan Ignacio Lagares. Gamos: A geant4-based easy and flexible framework for nuclear medicine applications. In *2008 IEEE Nuclear Science Symposium Conference Record*, pages 3162–3168. IEEE, 2008.

[48] Chul-Young Yi, Suck-Ho Hah, and Min Sun Yeom. Monte carlo calculation of the ionization chamber response to beam using penelope. *Medical physics*, 33(5):1213–1221, 2006.

[49] Lilie LW Wang and David WO Rogers. Monte carlo study of si diode response in electron beams. *Medical physics*, 34(5):1734–1742, 2007.

[50] Paola Solevi, Giulio Magrin, Davide Moro, and Ramona Mayer. Monte carlo study of microdosimetric diamond detectors. *Physics in Medicine & Biology*, 60(18):7069, 2015.

[51] CL Hartmann-Siantar, PM Bergstrom, and WP Chandler. Lawrence livermore national laboratorys peregrine project. Technical report, Lawrence Livermore National Lab.(LLNL), Livermore, CA (United States), 1997.

[52] M Fippel, W Laub, B Huber, and F Nuesslin. Xvmc-fast monte-carlo dose calculation for photon beam treatment planning; xvmc-schnelle monte-carlo-dosisberechnung fuer

die bestrahlungsplanung bei photonenstrahlung. *Zeitschrift fuer Medizinische Physik*, 9, 1999.

[53] Josep Sempau, Scott J Wilderman, and Alex F Bielajew. Dpm, a fast, accurate monte carlo code optimized for photon and electronradiotherapy treatment planning dose calculations. *Physics in Medicine & Biology*, 45(8):2263, 2000.

[54] X George Xu. An exponential growth of computational phantom research in radiation protection, imaging, and radiotherapy: a review of the fifty-year history. *Physics in Medicine & Biology*, 59(18):R233, aug 2014. doi: 10.1088/0031-9155/59/18/R233. URL https://dx.doi.org/10.1088/0031-9155/59/18/R233.

[55] Wolfgang Kainz, Esra Neufeld, Wesley E Bolch, Christian G Graff, Chan Hyeong Kim, Niels Kuster, Bryn Lloyd, Tina Morrison, Paul Segars, Yeon Soo Yeom, et al. Advances in computational human phantoms and their applications in biomedical engineering—a topical review. *IEEE transactions on radiation and plasma medical sciences*, 3(1):1–23, 2018.

[56] James E Brown, Rui Qiang, Paul J Stadnik, Larry J Stotts, and Jeffrey A Von Arx. Mr conditional safety assessment of implanted medical devices: Advantages of computational human phantoms. In *2016 38th Annual International Conference of the IEEE Engineering in Medicine and Biology Society (EMBC)*, pages 6465–6468. IEEE, 2016.

[57] Panagiotis Papadimitroulas. Dosimetry applications in gate monte carlo toolkit. *Physica Medica*, 41:136–140, 2017.

[58] Camilo M Correa-Alfonso, Julia D Withrow, Sean J Domal, Shu Xing, Jungwook Shin, Clemens Grassberger, Harald Paganetti, and Wesley E Bolch. A mesh-based model of liver vasculature: implications for improved radiation dosimetry to liver parenchyma for radiopharmaceuticals. *EJNMMI physics*, 9(1):28, 2022.

[59] Chan Hyeong Kim, YS Yeom, Nina Petoussi-Henß, M Zankl, Wesley Emmett Bolch, Choonsik Lee, Chansoo Choi, Thang Tat Nguyen, K Eckerman, HS Kim, et al. Icrp

publication 145: adult mesh-type reference computational phantoms. *Annals of the ICRP*, 49(3):13–201, 2020.

[60] Steven M Strasberg. Nomenclature of hepatic anatomy and resections: a review of the brisbane 2000 system. *Journal of hepato-biliary-pancreatic surgery*, 12(5):351–355, 2005.

[61] W Schreiner. Computer generation of complex arterial tree models. *Journal of biomedical engineering*, 15(2):148–150, 1993.

[62] J Pfitzner. Poiseuille and his law. *Anaesthesia*, 31(2):273–275, 1976.

[63] Cecil D Murray. The physiological principle of minimum work applied to the angle of branching of arteries. *The Journal of general physiology*, 9(6):835, 1926.

[64] Roger W Howell. The mird schema: from organ to cellular dimensions. *Journal of Nuclear Medicine*, 35(3):531–533, 1994.

[65] Jungwook Shin, Shu Xing, Lucas McCullum, Abdelkhalek Hammi, Jennifer Pursley, Camilo A Correa, Julia Withrow, Sean Domal, Wesley Bolch, Harald Paganetti, et al. Hedos—a computational tool to assess radiation dose to circulating blood cells during external beam radiotherapy based on whole-body blood flow simulations. *Physics in Medicine & Biology*, 66(16):164001, 2021.

[66] Jack Valentin. Basic anatomical and physiological data for use in radiological protection: reference values: Icrp publication 89: Approved by the commission in september 2001. *Annals of the ICRP*, 32(3-4):1–277, 2002.

[67] Bernd Grosswendt. Icrp publication 110, 2012.

[68] Claude COUINAUD. Lobes et segments hepatiques. *Press Med*, 62:709–712, 1954.

[69] C Couinaud. Liver anatomy: portal (and suprahepatic) or biliary segmentation. *Digestive surgery*, 16(6):459–467, 1999.

[70] Abdelkhalek Hammi, Harald Paganetti, and Clemens Grassberger. 4d blood flow model for dose calculation to circulating blood and lymphocytes. *Physics in Medicine & Biology*, 65(5):055008, 2020.

[71] Chris Beekman, Julia D Withrow, Camilo M Correa Alfonso, Shreya P Pathak, Robert J Dawson, Natalia Carrasco-Rojas, Andrew R Sforza, Carlos G Colon, Wesley E Bolch, Clemens Grassberger, et al. A stochastic model of blood flow to calculate blood dose during radiotherapy. *Physics in Medicine & Biology*, 68(22):225007, 2023.

[72] Rohan Amare, Amir A Bahadori, and Steven Eckels. A structured cleaving mesh for bioheat transfer application. *IEEE Open Journal of Engineering in Medicine and Biology*, 1:174–186, 2020.

[73] V Shanthoshini Deviha, P Rengarajan, and R Jahir Hussain. Modeling blood flow in the blood vessels of the cardiovascular system using fractals. *Applied Mathematical Sciences*, 7(11):527–537, 2013.

[74] Erlend Hodneland, Erik Hanson, Ove Sævareid, Geir Nævdal, Arvid Lundervold, Veronika Šoltészová, Antonella Z Munthe-Kaas, Andreas Deistung, Jürgen R Reichenbach, and Jan M Nordbotten. A new framework for assessing subject-specific whole brain circulation and perfusion using mri-based measurements and a multi-scale continuous flow model. *PLoS computational biology*, 15(6):e1007073, 2019.

[75] Stephen Blowers, Ian Marshall, Michael Thrippleton, Peter Andrews, Bridget Harris, Iain Bethune, and Prashant Valluri. How does blood regulate cerebral temperatures during hypothermia? *Scientific reports*, 8(1):7877, 2018.

[76] Luca Heltai, Alfonso Caiazzo, and Lucas O Müller. Multiscale coupling of one-dimensional vascular models and elastic tissues. *Annals of Biomedical Engineering*, 49:3243–3254, 2021.

[77] Rohan Amare, Erlend Hodneland, Jeremy A Roberts, Amir A Bahadori, and Steven

Eckels. Modeling a 3-d multiscale blood-flow and heat-transfer framework for realistic vascular systems. *Scientific Reports*, 12(1):14610, 2022.

[78] Jørg E Aarnes, Tore Gimse, and Knut-Andreas Lie. An introduction to the numerics of flow in porous media using matlab. In *Geometric modelling, numerical simulation, and optimization: applied mathematics at SINTEF*, pages 265–306. Springer, 2007.

[79] Howard Eves. Two surprising theorems on cavalieri congruence. *The College Mathematics Journal*, 22(2):118–124, 1991. doi: 10.1080/07468342.1991.11973367. URL https://doi.org/10.1080/07468342.1991.11973367.

[80] Julius Friedrich Cohnheim. *Gesammelte Abhandlungen*. A. Hirschwald, 1885.

[81] Phillipe A Hasgall, F Di Gennaro, C Baumgartner, E Neufeld, B Lloyd, MC Gosselin, D Payne, A Klingenböck, and N Kuster. It'is database for thermal and electromagnetic parameters of biological tissues. *Version 4.0*, 15:2018, 2018.

[82] A Victor Hoffbrand and Steensma DP. Hoffbrand's essential haematology, 2019.

[83] Hirotogu Akaike. Information theory and an extension of the maximum likelihood principle. In *Selected papers of hirotugu akaike*, pages 199–213. Springer, 1998.

[84] Rohan Amare, Amir A Bahadori, and Steven J Eckels. Analysis of sphere of influence (soi) and pressure drop parameter in vom-phys framework. In *ASTFE Digital Library*. Begel House Inc., 2023.

[85] RA Forster, TE Booth, and SP Pederson. Ten new checks to assess the statistical quality of monte carlo solutions in mcnp. Technical report, Los Alamos National Lab., NM (United States), 1994.

[86] N Casson. Rheology of disperse systems. *Flow Equation for Pigment Oil Suspensions of the Printing Ink Type. Rheology of Disperse Systems*, pages 84–102, 1959.

[87] Marie-Catherine Vozenin, Jean Bourhis, and Marco Durante. Towards clinical translation of flash radiotherapy. *Nature Reviews Clinical Oncology*, 19(12):791–803, 2022.

# Appendix A

# Pressure Map for Various SoI Cases

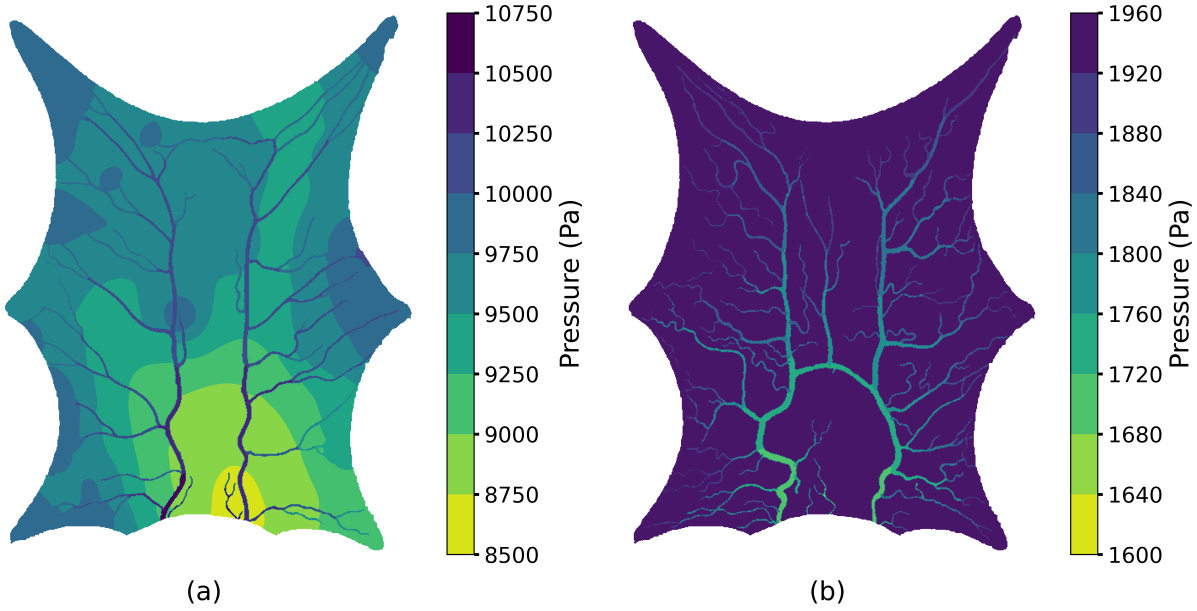


Figure A.1: Pressure map in the frog tongue for SoI radius $\epsilon = 2$mm. (a) Arterial compartment of Layer 1. (b) Venous compartment of Layer 3.

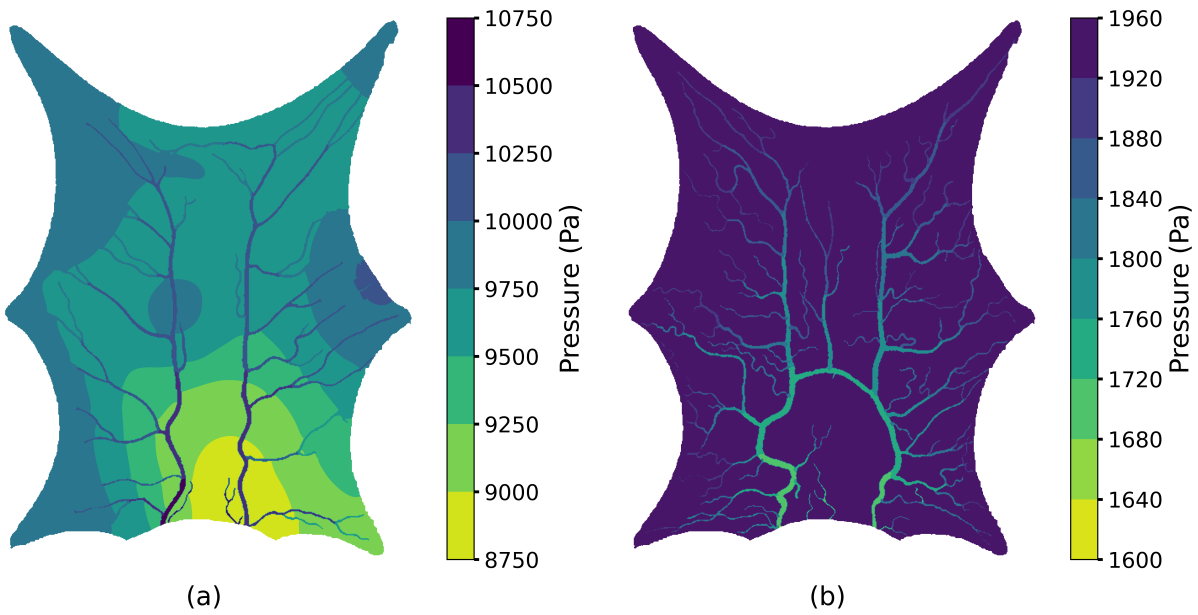


Figure A.2: Pressure map in the frog tongue for SoI radius $\epsilon = 5$mm. (a) Arterial compartment of Layer 1. (b) Venous compartment of Layer 3.

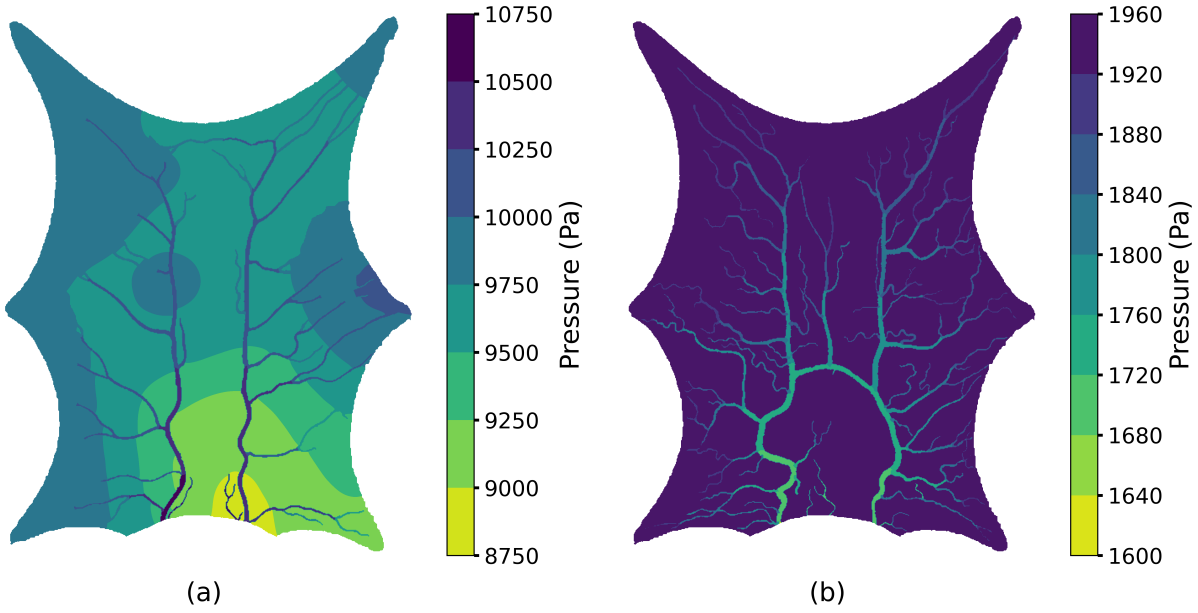


Figure A.3: Pressure map in the frog tongue for SoI radius $\epsilon = 7$mm. (a) Arterial compartment of Layer 1. (b) Venous compartment of Layer 3.

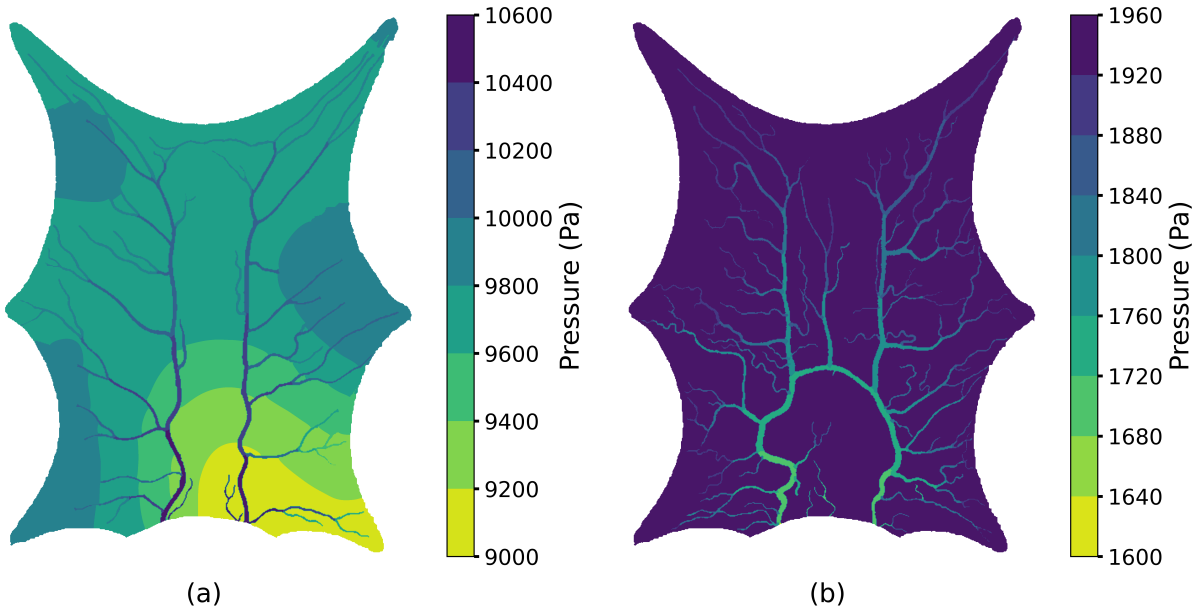


Figure A.4: Pressure map in the frog tongue for SoI radius $\epsilon = 10$mm. (a) Arterial compartment of Layer 1. (b) Venous compartment of Layer 3.

# Appendix B

# Transit Time Distributions

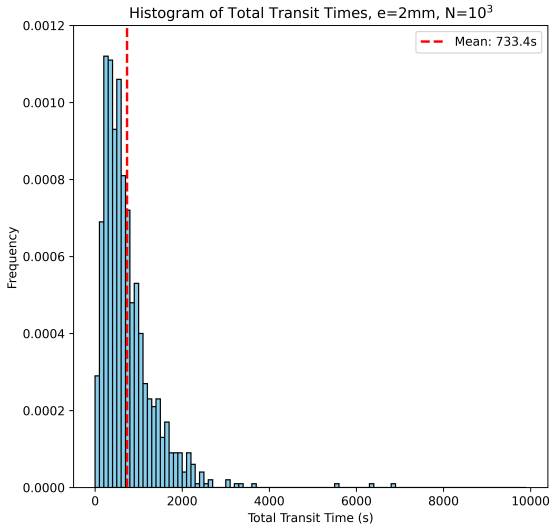


(a) N = $10^3$

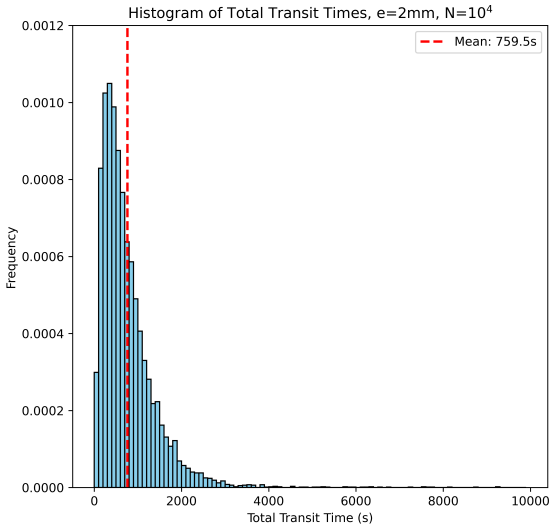


(b) N = $10^4$

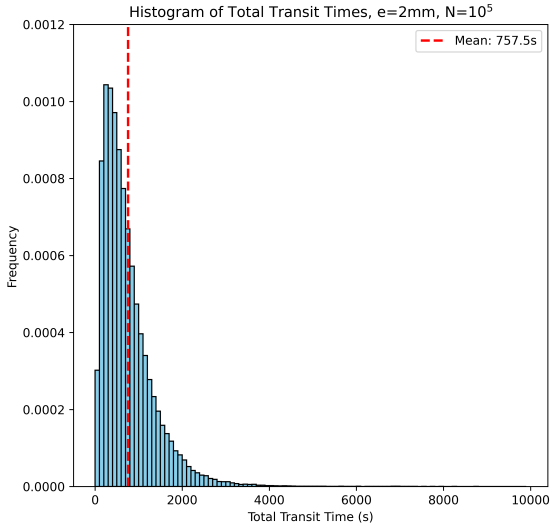


(c) N = $10^5$

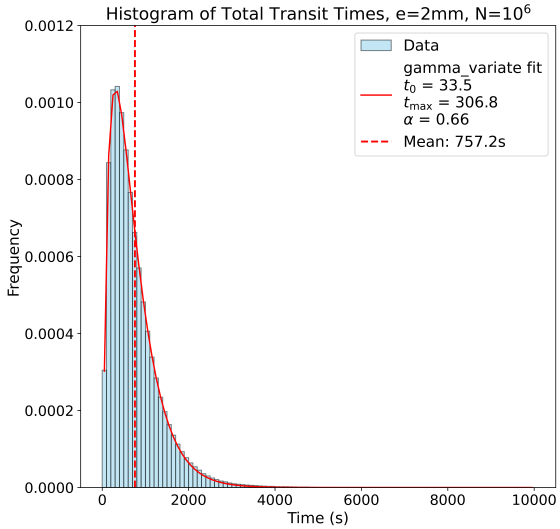


(d) N = $10^6$

Figure B.1: Transit time distribution for $\epsilon = 2$mm.

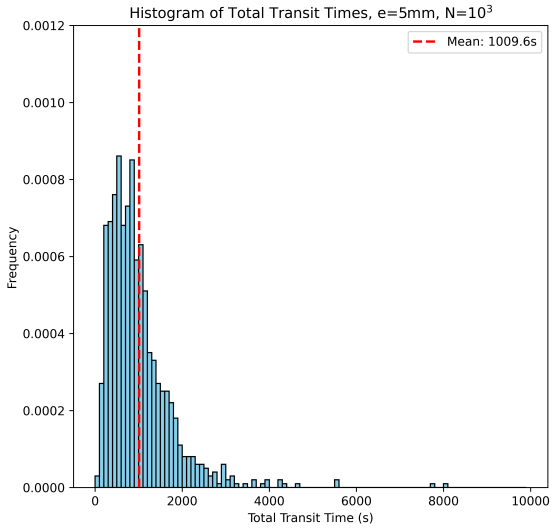


(a) N = $10^3$

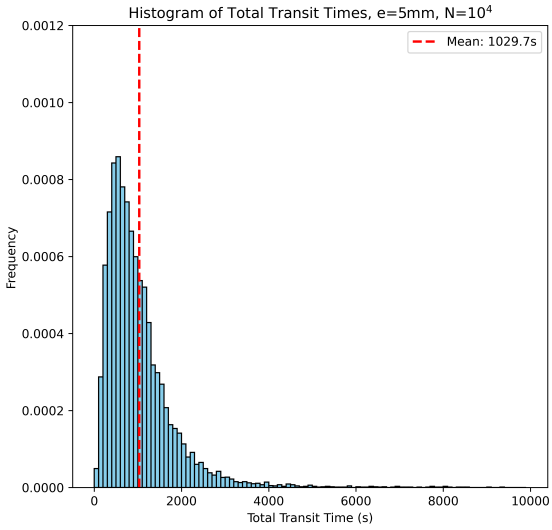


(b) N = $10^4$

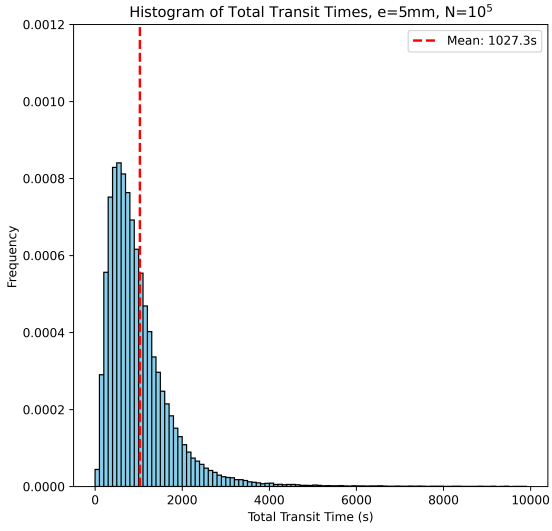


(c) N = $10^5$

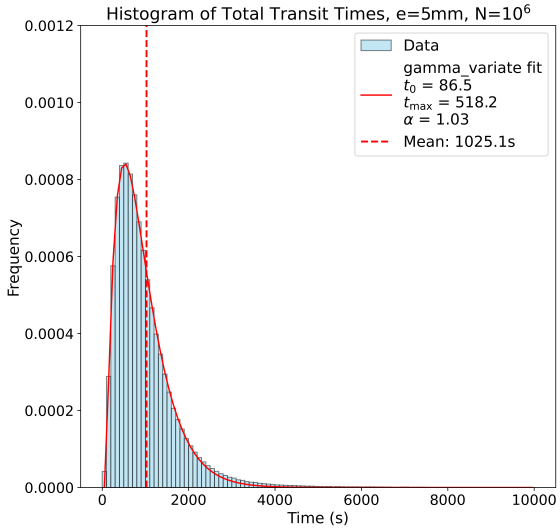


(d) N = $10^6$

Figure B.2: Transit time distribution for $\epsilon = 5$mm.

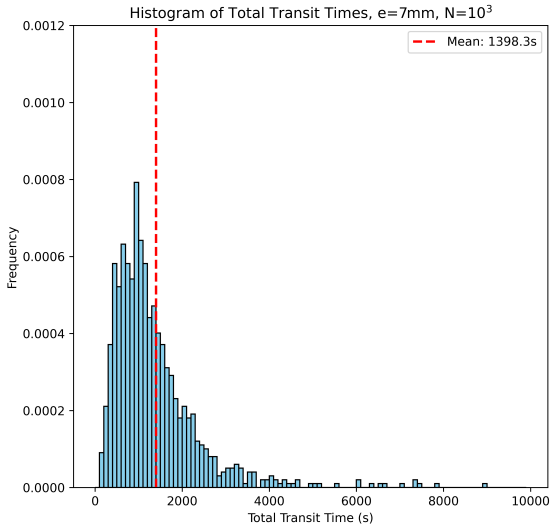


(a) N = $10^3$

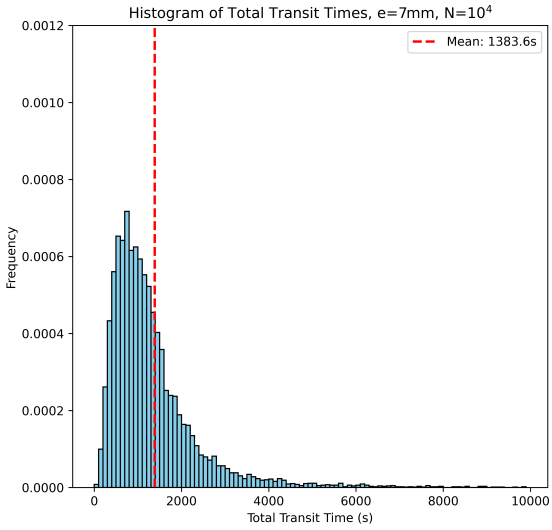


(b) N = $10^4$

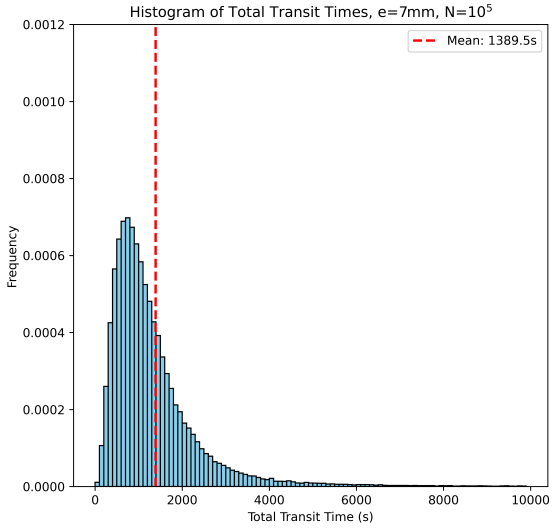


(c) N = $10^5$

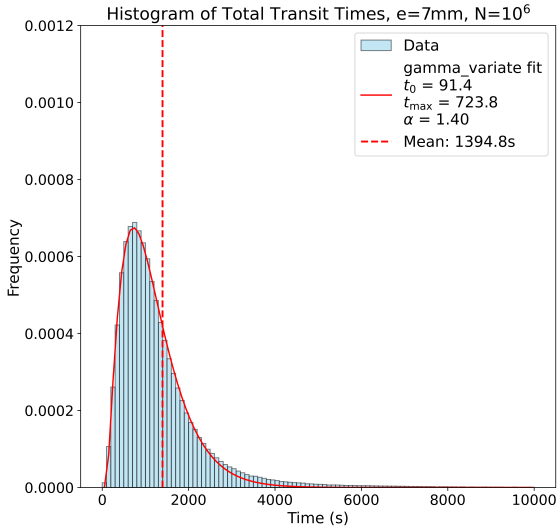


(d) N = $10^6$

Figure B.3: Transit time distribution for $\epsilon = 7$mm.

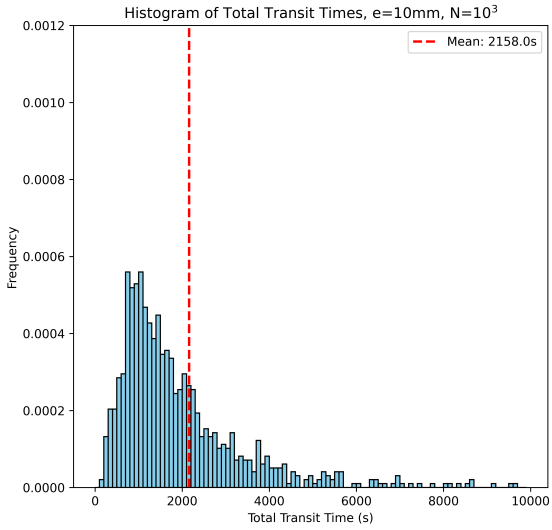


(a) N = $10^3$

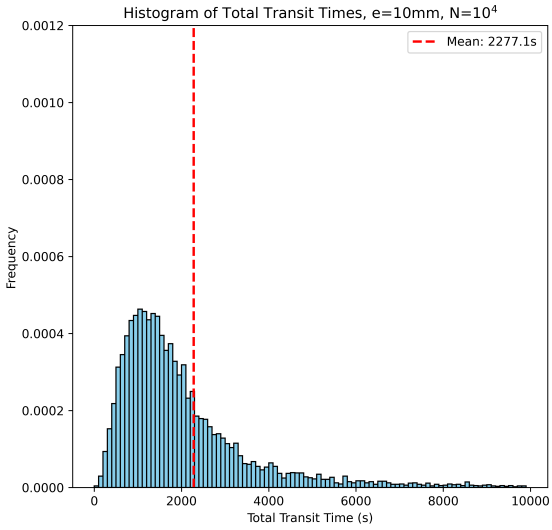


(b) N = $10^4$

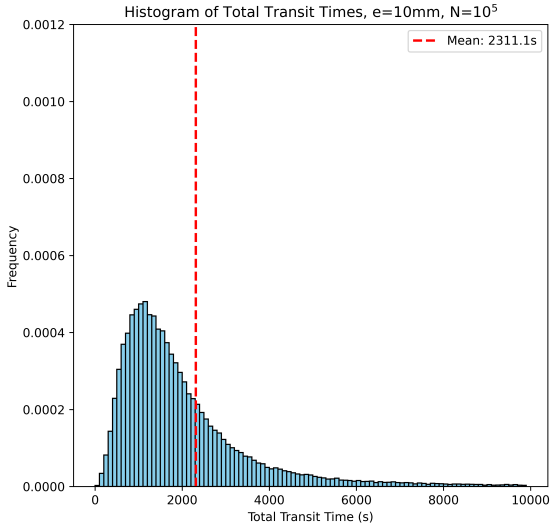


(c) N = $10^5$

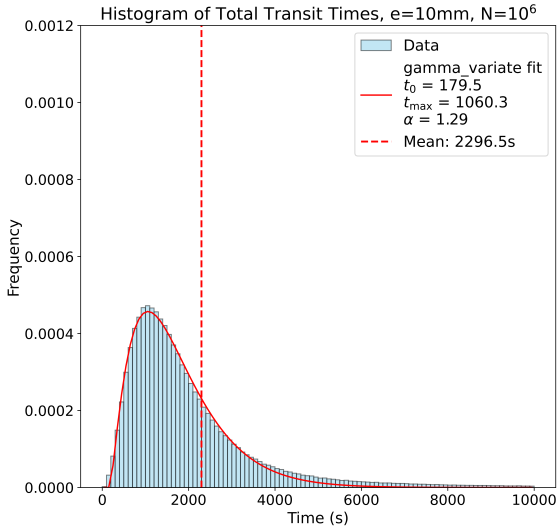


(d) N = $10^6$

Figure B.4: Transit time distribution for $\epsilon = 10$mm.

# Appendix C

# Minimum Transit Time Calculation

To calculate a minimum transit time through the frog-tongue, the particle was assumed to run through the centerline of the vessel segments. At a terminal arterial node, the particle was delivered to the central outlet node fed by the terminal in the arterial compartment of the tissue domain, instantly. Subsequently, the particle instantly perfused to the venous compartment and jumped to the nearest venous terminal. Finally, it traced its path along the centerline of the venous vasculatures to exit the network. The following data are taken from a path-tracing simulation of SoI radius $\epsilon = 10$ mm.

The nodes it follows in the arterial vasculature are,

$0 \rightarrow 1 \rightarrow 2 \rightarrow 3 \rightarrow 4 \rightarrow 48$

$P_0 = 10\,600\,\mathrm{Pa}$, $P_1 = 10\,565.53\,\mathrm{Pa}$

$\mu = 3 \times 10^{-3}\,\mathrm{Pa\,s}$, $L = 53$, $dx = 6.4 \times 10^{-5}\,\mathrm{m}$

$R = 3.5$, $r = 0$

$$
\begin{aligned}
t_{1,0} &= \frac{4 \times \mu \times (L_{01} \times dx)^2}{(P_0 - P_1)(R_{01}^2 - r^2)(dx)^2} \\
&= \frac{4 \times 3 \times 10^{-3}\ \mathrm{Pa\ s} \times (53 \times 6.4 \times 10^{-5}\ \mathrm{m})^2}{(10600 - 10565.53)\ \mathrm{Pa} \times ((3.5 \times 6.4 \times 10^{-5}\ \mathrm{m})^2 - 0^2)} \\
&= 0.07983\ \mathrm{s}
\end{aligned}
$$

Similarly, for the other segments,

$t_{2,1} = 0.03919$ s, $t_{3,2} = 0.05084$ s, $t_{4,3} = 0.09680$ s, $t_{48,4} = 0.07285$ s.

The times in the arterial and venous compartment are identically 0, since they are assumed instantaneous in this case.

The nodes followed in the venous vasculature are,

153→152→148→138→12→13→14→15→16→17→18→19→20

$P_{153} = 1940.6552\,\text{Pa}$, $P_{152} = 1787.8988\,\text{Pa}$

$L = 36$, $R = 0.5$

$$t_{152,153} = \frac{4 \times 3 \times 10^{-3}\ \text{Pa s} \times (36 \times 6.4 \times 10^{-5}\ \text{m})^2}{(1940.6552 - 1787.8988)\ \text{Pa} \times ((0.5 \times 6.4 \times 10^{-5}\ \text{m})^2 - 0^2)}$$
$$= 0.4072\ \text{s}$$

Similarly,

$t_{148,152} = 0.04320$ s, $t_{138,148} = 0.10834$ s, $t_{12,138} = 0.17956$ s, $t_{13,12} = 0.07288$ s, $t_{14,13} = 0.02444$ s, $t_{15,14} = 0.04604$ s, $t_{16,15} = 0.08135$ s, $t_{17,16} = 0.05734$ s, $t_{18,17} = 0.05992$ s, $t_{19,18} = 0.07482$ s, $t_{20,19} = 0.02595$ s

$$\begin{aligned}\text{In total} = {} & 0.07983\ s + 0.03919\ s + 0.05084\ s + 0.09680\ s + 0.07285\ s + 0.4072\ s + \\ & 0.04320\ s + 0.10834\ s + 0.17956\ s + 0.07288\ s + 0.02444\ s + 0.04604\ s + \\ & 0.08135\ s + 0.05734\ s + 0.05992\ s + 0.07482\ s + 0.02595 s \\ = {} & 1.52055\ s\end{aligned}$$

Hence, the minimum time is $\sim 1.52$ seconds. The histogram in Figure 4.2(d) shows the transit time distribution for $\epsilon = 10$ mm, simulated with $10^6$ particles. The minimum time found in this simulation was approximately $\sim 19.8$ seconds. This time is in a reasonable range judging by the minimum time obtained from the present calculation, provided that

the minimum time from the simulation accounts for the travel inside the tissue domain as well as the terminal jump.